U.PORTO
FEUP FACULDADE DE ENGENHARIA
UNIVERSIDADE DO PORTO

UPC UNIVERSITAT POLITÈCNICA
DE CATALUNYA
BARCELONATECH

MODELLING SAND INSTABILITY WITHIN THE FRAMEWORK OF CRITICAL STATE SOIL MECHANICS

CATARINA PAISANA FERREIRA CORREIA RAMOS

Dissertação submetida para satisfação parcial dos requisitos do grau de

MESTRE EM ENGENHARIA CIVIL — ESPECIALIZAÇÃO EM GEOTECNIA

Orientador: Professor Doutor António Joaquim Pereira Viana da Fonseca

---

Coorientador: Professor Doutor Jean Vaunat

JULHO DE 2013

MESTRADO INTEGRADO EM ENGENHARIA CIVIL 2012/2013
DEPARTAMENTO DE ENGENHARIA CIVIL

Tel. +351-22-508 1901

Fax +351-22-508 1446

✉ miec@fe.up.pt

Editado por

FACULDADE DE ENGENHARIA DA UNIVERSIDADE DO PORTO

Rua Dr. Roberto Frias

4200-465 PORTO

Portugal

Tel. +351-22-508 1400

Fax +351-22-508 1440

✉ feup@fe.up.pt

🌐 http://www.fe.up.pt

To my Mother and Father

Intelligence without ambition is a bird without wings

Salvador Dalí

ACKNOWLEDGEMENTS

During the process of doing and writing this Dissertation the author had the help and support of some people that deserve to be acknowledged:

- To my Portuguese supervisor, Professor António Viana da Fonseca, for the proposition of such a challenging work, for his constant help and advice during this period, for always recommending new approaches for the work and for helping me with the bibliography and final revision of the work.
- To my co-supervisor, Professor Jean Vaunat, for all the patience and help during these months, for the suggestion of new ideas and for the guidance throughout the elaboration of this work.
- To my mother and my father for always believing in me, supporting me and loving me.
- To my sister, family and friends for always being there for me and for all the good moments, the care and enjoyment they bring to my life.
- To my man Luís, for all the conversations, the motivation and support but especially for the unconditional love.

ABSTRACT

The aim of the present work was the study of a sand from *Les Dunes* beach in Ain Beninan, Algeria, where the Boumerdès earthquake occurred in 2003. This earthquake caused a lot of structural damages and claimed the lives of many people. Many damages caused to infrastructures are related to the phenomenon of liquefaction.

A brief introduction to the concepts of liquefaction, elasto-plasticity and critical state theory is done in the attempt to have a framework. These concepts are of main importance as they are the base of this study and essential for the interpretation of the results presented. The model used in this work was the unified critical state constitutive model for clays and sands (CASM), developed by Yu (1998), which is implemented in *Code_Bright*.

The study was based on the results of two drained and six undrained triaxial tests, performed by Pinheiro (2009) and Rocha (2010) at LabGeo. All the tests performed followed compression stress-paths in monotonic conditions and the specimens were isotropically consolidated as the objective was to study the instability and liquefaction phenomenon due to static loading.

The results were compared with simulations done in *Code_Bright*, a finite element program for numerical calculations. The parameters that characterize the sand were obtained from laboratory data or through calibration for a suitable curve fitting. CASM is implemented in *Code_Bright* and the comparison between the experimental results and the numerical solution allows for the verification of the applicability of the model.

The instability is studied with the second-order work increment criterion, with which the instability line for this sand is determined. The dilatancy rate defined by Rowe (1962) is studied in the points where instability begins and it is shown once more that CASM can model liquefaction in materials where the instability line is straight in p'–q space.

It is shown that specimens that have been performed under drained conditions are always stable, even when their stress-paths are inside the region of potential instability. On the other hand, under undrained conditions, specimens may become unstable after crossing the instability line. Some tests were also simulated, which started with drained conditions but then change to undrained conditions at different time steps. Finally, the Normal Compression Line, the Critical State Line and the Instability Line were defined in the e-lnp' space.

KEYWORDS: constitutive model, critical state, elastoplasticity, flow liquefaction, instability of sands

RESUMO

O objetivo deste trabalho foi o estudo de uma areia proveniente da praia *Les Dunes*, em Ain Beninan na Argélia, onde, em 2003, o terramoto de Boumerdès ocorreu. Este terramoto causou vários danos estruturais e tirou a vida a muitas pessoas. Muitos dos danos causados em infra-estruturas estão relacionados com o fenómeno da liquefação.

Uma breve introdução e enquadramento sobre os conceitos de liquefação, elasto-plasticidade e teoria dos estados críticos são apresentados. Estes conceitos são muito importantes pois são a base deste estudo e essenciais para a interpretação dos resultados apresentados. O modelo utilizado neste trabalho é um modelo constitutivo do estado crítico unificado para argilas e areias (CASM), desenvolvido por Yu (1998) e está implementado no programa *Code_Bright*.

O estudo foi baseado nos resultados de ensaios triaxiais, dois drenados e seis não drenados, realizados por Pinheiro (2009) e Rocha (2010) no LabGeo, da FEUP. Todos os ensaios foram realizados em carregamento de compressão e monotónicos e todas as amostras foram consolidadas isotropicamente, uma vez que o objetivo deste trabalho é o estudo da instabilidade e do fenómeno de liquefação devido a carregamentos estáticos.

Os resultados foram comparados com simulações realizadas no *Code_Bright*, um programa de elementos finitos para cálculo numérico. Os parâmetros que caracterizam a areia foram obtidos através de ensaios de laboratório ou por calibração até as curvas se ajustarem adequadamente. O CASM está implementado no *Code_Bright* e a comparação entre os resultados experimentais e a solução numérica permite a verificação da aplicabilidade do modelo.

A instabilidade foi estudada segundo o critério do incremento de trabalho de segunda ordem e a linha de instabilidade da areia é determinada. A taxa de dilatância definida por Rowe (1962) é estudada nos pontos de início de instabilidade e é demostrado mais uma vez que o modelo CASM permite a modelação da liquefação nos materiais em que a linha de instabilidade é reta no espaço p'–q.

É demonstrado que as amostras realizadas em condições drenadas são sempre estáveis, mesmo quando as tensões se encontram dentro da região de potencial instabilidade. Por outro lado, quando submetidas a condições não drenadas, as amostras podem tornar-se instáveis após passar a linha de instabilidade. Também foram simulados com sucesso ensaios que começam drenados mas passam a não drenados em diferentes intervalos de tempo. Finalmente foram definidas a linha normalmente consolidada, a linha dos estados críticos e a linha de instabilidade no espaço e-lnp'.

PALAVRAS-CHAVE: elasto-plasticidade, estado crítico, instabilidade nas areias, liquefação por fluxo, modelo constitutivo

TABLE OF CONTENTS

LIST OF FIGURES

LIST OF TABLES

NOMENCLATURE

Latin characters

B – Skempton parameter

C_U – coefficient of uniformity

C_C – coefficient of curvature

D – dry

D_r – relative density

D_{10} – diameter correspondent to 10% passing

D_{30} – diameter correspondent to 30% passing

D_{60} – diameter correspondent to 60% passing

D_{100} – diameter correspondent to 100% passing

d – dilatancy rate

dq – increment of deviatoric stress

dp' – increment of effective mean stress

d^2W – second order work increment

E – Young's modulus

e – void ratio

e_0 – initial void ratio

e_f – void ratio at ultimate state

e_{max} – maximum void ratio

e_{min} – minimum void ratio

f – yield function

G – shear modulus

g – plastic potential function

K – bulk modulus

K_0 – coefficient of earth pressure at rest

$(k_{11})_0$ – intrinsic permeability, 1st principal direction

M – slope of the Critical State line (in q-p' space)

N – specific volume of the NCL when p' = 1 kPa

n – shape parameter

n – porosity

p' – effective mean stress

p'_0 – preconsolidation pressure

p'_e – equivalent pressure on the NCL

p'_c – critical pressure

q – deviatoric stress

r – spacing ratio

S – degree of saturation

u – pore pressure

V_P – P wave velocity

V_S – S wave velocity

W – wet

w – moisture content

Greek characters

β – size parameter

Γ – specific volume of the critical state line at $p'=1$kPa

γ – total unit weight

γ_{sat} – saturated unit weight

γ_d – density

δ – small increment of

ε_a – axial strain

ε_p – volumetric strain

ε_q – shear strain

ε_r – radial strain

ε_s – shear strain

ε_v – volumetric strain

η – stress ratio

κ – slope of the isotropic swelling line (in υ-lnp' space)

λ – slope of the CSL (in υ-lnp' space)

ν – Poisson’s ratio

ξ – state parameter

ξ_R – reference state parameter

σ – total stress

σ_a – total axial stress

σ_r – total radial stress

υ – specific volume

Φ' – friction angle

Φ_c – critical friction angle

Abbreviations and Acronyms

BP – Back Pressure

CAD – Computer Aided Design

CASM – Clay And Sand Model

CID – Consolidated Isotropically Drained

CIMNE – International Center for Numerical Methods in Engineering

CIU – Consolidated Isotropically Undrained

CP – Cell Pressure

CSL – Critical State Line

FEUP – Faculdade de Engenharia da Universidade do Porto

LD – Les Dunes

NCL – Normal Compression Line

NRC – National Research Council

OCR – Overconsolidation ratio

UPC – Universitat Politècnica de Catalunya

1

INTRODUCTION

1.1. PROLOGUE

Every day, geotechnical engineers have to deal with problems related to failure of granular soils. One of these problems is the liquefaction of loose sands under undrained conditions, which can cause devastating damages.

Constitutive models can reproduce the response of soils to applied loads. One of the widely used frameworks to formulate constitutive models is the elasto-plastic theory. Elasto-plastic models based on the critical state concept have been used to simulate real soil behaviour. Some examples are the Cam-clay model (Roscoe et al., 1958), the modified Cam-clay model (Roscoe and Burland, 1968) and the Clay and Sand model (Yu, 1998).

But the constitutive models formulations alone are not sufficient to solving the practical engineering problems. It is necessary to implement the models in numerical tools, such as finite element codes and checking and validate those implementations. For that, the comparison of numerical solutions with results of tests performed in real soils, that show the real soil behaviour, is essential.

The choice of the model that is going to be used to simulate the material behaviour is very important. The quality of the results obtained depends on the selected model and on its implementation. So it is important to choose a model based on the kind of material to be modelled, the number of information available and the type of results being pursued. The applicability of the model for a specific material is of extreme importance, inview of using the numerical results with sufficient reliability.

The study of instability is a huge concern when dealing with the safety of dams, structures, excavations or slopes because instability eventually leads to failure. In this work, the instability that leads to flow liquefaction under undrained conditions is studied according to the second-order work increment criterion and according to Lade (1994), that explains that, for materials isotropically consolidated under undrained conditions, the top of the yield surface is the onset of flow liquefaction.

1.2. SCOPE AND OBJECTIVES

This work is part of a study that the LabGeo from FEUP is developing, under the coordination of Professor Viana da Fonseca. It is scope of this study of soils susceptible to liquefaction, to evaluate *in situ* and in the laboratory the risks and their mitigation.

This work complements the studies that have been done in a particular sand, from *Les Dunes* beach in Ain Benian in Algeria, where in 2003 the Boumerdès earthquake occurred. This earthquake caused many liquefaction related occurrences so the study of the behaviour of this sand is very important for the understanding of the soil susceptibility for liquefaction. The work of this thesis, in particular, pretends to analyse some test results performed in the laboratory in previous studies and compare them with numerical solutions given by a specific model. Thus, the model can be tested and its applicability to this conditions can be verified to be subsequently used in future studies. The calibration of the parameters that constitute the model for this specific sand is also an objective of this work.

The study of the instability that leads to flow liquefaction is also a concern. The definition of the instability line for *Les Dunes* sand and its relation with yield surfaces will allow the identification of the region of potential instability and help in the evaluation of the susceptibility of soils to liquefy under undrained conditions. Other objective is the study of the dilatancy rate, proposed by Rowe (1962) and used in CASM, for the results of the tests performed in *Les Dunes* sand.

1.3. ORGANIZATION OF THE THESIS

This work is organised in six Chapters and one Appendix.

Chapter 1 presents a short introduction of the work developed, as well as the scope and objectives that motivated this study and the organization of the thesis.

Chapter 2 presents the state of the art, where the main concepts of this work are explained in detail. First, a background on liquefaction is included, where some concepts such as flow and cyclic liquefaction are explained, as well as failure types and a criterion to evaluate the soil susceptibility for liquefaction. Secondly, a theoretical framework of the elasto-plastic models is presented as well as an introduction to critical state theory. The chapter finishes with the description of two Cam-clay models. One of them is the Clay and Sand Model, which is used to simulate the behaviour of *Les Dunes* sand in this Thesis and is explained with more detail.

Chapter 3 presents a small description of the Boumerdès Earthquake in Algeria (2003) and some images of the damages caused are included. The characteristics of *Les Dunes* sand are explained as well as the experimental data that is used to calibrate the model and to study the instability behaviour of the sand.

In Chapter 4, the Code where the CASM is implemented is explained. The numerical implementation and a description of the material parameters and their determination are given. The laboratory tests are reproduced with *Code_Bright* and the comparison with the experimental data is presented.

Chapter 5 presents the study of instability in this sand. A background on instability of sands is made followed by a study of *Les Dunes* sand, using the results of the drained and undrained tests and a simulation on specimens under drained conditions that become undrained at certain times of the test. The instability is interpreted based on the second-order work increment and the dilatancy rate is analysed.

Finally, Chapter 6 summarizes the conclusions and future developments of the present work.

Appendix A contains the equations and formulas for the implementation of CASM for triaxial path.

2

ELASTO-PLASTIC FRAMEWORK FOR MODELLING LIQUEFACTION IN SANDS

2.1. BACKGROUND ON LIQUEFACTION

Allen Hazen was the first to use the term *liquefied* in soil mechanics to explain the failure of Calaveras dam in California, in 1918. It is a complex concept that has been studied thoroughly over the last 50 years, especially due to the 1964 Niigata earthquake in Japan and the 1964 Alaska earthquake. These earthquakes caused liquefaction instabilities in many parts of the cities and were responsible for slope failures, bridge and building foundation failures and flotation and consequent lateral spreading of buried structures (Kramer, 1996).

There are a lot of disagreements related with the term liquefaction. The NRC (1985) states that the controversy concerning liquefaction is due to a number of facts. First, the soil is a very complex material, nonlinear, and its behaviour can change with time. There is a small number of studies on the behaviour of soils that experienced these phenomena during earthquakes where there was a good knowledge of the characteristics of the shaking action and the properties of the soil at the site. Apart from that, there is a clear uncertainty concerning the intensity and nature of future earthquakes. Nevertheless, there is a great incentive to find new methodologies to evaluate the consequences of earthquakes that would provide less expensive solutions to guarantee safety. Much progress has been made in understanding this phenomenon and in finding measures to ensure and implement safety and to mitigate the liquefaction hazard (NRC, 1985).

Liquefaction is a phenomenon that occurs normally, but not exclusively, in saturated granular soils and its consequences can be devastating. It is typically associated with a decrease of effective mean stress by the build-up of pore water pressure which causes the shear strength of the soil to decrease, towards the annulment. The name comes from the fact that when a soil suffers from this type of failure its behaviour is similar to a liquid.

Figure 2.1 shows a scheme of the phenomenon. When a soil is saturated, quick loads (such as earthquakes) generate undrained conditions, which cause the increase of pore water pressure, hence lowering the effective mean stresses. The build-up of pore pressure is due to the fact that there is no drainage in quick loadings and so the pore water cannot dissipate immediately. When the pore pressure increases enough to equal the total stress, the effective mean stress is reduced to essentially zero and liquefaction occurs.

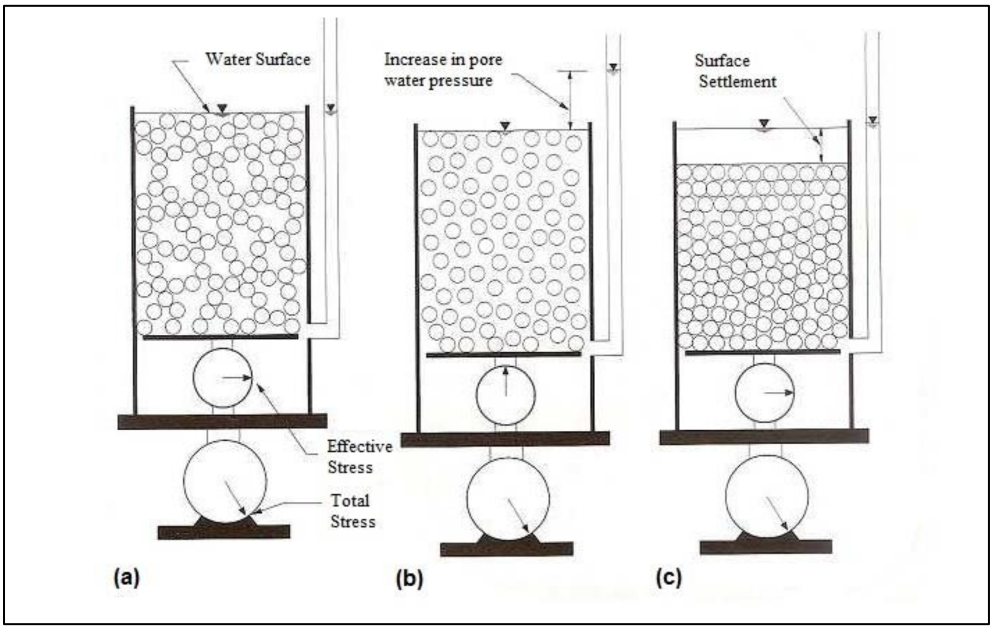

Figure 2.1 – Liquefaction scheme. a) before liquefaction; b) during liquefaction; c) after liquefaction (Ishihara, 1985)

According to the National Research Council (NRC, 1985), liquefaction can be associated with a phenomena giving rise to loss of shearing resistance or to the development of excessive strains. It can be divided into flow liquefaction and cyclic mobility (NCR, 1985; Kramer, 1996). The work developed in this thesis focuses on flow liquefaction so it will be discussed more thoroughly. Nevertheless, the cyclic mobility is discussed too, to make it easier to distinguish the two of them.

2.1.1. Flow Liquefaction

Kramer (1996) states that flow liquefaction occurs when the shear stress required for static equilibrium of a soil mass is greater than the shear strength of the soil in its liquefiable state. When this happens, great damages are caused. This type of liquefaction occurs in loose sands and/or silts, when they situate on the wet side of the Critical State Line (concepts explained later in this Chapter). If the soil is loose, it can suffer large volumetric deformations.

The US National Academy of Science's National Research Council (NRC, 1985) defines flow liquefaction as "*the condition where a soil mass can deform continuously under a shear stress less than or equal to the static shear stress applied to it. Equilibrium is restored, if at all, only after enormous displacements or settlements*". It can be triggered by monotonic or cyclic undrained loading conditions.

In the present work, it is considered that the soil liquefies (flow liquefaction) when the effective mean stress equals zero and the soil losses its shear strength, as it is shown is Figure 2.2. This is an example of a monotonic (static) test on an isotropically consolidated specimen of loose, saturated sand and the test is performed in undrained conditions.

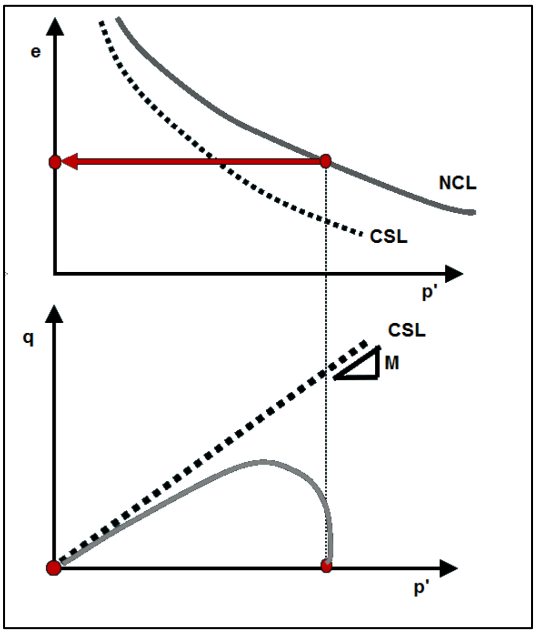

Figure 2.2 – Liquefaction definition in *e-p’* and *q-p’* spaces

Flow liquefaction is related to an instability that induces flow failure. Therefore, there has to be flow instability in order to occur flow failure but these two concepts are not the same (Andrade, 2009). According to Cañón (2010), flow liquefaction is associated with large deformations but the onset of instability occurs at small strains. In Figure 2.3 are represented the stress-path of an undrained test that liquefied and the point where instability begins. The concepts of instability will be discussed later in this work (Chapter 5).

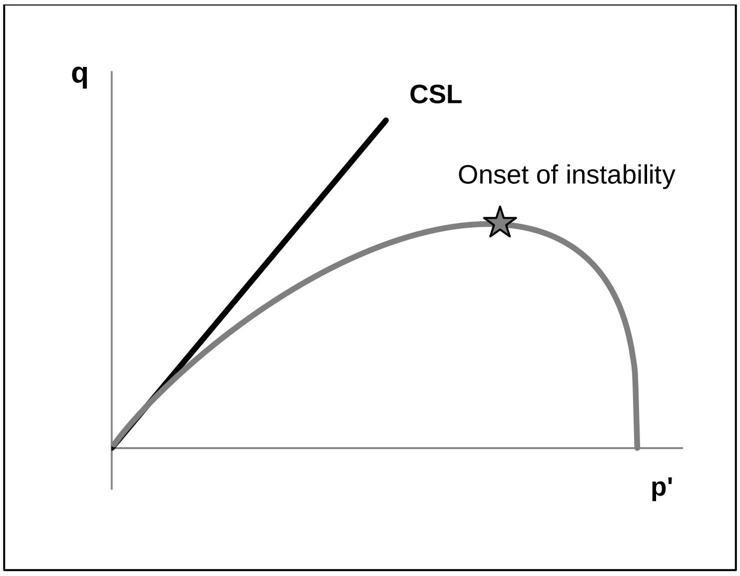

Figure 2.3 – Onset of instability in *q-p’* space

Flow liquefaction can also be triggered by cyclic loading. Figure 2.4 shows an example of a stress-path of a cyclic triaxial test on sand. The onset of liquefaction is located after the instability line. When the effective stress-path crosses the instability line and intercepts the collapse boundary (locus defined by the effective stress-path for monotonic loading where liquefaction is observed) liquefaction occurs on the specimens (Andrade and Ramos, 2013).

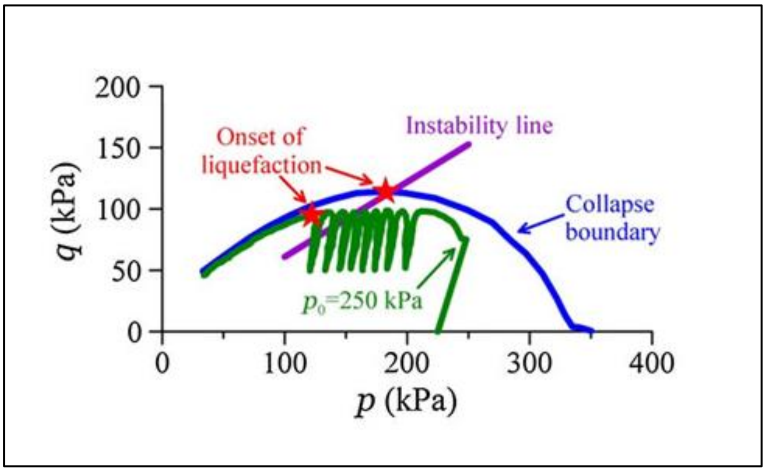

Figure 2.4 – Onset of instability under cyclic loading (Andrade and Ramos, 2013)

2.1.2. CYCLIC MOBILITY

Cyclic mobility is a phenomenon that occurs when the static shear stress is less than the shear strength of the liquefied soil and the deformations develop incrementally during earthquake shaking (Kramer, 1996). This type of liquefaction usually happens in dense soils, normal or overconsolidated.

The deformations depend not only on the density of the soil, confining stresses and the soil structure but also on the duration of the cyclic loading, magnitude and the present amount of stress reversal. This type of liquefaction is characterized by large vertical settlements and the development of *sand boils* at the ground surface, which are caused by the pressures generated during the cycles of shaking that force the liquefied sand and water to come to the ground surface through cracks. Land instability is also associated with cyclic mobility and it consists on cracking and sliding of ground down slopes or towards margins of rivers. This failure is called *lateral spreading* and it can cause a lot of damage to infrastructures and buildings.

2.1.3. FAILURE TYPES

Liquefaction is associated with a lot of phenomena that can cause the failure of the ground and damage in buildings and constructions. Sands' boils are formed during seismic shaking when high pore pressure causes water and sediments from sublayers to come to the surface by opening cracks. The water and sediments settle and forms a conical shape, similar to a small volcano. When there are paved surfaces like building foundations or roads, the sand-water ejection appear around structures.

Other type of failure is flow failure, which consists in the displacement of large masses of soil. This usually occurs in loose sands or silty sands on slopes greater than 3 degrees, especially in coastal areas (NRC, 1985). Figure 2.5 shows a diagram of a flow failure. The soil beneath the ground surface loses strength and a mass of soil "travels" down the slope.

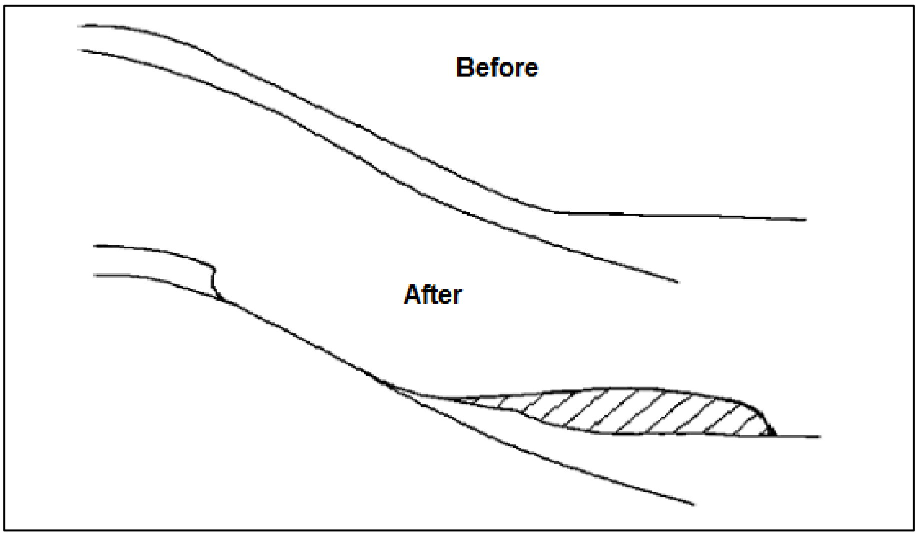

Figure 2.5 – Flow Failure (NRC, 1985)

Lateral spreads is another failure related to liquefaction and it implicates a large displacement of superficial blocks of soil. During an earthquake, movements of the ground are generated and horizontal displacements happen. Lateral spreads normally develop in gentle slopes (between 0.3 and 3 degrees) and move toward a free face (NRC, 1985). They can cause failure of foundations, ruptures in pipelines and sewers. In Figure 2.6 is represented this type of failure, which is one of the most catastrophic, as it is responsible for the immobilization of services in urban areas, unable to distribute water and assuring sanity.

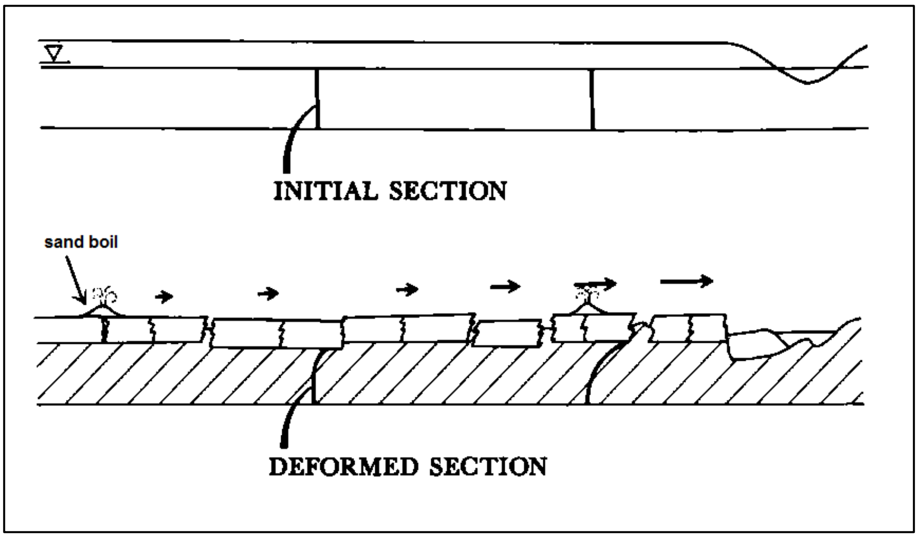

Figure 2.6 – Lateral Spreads (NRC, 1985)

Other types of failures are loss of bearing capacity, when a building is supported by a soil that liquefies and loses strength which causes large deformations, buoyant rise of buried structures such as tanks and pipelines that affect the community services and ground settlements (NRC, 1985).

2.1.4. SOIL SUSCEPTIBILITY FOR LIQUEFACTION

One approach for evaluating if a soil is susceptible to suffer liquefaction is based on its composition, i. e., the grain size of the particles. According to Terzaghi et al. (1996), a well graded soil is less susceptible to liquefaction because the smaller particles fill in the voids. This results in lower volumetric changes in drained conditions and in lower values of pore pressure generation in undrained conditions. It is safe to say that the grain size of the particles that constitute the solid part of the soil can be determinant for the analyses of soil liquefaction.

As it is shown in Figure 2.7, where the boundaries in the gradation curves for liquefiable soil and potentially liquefiable soil proposed by Tsuchida (1970) are represented, saturated granular soils are the most susceptible to suffer liquefaction. On the other hand, soils with great content of fine particles such as clays or fine silts, or coarse materials such as gravel or coarse sands are less susceptible to the liquefaction phenomenon occurrence. In the first type of soils, the plasticity of clays and fines prevent the rearrangement of particles. In the second type of soils, the space between the particles allows the dissipation of the pore water. It is also notable that a soil is more susceptible to liquefy if it is poorly graded, i. e., if the particles have approximately the same size and the soil is uniformly graded.

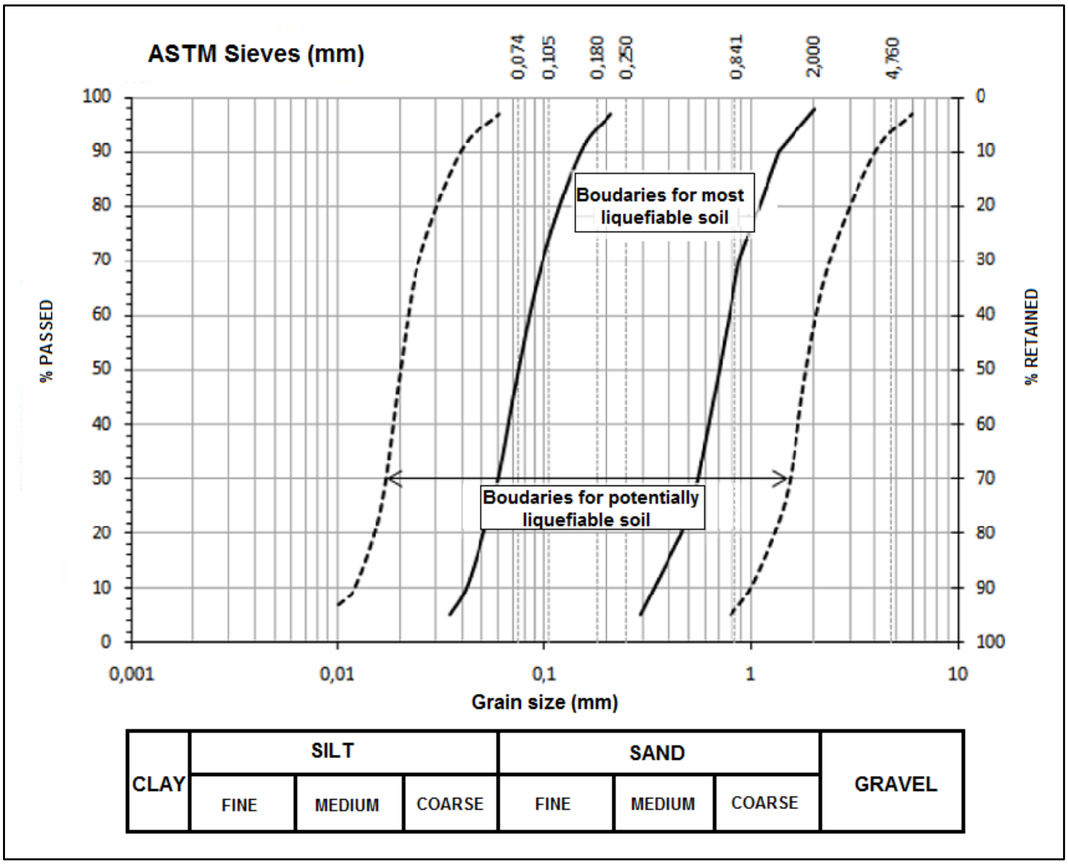

Figure 2.7 – Boundaries in the gradation curves for soils susceptible to liquefaction (adapted from Tsuchida, 1970)

2.2. ELASTO-PLASTICITY

Elasto-plastic theory provides one of the best frameworks to formulate constitutive models that can describe some of the most important features of soil behaviour. Elasto-plastic models based on the critical state concept have been used to simulate real soil behaviour.

Drucker et al. (1957) proposed the existence of a cap yield surface controlled by volume change and Roscoe et al. (1958) suggested a behavioural framework based on the concepts of critical state and the existence of a state boundary surface. These works on soil hardening and soil yielding established the basis for critical state theory.

The elastic constitutive models are unable to simulate some of the most important characteristics of real soil behaviour (Potts and Zdravković, 1999). By using the theory of plasticity, those models can be improved in order to describe those features. To explain and introduce the ideas of plastic yield, hardening and softening, it is considered the uniaxial behaviour of a linear elasto-plastic material.

2.2.1. UNIAXIAL BEHAVIOUR OF A LINEAR ELASTIC PERFECTLY PLASTIC MATERIAL

Considering a bar of an ideal linear elasto-plastic material loaded by the application of a compressive axial strain, ε, the stress-strain curve represented in Figure 2.8 illustrates this behaviour.

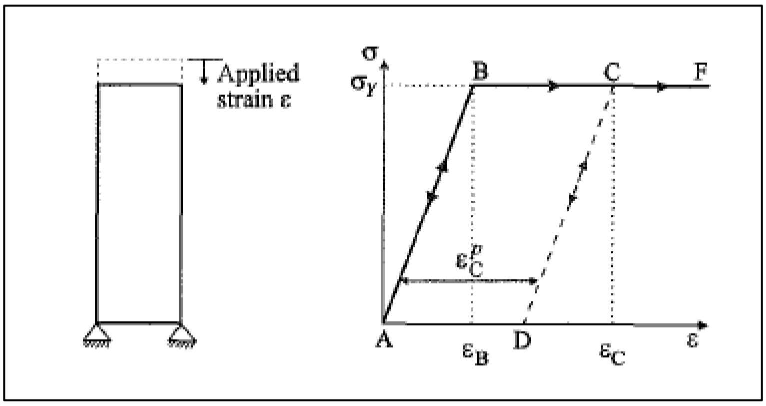

Figure 2.8 – Uniaxial loading for linear elastic perfectly plastic material (Potts and Zdravković, 1999)

As the strain is applied, the bar behaves elastically and the stress-strain curve follows the path AB. The slope of the line AB is the Young's modulus, E. As the material is linear elastic, if the bar is unloaded or unstrained before reaching point B, the stress-strain response moves down on the line AB and there is no permanent deformations. If the strain applied passes ε_B, the material becomes plastic because it reached the yield stress, σ_y. The stress remains constant, with the value of σ_y, and if the bar is unloaded it becomes elastic and the stress-strain curve travels along CD, a line parallel to AB. When the bar is unloaded until point D, where the stress is zero, there is a permanent strain (shortening) in the bar, equal to $\varepsilon_C^p = \varepsilon_C - \varepsilon_B$. On reloading the bar, the stress-strain curve follows the path DC until point C, in which the axial stress is the same as the yield stress and the bar is plastic. After reaching point C, the curve moves along CF. The behaviour on the paths AB and CD is reversible whereas on the path BCF is irreversible. If the bar is loaded by an increasing stress, it is not possible to apply a stress greater than the yield stress otherwise it would result in infinite strains. This type of behaviour is known as linear elastic perfectly plastic.

2.2.2. UNIAXIAL BEHAVIOUR OF A LINEAR ELASTIC STRAIN HARDENING PLASTIC MATERIAL

Considering a bar made of a linear elastic strain hardening plastic material, the stress-strain curve is represented in Figure 2.9.

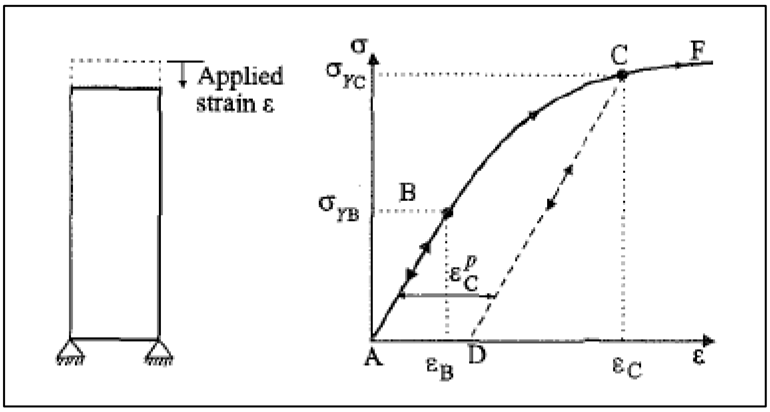

Figure 2.9 – Uniaxial loading for linear elastic strain hardening plastic material (Potts and Zdravković, 1999)

While the bar is loaded or strained until point B it behaves elastically (all along path AB). When the path reaches the point B, the stress is equal to the yield stress, σ_{yB} and if the strain goes beyond point B to point C, the initial yield stress is exceeded, without remaining constant. Instead, the stress increases to σ_{yC}. At this point, if the bar is unloaded, it becomes elastic and follows the path CD, a line parallel to BA. When the bar is unloaded to zero stress (point D) there is a permanent strain, ε_C^p. If the bar is reloaded, it follows the path DC, behaving elastically until the curve reaches point C where the bar is again plastic. The yield stress σ_{yC} is greater than σ_{yB} and this increase is due to the plastic straining from B to C. If the bar continues to be strained, eventually at some point (for example point F), the stress-strain curve becomes horizontal and the stress becomes constant.

2.2.3. UNIAXIAL BEHAVIOUR OF A LINEAR ELASTIC STRAIN SOFTENING PLASTIC MATERIAL

If the bar is now made of a linear elastic strain softening plastic material, the stress-strain curve is represented in Figure 2.10.

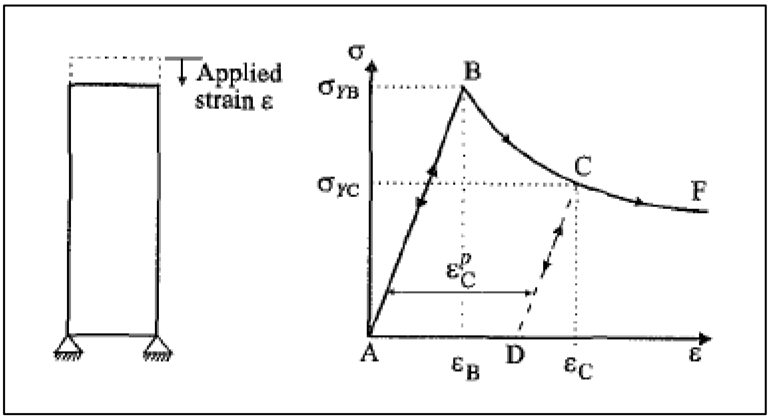

Figure 2.10 – Uniaxial loading for linear elastic strain softening plastic material (Potts and Zdravković, 1999)

When straining to point B, the bar has the same behaviour as the two presented before, both following a linear initial behaviour. However, when the stress-strain curve passes point B, instead of increasing with plastic straining, it decreases. The behaviour during unloading and reloading is the same as in the examples presented before. The fact that the yield stress decreases beyond point B is a concern because the material resistance to load diminishes.

2.2.4. BASIC CONCEPTS OF THE ELASTO-PLASTIC THEORY

As the model and results used in this work are obtained from triaxial tests, the model will be described in terms of triaxial stress variables *p'* and *q* and strain variables ε_p and ε_q. There are four basic components to formulate an elasto-plastic model:

- Elastic properties

The more usual elastic parameters are Young's modulus, *E'*, and Poisson's ratio, ν'. The bulk and shear moduli, for isotropic materials, can be written as a function of these two parameters as shown in equations (2.1) and (2.2) respectively.

$$K' = \frac{E'}{3(1-2\nu')} \tag{2.1}$$

$$G' = \frac{E'}{2(1+\nu')} \tag{2.2}$$

It is preferable to use bulk and shear moduli instead of Young's modulus and Poisson's ratio because in this way, the deviatoric or shear stress-strain relation and the volumetric strain variation due to isotropic stress change are considered separately.

Assuming that the soil behaves isotropically and elastically within the yield surface, the elastic response of the soil can be written as in (2.3). The linear elastic material behaviour is represented in Figure 2.11. In Figure 2.11 a) shearing mode is represented while in Figure 2.11 b) volumetric compression and expansion are drawn.

$$\begin{bmatrix} \delta\varepsilon_p^e \\ \delta\varepsilon_q^e \end{bmatrix} = \begin{bmatrix} 1/K' & 0 \\ 0 & 1/3G' \end{bmatrix} \begin{bmatrix} \delta p' \\ \delta q \end{bmatrix} \tag{2.3}$$

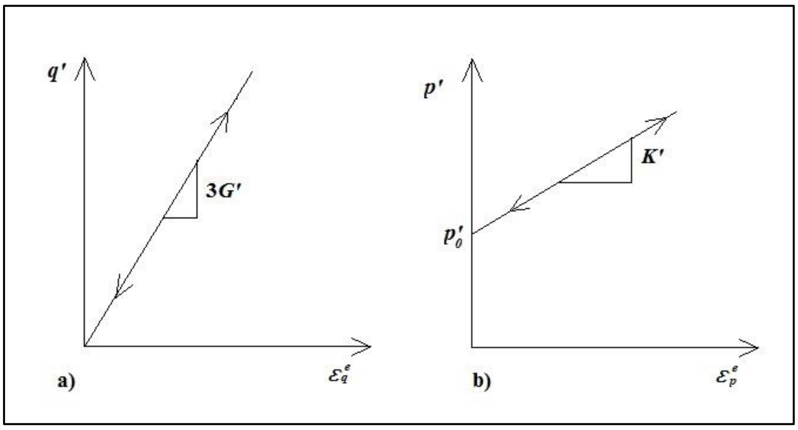

Figure 2.11 – Behaviour of linear elastic material (adapted from Atkinson, 1993)

- Yield function

In the multi-axial case, the stress has many components. So in order to define the onset of plastic straining, it is best to define a yield function, *f*, which depends on the stress and the state parameter.

$$F = f(p', q, \xi) = 0 \tag{2.4}$$

The value of this function identifies the type of material behaviour. F<0 represents a material with purely elastic behaviour (recoverable deformations) and F=0 represents elasto-plastic behaviour. It is impossible to have F>0 as above this boundary there is overall failure, therefore, no stress-strain equilibrium. The surface is a function of the stress state while the size is controlled by the state parameter. In case of perfect plasticity, the state parameter is constant. If the state parameter varies with plastic straining there is hardening or softening plasticity.

Figure 2.12 shows the yield function plotted in σ_1, σ_2 and σ_3. In a), σ_2 is equal to zero so the function is a curve while in b) σ_2 is allowed to vary so the yield function is plotted as a surface. The *elastic domain* is the space enclosed by this surface.

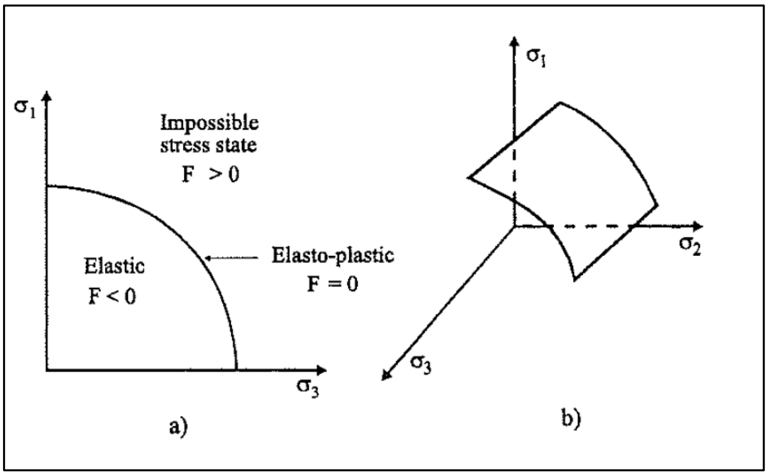

Figure 2.12 – Yield function (Potts and Zdravković, 1999)

- Plastic potential function

According to Muir Wood (1990), the plastic deformations depend on the stress state at which the yielding occurs. The yielding of a soil is associated with some plastic volumetric strain increment, $d\varepsilon_p^p$ and some plastic shear strain increment, $d\varepsilon_q^p$. If these components are plotted at a stress state where yielding occurs (*e. g.* point Y), with axes parallel to *p'* and *q*, a plastic strain increment vector (YS) is formed, as shown in Figure 2.13.

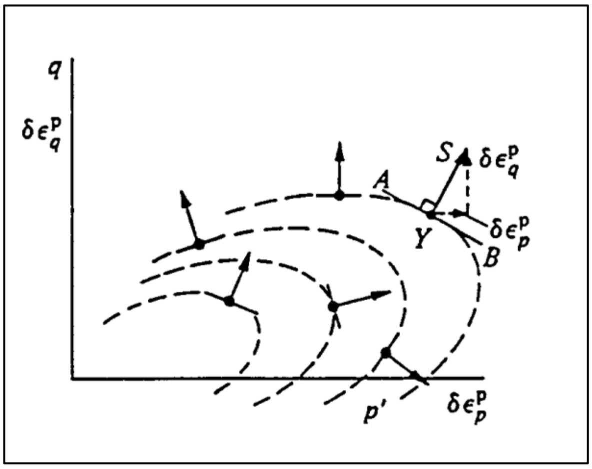

Figure 2.13 – Plastic strain increment vectors normal to a family of plastic potential curves (Muir Wood, 1990)

A line orthogonal to the plastic strain increment vector can be drawn (AB). Each combination of stress that causes yielding have a plastic strain vector associated and an orthogonal line can be drawn at each of those points. These lines can be joined to form a family of curves, known as plastic potentials. The relative magnitudes of the components of plastic deformation are defined by the direction of the outward normal to the plastic potential surface.

The plastic potential is defined by equation (2.5), where the parameter β controls the size of the plastic potential.

$$G = g(p', q, \beta) = 0 \tag{2.5}$$

In the multi-axial situation, it is necessary to specify the direction of plastic straining at every stress state which is done by the *flow rule*. If the yield function and the plastic potential are the same, the flow rule is *associated*, otherwise it is *non-associated*. In the case of associated flow rule, the vector that defines the increment of plastic strain is normal to the yield surface. In constitutive modeling, flow rules govern, or in other view, are conditioned by dilatancy effects, which influence volume changes and strength of the soil (Potts and Zdravković, 1999).

- Hardening/softening laws

As it was discussed before, when the soil reaches the yield stress and is strained further that point, it suffers irrecoverable plastic strains.

The hardening/softening rules define the variations on the state parameters with plastic straining. As it was explained before, if the material is perfectly plastic there is no need for hardening or softening rules because when the stress reaches yield it strains indefinitely. However, if the material suffers from hardening or softening, some rules have to be defined to evaluate the changes in the yield surface.

Observing Figure 2.9, it is notable that the yield stress increases with plastic strain (BCF). The definition of the increase of the yield stress with the plastic strain is known as hardening. On the other hand, in Figure 2.10 the yield stress decreases with plastic strain (softening). The relation that defines the decrease of the yield stress with plastic strained is called softening rule. In Figure 2.14 two examples of these relationships are represented.

To sum up, the hardening/softening law is the relationship between the changing in the yield locus and the plastic deformation and it describes the expansion/contraction of the yield surface. A model that simulates the behaviour of a real soil usually involves strain hardening and strain softening.

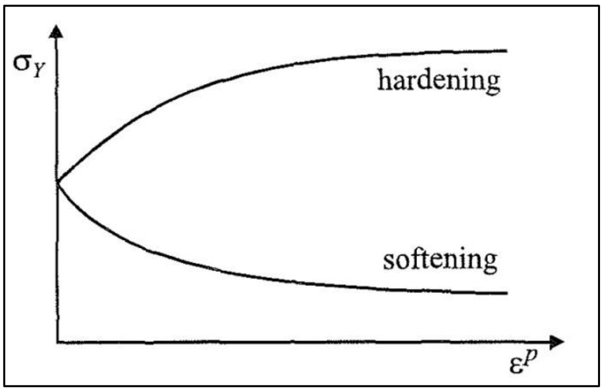

Figure 2.14 – Examples of hardening and softening rules (Potts and Zdravković, 1999)

2.2.5. TWO DIMENSIONAL BEHAVIOUR

To explain better these concepts, in this section it is considered a two dimensional situation. It is assumed that the yield and plastic potential functions are the same, in order to simplify the explanation.

If the material behaviour is linear elastic perfectly plastic, the yield surface position does not change when the material is loaded. Such behaviour is illustrated in Figure 2.15. If the stress state is below the yield surface the behaviour is elastic and if it reaches the yield surface plastic straining takes place. The stress state cannot go further the yield surface so when the stress reaches it (point b), it stays constant and plastic straining occurs. The ratio between $d\varepsilon_x^p$ and $d\varepsilon_y^p$ is fixed by the gradient of the yield surface (the same as the plastic potential because of the associated conditions considered) at point b so the element of soil failed (Potts and Zdravković, 1999).

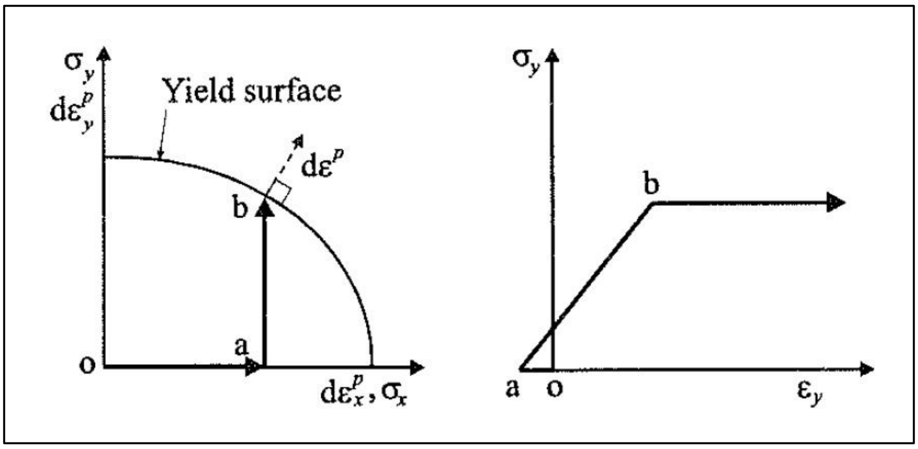

Figure 2.15 – Two dimensional behaviour of a linear elastic perfectly plastic material (Potts and Zdravković, 1999)

In the case of a linear elastic hardening plastic material, the yield surface changes size with plastic strain. In isotropic hardening, it stays centred in the same point but if it is kinematic hardening, the center point changes position but the yield surface does not change size, as it is exemplified in Figure 2.16. Hardening can include both types at the same time.

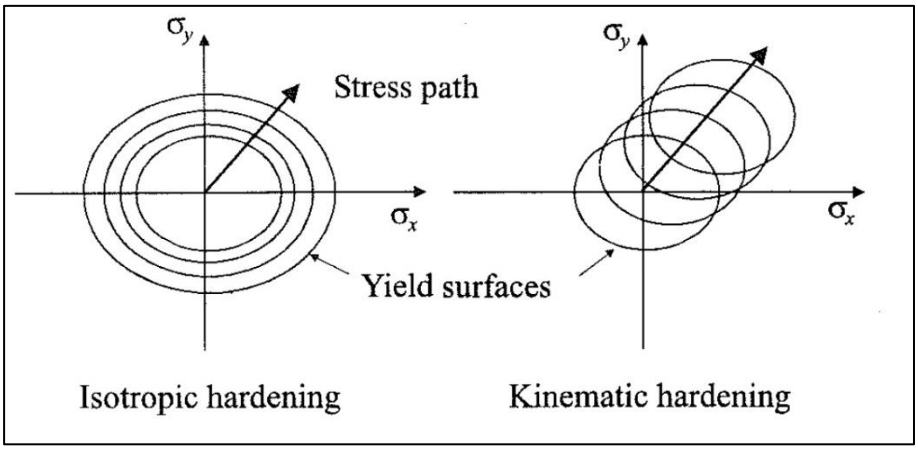

Figure 2.16 – Hardening types (Potts and Zdravković, 1999)

As it is shown in Figure 2.17, until the stress state reaches the yield surface, the material has an elastic behaviour. If the stress increases beyond point b, plastic deformation takes place, the yield surface changes size and expands (isotropic hardening). The soil behaviour is elasto-plastic so there is the development of both elastic and plastic strains. The ratio between $d\varepsilon_x^p$ and $d\varepsilon_y^p$ can change with the continued loading. Failure happens when the yield surface stops hardening.

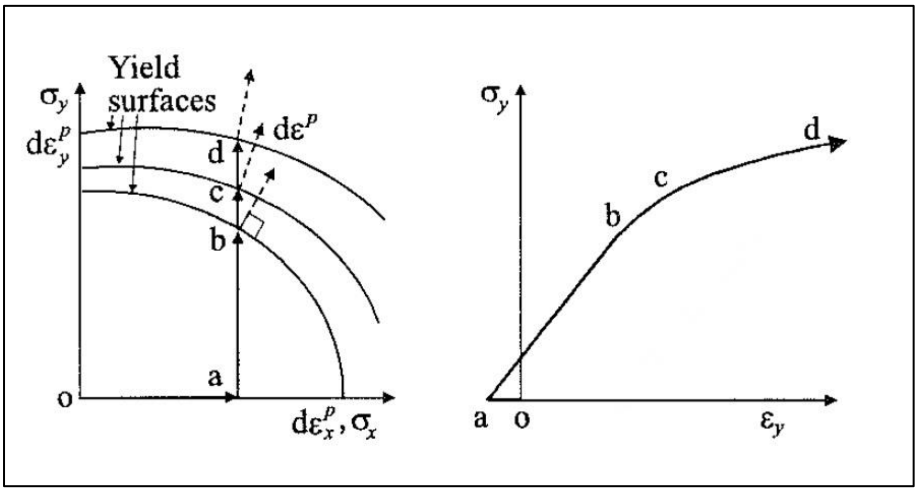

Figure 2.17 – Two dimensional behaviour of a linear elastic hardening plastic material (Potts and Zdravković, 1999)

In the case of a linear elastic softening plastic material, the yield surface reduces size with increasing of plastic strain (Figure 2.18). Once the point b is reached and plastic deformations occur, isotropic softening happens and the yield surface decreases its size. In that way, the stress σ_Y has to reduce. The strain softening stress-strain curve can be followed if the action is made in strain (ε_Y) control, which will be mostly impossible if the action is made under stress (σ_Y) control (Potts and Zdravković, 1999). Failure will also be defined when yield surface stops to shrink, which can be the extreme position in zero effective stress (i. e., liquefaction).

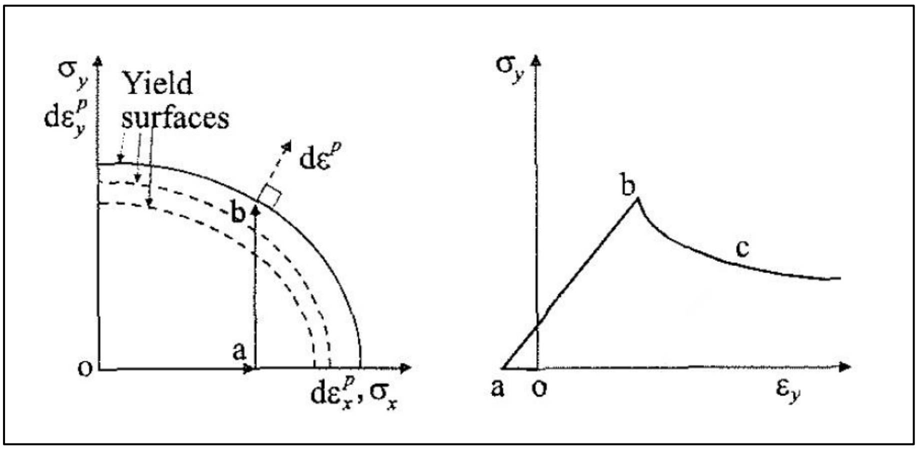

Figure 2.18 – Two dimensional behaviour of a linear elastic softening plastic material (Potts and Zdravković, 1999)

2.3. CRITICAL STATE THEORY

2.3.1. ISOTROPIC COMPRESSION

According to Atkinson (1993), the rearrangement of the grains is what causes soil compression or dilation. Initial stiffness can decrease when state is loos, while it will increase in dense states. During the loading, the stress-strain line is not linear therefore the mechanisms of volume change due to rearrangement of the grains accounts for non-linear bulk stiffness behaviour. On the unloading-reloading, the stiffness is higher than for the first loading as the grains cannot invert the rearrangement they suffered. Figure 2.19 shows the curve of isotropic compression and swelling on both linear and logarithmic horizontal scale and it represents the specific volume, υ, plotted against the mean effective stress, *p'*.

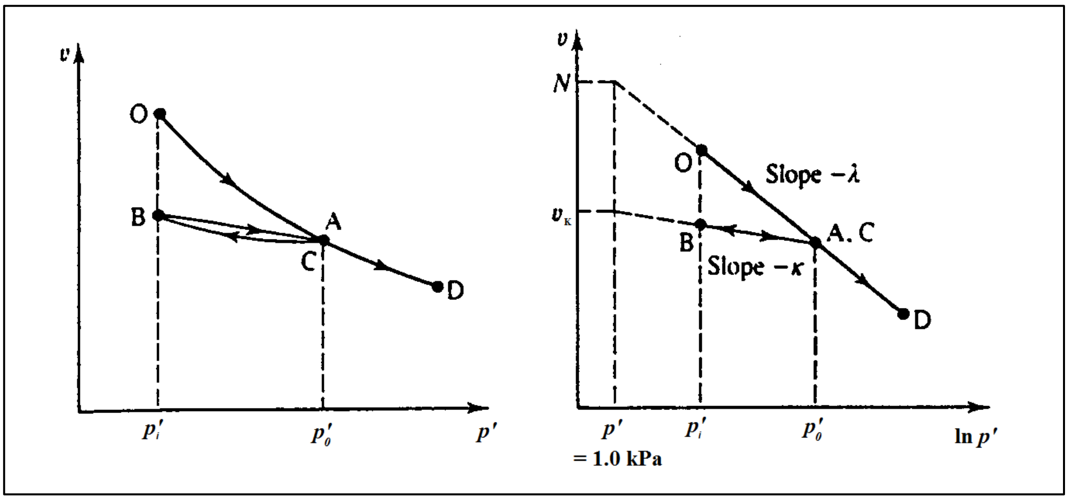

Figure 2.19 – Isotropic compression and swelling (adapted from Atkinson, 1993)

The line OACD is the normal compression line (NCL) and it represents the first loading. Its equation is given by expression (2.6).

$$\upsilon = N - \lambda \ln p' \tag{2.6}$$

The λ is the gradient and N is the value of υ when *p'*=1.0 kPa. The swelling line (also called unloading line) is ABC and it is given by equation (2.7).

$$\upsilon = \upsilon_\kappa - \kappa \ln p' \tag{2.7}$$

Where κ is the gradient and υ_κ is the value of υ when *p'*=1.0 kPa. The parameters λ, κ and N are constant for a certain soil, except if there is an evolution of particle size, due for instance to particle breakage. There are many swelling lines as the soil can be unloaded from any point of the NCL.

2.3.2. Wet and Dry Side of Critical State

Figure 2.20 represent the types of behaviour a soil has depending on whether it is on the wet or dry side of the critical state before shearing. A combination of pressure and specific volume define the state of the soil. The state of a conventional soil (that is, without interparticle cementation (bounding)) can never be above and to the right of the NCL (Roscoe et al., 1958). Heavily overconsolidated clays and dense sands are on the dry side (point A in Figure 2.20) while lightly overconsolidated clays or loose sands are on the wet side (point B in Figure 2.20).

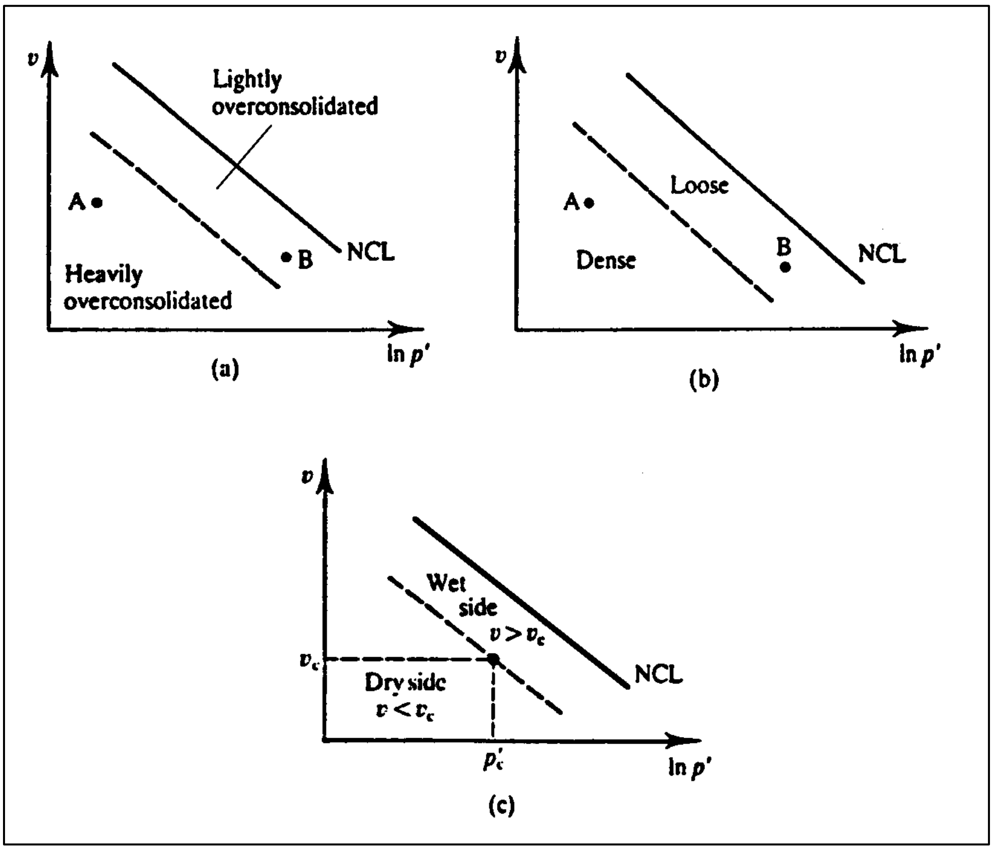

Figure 2.20 – State of soils on the wet and on the dry side of critical (adapted from Atkinson, 1993)

When submitted to shear tests (drained tests with constant σ’), the soils behave differently whether they are on the dry or wet side, as it is shown in Figure 2.21 (the soils on the wet side are marked W and on the dry side are marked D). Soils on the dry side have a peak before going to the ultimate (also known as critical) state while soils on the wet side increase only until the ultimate state. As for the volumetric strains, soils on the dry side experience a small compression and then dilate (expand) while soils on the wet side compress as the shear stresses increase. Both samples have the same effective normal stresses but they have different initial void ratio. However, when reaching the ultimate states, the void ratio is the same, e_f.

The peak state, observed in soils on the dry side, is normally reached at strains of the order of 1 % while the ultimate strains reached after strains higher than 10%. The peak state coincides with the point of maximum rate of dilation (Atkinson, 1993).

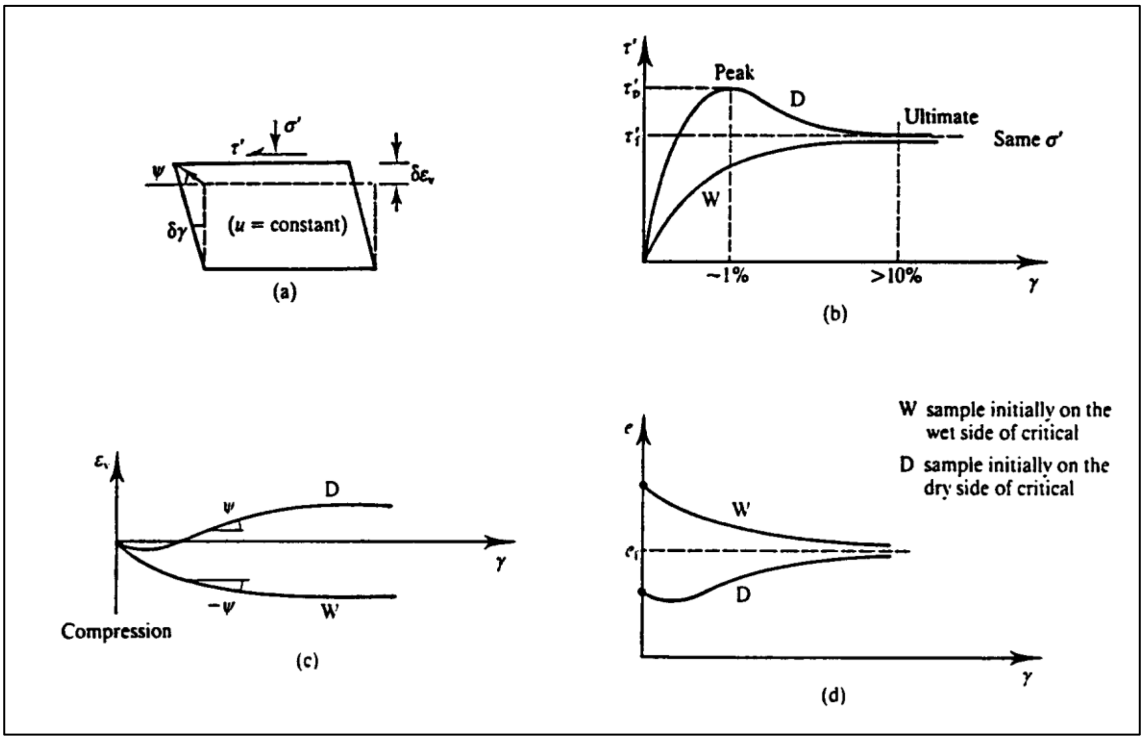

Figure 2.21 – Typical behaviour of soils in drained shear tests a) stresses applied; b) stress-strain curves; c) volume change curves; d) voids ratio change curves (Atkinson, 1993)

2.3.3. CRITICAL STATE LINE

According to Atkinson (1993), the critical state is the ultimate state reached after strains higher than 10% and it is defined as a combination of the voids ratio, shear stress and normal stress. These relationships are represented in Figure 2.22. The critical state line is defined by the equations (2.8) and (2.9).

$$\tau'_f = \sigma'_f \tan \phi'_c \tag{2.8}$$

$$e_f = e_\Gamma - C_c \log \sigma'_f \tag{2.9}$$

The suffix f means the ultimate failure at critical state. The parameter e_Γ represents the value of the voids ratio when the normal stress is 1.0 kPa (on the logarithmic scale) and the value of C_c is the slope of the CSL which is parallel to the normal compression line.

At the critical state, without any changes on the shear stress, normal stress or voids ratio, the soil continues to suffer shear strains which are associated with turbulent flow. The main characteristic of the critical states is that, during shearing, all soils will ultimately reach their critical states which are independent from the initial states (Atkinson, 1993).

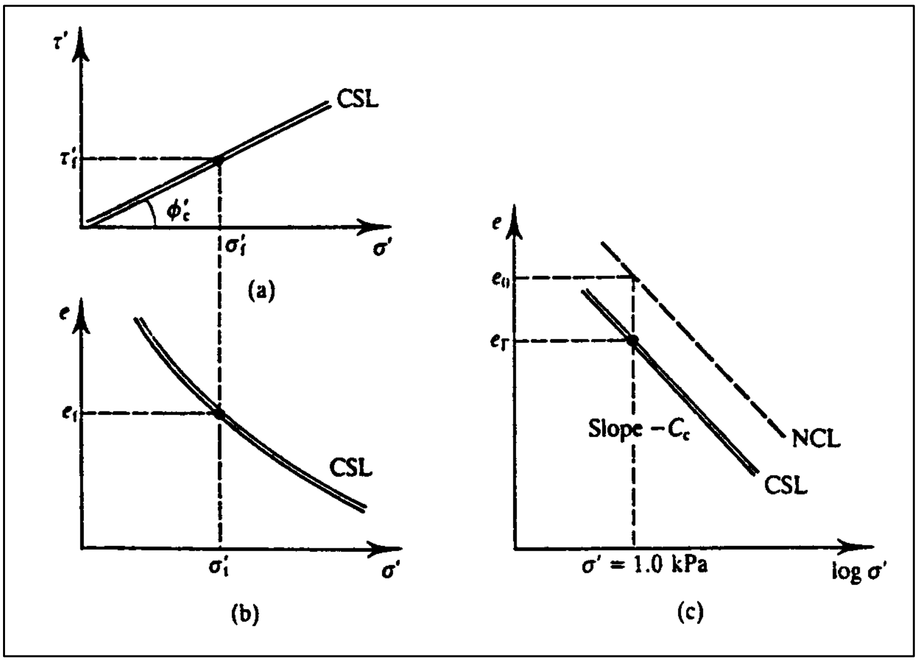

Figure 2.22 – Critical State Line a) shear stress against normal stress; b) voids ratio against normal stress; c) on logarithmic scale (Atkinson, 1993)

2.3.4. CRITICAL STATE IN TRIAXIAL TESTS

In triaxial tests the soil specimen is subjected to total axial and radial stresses. As the sample volume and pore pressures can be controlled and measured independently, it is possible to determine the strains and the effective stresses. The soil behaviour is the same as explained before but now the parameters are q', p', ε_p and ε_q which represent deviatoric stress, mean effective stress, volumetric strain and shear strain respectively. These parameters are described in equations (2.10) to (2.13). The suffixes *a* (for axial) and *r* (for radial) can be replaced by *1* and *3*, respectively, which are the principal directions. The principal direction 2 is equal to the principal direction 3 in conventional triaxial tests, where the vertical (or axial) stress is always higher than the radial. The following notations (Cambridge convention) will be adopted in the present work:

$$q' = \sigma'_a - \sigma'_r \tag{2.10}$$

$$p' = \frac{\sigma'_a + 2\sigma'_r}{3} \tag{2.11}$$

$$\varepsilon_p = \varepsilon_v = \varepsilon_a + 2\varepsilon_r \tag{2.12}$$

$$\varepsilon_q = \varepsilon_s = \frac{2}{3}(\varepsilon_a - \varepsilon_r) \tag{2.13}$$

,meaning the deviatoric stress, mean effective stress, volumetric strain and shear or deviatoric strain, respectively.

Figure 2.23 shows the critical state line for triaxial tests both drained and undrained. The expressions of the critical line are given by equations (2.14) and (2.15).

$$q'_f = Mp'_f \tag{2.14}$$

$$\upsilon_f = \Gamma - \lambda \ln p'_f \tag{2.15}$$

As before, *f* denotes ultimate failure at the critical states. The critical stress ratio M is the slope of the CSL in *p*'-*q* space and it can be related with the critical friction angle (ϕ'_c). The gradient of the CSL is λ and the parameter Γ represents the value of the specific volume, υ, when *p*' equals 1.0 kPa (on the logarithmic scale).

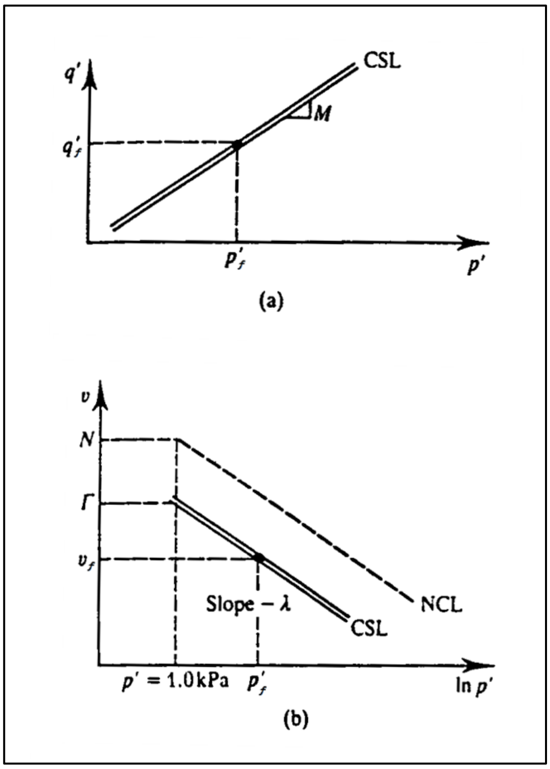

Figure 2.23 – Critical State Line for triaxial tests a) deviatoric stress against mean normal stress; b) specific volume against mean normal stress (on logarithmic scale) (Atkinson, 1993)

According to Atkinston (1993), the Mohr-Coulomb circle (corresponding to failure) can be used to relate triaxial and shear tests results. Figure 2.24 shows the Mohr-Coulomb circle for general stress ratios in triaxial tests. Equations (2.16) to (2.19) express the relations between some parameters (with the meaning in the Figure 2.24).

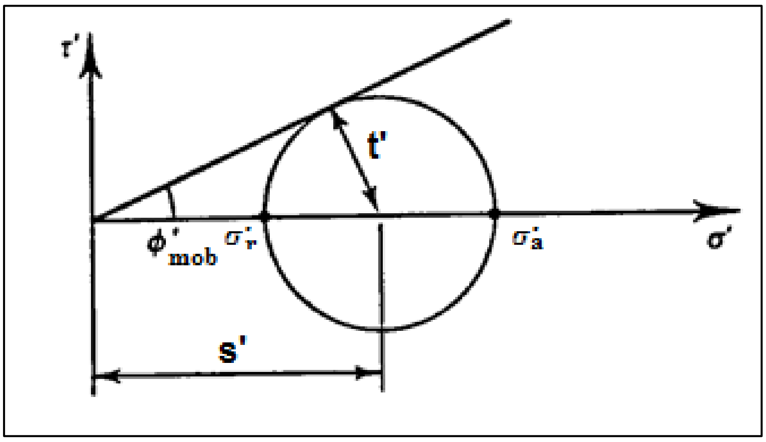

Figure 2.24 – Stress ratios in triaxial tests (Atkinson, 1993)

$$t' = \frac{1}{2}(\sigma'_a - \sigma'_r) \tag{2.16}$$

$$s' = \frac{1}{2}(\sigma'_a + \sigma'_r) \tag{2.17}$$

$$\frac{t'}{s'} = \sin\phi'_{mob} = \frac{\sigma'_a - \sigma'_r}{\sigma'_a + \sigma'_r} \tag{2.18}$$

$$\frac{\sigma'_a}{\sigma'_r} = \frac{1 + \sin\phi'_{mob}}{1 - \sin\phi'_{mob}} \tag{2.19}$$

At the critical state, $\phi'_{mob} = \phi'_c$. From equations (2.14) and (2.19), relationships between M and ϕ'_c can be obtained, as expressed in equations (2.20) and (2.21), for compression and extension respectively. Note that for compression, $\sigma'_a > \sigma'_r$ and for extension $\sigma'_a < \sigma'_r$.

$$M_c = \frac{6\sin\phi'_c}{3 - \sin\phi'_c} \tag{2.20}$$

$$M_e = \frac{6\sin\phi'_c}{3 + \sin\phi'_c} \tag{2.21}$$

2.3.5. NORMALIZATION

There are some methods of normalization of stresses and voids ratios, in order to simplify the presentation and the interpretation of the results. Focusing on the triaxial test results, the normalizing parameters are the critical pressure p'_c (that is, the value of the mean effective stress in the CSL for a specific void ratio) and the equivalent specific volume υ_λ, shown in Figure 2.25. It is often used the equivalent pressure on the normal compression line, p'_e, but as there are different NCL for isotropic and one-dimensional compression, it is preferable to use the critical pressure as a normalizing parameter.

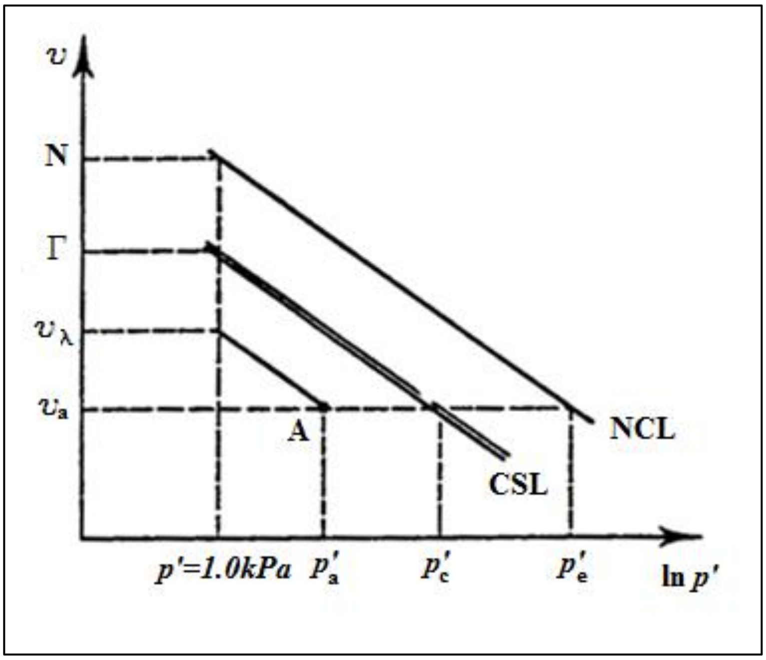

Figure 2.25 – Normalizing parameters for triaxial tests (Atkinson, 1993)

From Figure 2.25, equations (2.22) and (2.23) can be written.

$$\upsilon_\lambda = \upsilon_a + \lambda \ln p'_a \tag{2.22}$$

$$\ln p'_c = \frac{\Gamma - \upsilon_a}{\lambda} \tag{2.23}$$

The normalizing parameters are obtained by the NCL or CSL equation, using the value of the specific volume (which is the same as considering the corresponding void ratio: $\upsilon=1+e$) of the point that is being normalized (equations (2.24) and (2.25)).

$$p'_e = \frac{N - \upsilon}{\lambda} \tag{2.24}$$

$$p'_c = \frac{\Gamma - \upsilon}{\lambda} \tag{2.25}$$

The normalization consists in dividing the q and p' by the normalizing parameters. In this way the lines such as NCL and CSL or another parallel to these will be represented by a point in the new normalized plot, shown in Figure 2.26.

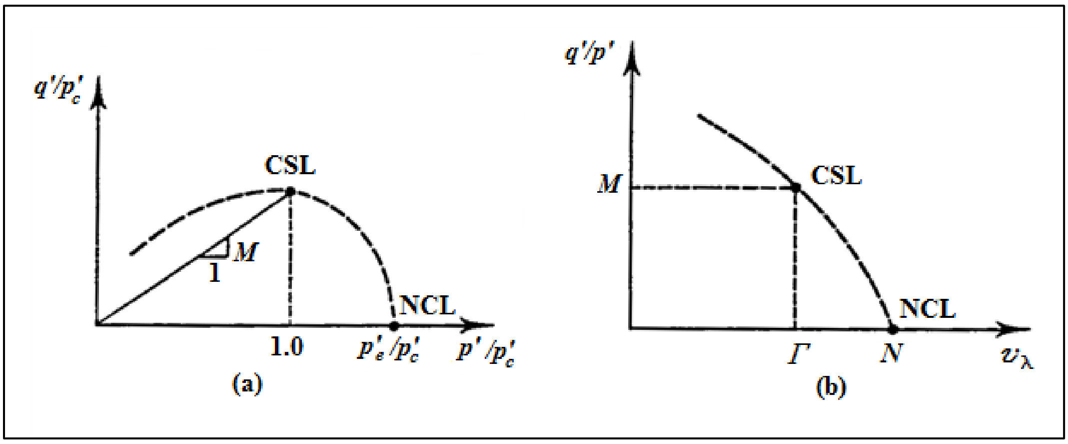

Figure 2.26 – Normalized CSL and NCL (Atkinson, 1993)

2.4. CAM-CLAY MODELS

Roscoe et al. (1958) developed the original Cam-clay model, named by the authors in reference to the river flowing in the vicinity of Geotech Lab in Cambridge University. Later, the modified Cam-clay model was proposed by Roscoe and Burland (1968). These were the first critical state models, developed at the University of Cambridge. Afterwards, a large number of new models have been proposed based on the Cam-clay models with the purpose of achieving a better adjustment between predicted and observed behaviour in different soils, such as sands, residual and cemented soils, etc.

A unified model for clays and sand was proposed by Yu (1998), with the name CASM (Clay and Sand Model). Its main feature is that a single yield function and plastic potential are used for both clay and sand under both drained and undrained conditions.

2.4.1. ORIGINAL CAM-CLAY

The Original Cam-clay model was described by Schofield and Wroth (1968). This model combines the Critical State Soil Mechanics and the idea of a state boundary surface essential to the theory of plasticity. The equation that defines the yield curve is shown in (2.26).

$$F = \frac{q}{p'} + M \ln \frac{p'}{p'_0} = 0 \tag{2.26}$$

Figure 2.27 represents the yield curve for the original Cam-clay model.

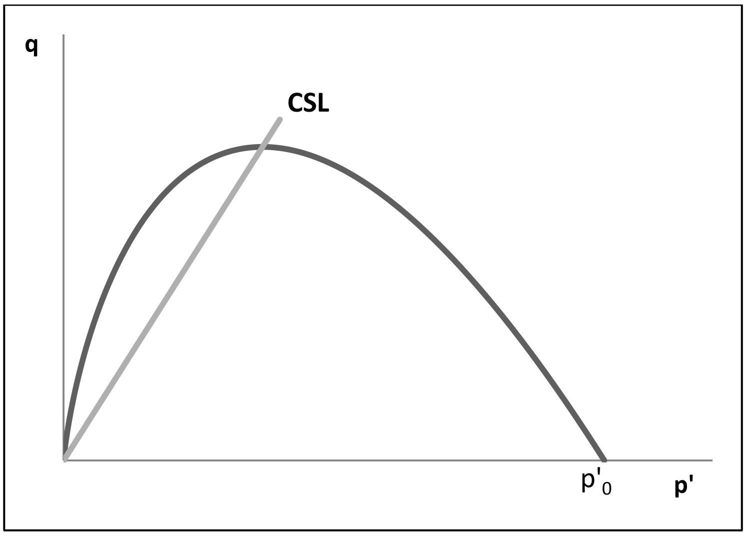

Figure 2.27 – Yield curve for original Cam-clay

This model is associated, so the yield function is identical to the plastic potential. The elastic law is defined by equations (2.27) and (2.28). The flow rule is expressed in (2.29) and the hardening law in (2.30).

$$dp' = \frac{(1+e)p'}{\kappa} d\varepsilon_p^e \tag{2.27}$$

$$dq = 3G d\varepsilon_q^e \tag{2.28}$$

$$\frac{d\varepsilon_p^p}{d\varepsilon_q^p} = M - \frac{q}{p'} \tag{2.29}$$

$$dp'_0 = \frac{(1+e)p'_0}{\lambda - \kappa} d\varepsilon_p^p \tag{2.30}$$

2.4.2. CASM – CLAY AND SAND MODEL

The Clay and Sand model (CASM), developed by Yu (1998), is a unified critical state constitutive model and it is based on the state parameter. The state parameter is defined as the difference between specific volume (or void ratio) and the specific volume (or void ratio) at the critical state at the same mean effective stress (Been and Jefferies, 1985). This parameter is very important when modelling sand behaviour. It depends on the specific volume ($\upsilon = 1 + e$, e being the void ratio), two critical state constants (λ and Γ) and the mean effective stress (p'). Its expression is given by (2.31). Figure 2.28 shows the definition of some of these parameters.

$$\xi = \upsilon + \lambda \ln p' - \Gamma \tag{2.31}$$

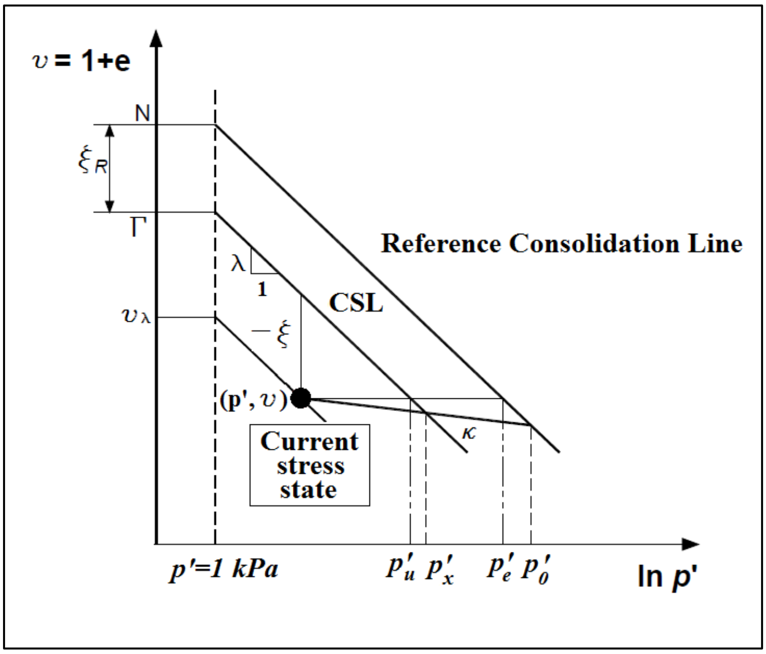

Figure 2.28 – Definition of state parameter, critical state constants and reference state parameter (Yu, 1998)

- Elastic component

CASM assumes the same elastic behaviour as the standard Cam-clay models, being the bulk and shear moduli defined by expressions (2.32) and (2.33). A constant value of Poisson's ratio (ν) is specified, so that the shear modulus varies with the bulk modulus and therefore with the stress level.

$$K = \frac{\upsilon p'}{\kappa} \tag{2.32}$$

$$G = \frac{3(1-2\nu)}{2(1+\nu)} K \tag{2.33}$$

- Yield function

The yield function of CASM is expressed in equation (2.34), where p' is the mean effective stress, q is the deviatoric stress and p'_0 is the preconsolidation pressure. The constant n is the stress-state coefficient and specifies the shape of the yield surface and r is the spacing ratio.

$$F = \left(\frac{q}{Mp'}\right)^n + \ln\left(\frac{p'}{p'_0}\right)\frac{1}{\ln r} \tag{2.34}$$

Knowing that parameter ξ_R is the reference state parameter obtained by equation (2.35) and the spacing ratio is defined by equation (2.36), the geometry shown in Figure (2.28) allows to write the equation (2.37) (Yu, 1998).

$$\xi_R = (\lambda - \kappa)\ln r \tag{2.35}$$

$$r = \frac{p'_0}{p'_x} \tag{2.36}$$

$$\frac{\xi}{\xi_R} = \frac{-(\lambda - \kappa)\ln(p'_x/p')}{(\lambda - \kappa)\ln r} = 1 + \frac{\ln(p'/p'_0)}{\ln r} \tag{2.37}$$

Replacing equation (2.37) into the equation of the yield function (2.34), the yield function can be defined in terms of state parameter, as follows:

$$F = \left(\frac{q}{Mp'}\right)^n + \frac{\xi}{\xi_R} - 1 = 0 \tag{2.38}$$

If the parameters n and r are replaced by 1 and 2.718, respectively, the yield function reduces to the original Cam-clay yield surface.

- Plastic potential

The plastic flow rule used in CASM is non-associated, so the yield function and the plastic potencial are different. According to Yu (1998), the stress-dilatancy relation used in the model is due to Rowe (1962), as it succeeded in describing the deformation of sands and other granular materials. The dilatancy rate is defined in equation (2.39), where $\eta = q/p'$.

$$d = \frac{\delta\varepsilon_p^{\mathrm{p}}}{\delta\varepsilon_q^{\mathrm{p}}} = \frac{9(M - \eta)}{9 + 3M - 2M\eta} \tag{2.39}$$

The plastic potential is obtained by the integration of Rowe’s stress dilatancy relation and it is expressed on equation (2.40), where β is the size parameter and can be determined by solving that equation for any given stress state (p', q).

$$g(p', q, \beta) = 3M\ln\frac{p'}{\beta} + (3 + 2M)\ln\left(\frac{2q}{p'} + 3\right) - (3 - M)\ln\left(3 - \frac{q}{p'}\right) = 0 \tag{2.40}$$

- Hardening rule

CASM postulates that the hardening law is of the isotropic volumetric plastic strain hardening type (Yu, 1998). The change in size of the yield surface is related to the incremental plastic volumetric strain, as shown in equation (2.41).

$$dp'_0 = \frac{(1+e)p'_0}{\lambda - \kappa} d\varepsilon_p^p \tag{2.41}$$

In appendix A the equations for the implementation of CASM are exposed.

3

CASE HISTORY: THE BOUMERDÈS EARTHQUAKE, ALGERIA (2003)

3.1. DESCRIPTION OF THE CASE

On May 21, 2003, an earthquake occurred in Boumerdès, a province located in the north of Algeria, close to the capital, Algiers. It was one of the most destructive earthquakes seen in the past years with a magnitude of 6.8, Richter scale. Since January 1716, when a severe earthquake destroyed Algiers, this was the worst seismic event in the region and caused a lot of structural damages and claimed the lives of 2271 people, injured more than 10000 and left about 160000 homeless (Bouhadad *et al*., 2004). The shock was so violent that it was felt on the Spanish and French coasts and on Italy (Genoa). To evaluate the severity of the damages, and based on the observed effects and press reports, an intensity of IX (Destructive) on the MSK scale was attributed to the epicentral area. Foundations of buildings lying on sand where liquefaction occurred, suffer a sudden loss of support, giving rise to differential settlements and consequently inducing structural damages. In Figure 3.1 some damages in buildings and transportation systems are illustrated.

Figure 3.1 – a) Total displacement of the first floor; b) Elementary school in Corso, insufficient lateral resisting system; c) Damage to Highway 5 Bridge; d) Several floors pancaked (EERI, 2003)

Many liquefaction occurrences were documented especially on the coastline and areas near the river. The liquefaction features vary in size and morphology. Figure 3.2 shows some regions affected by this phenomenon.

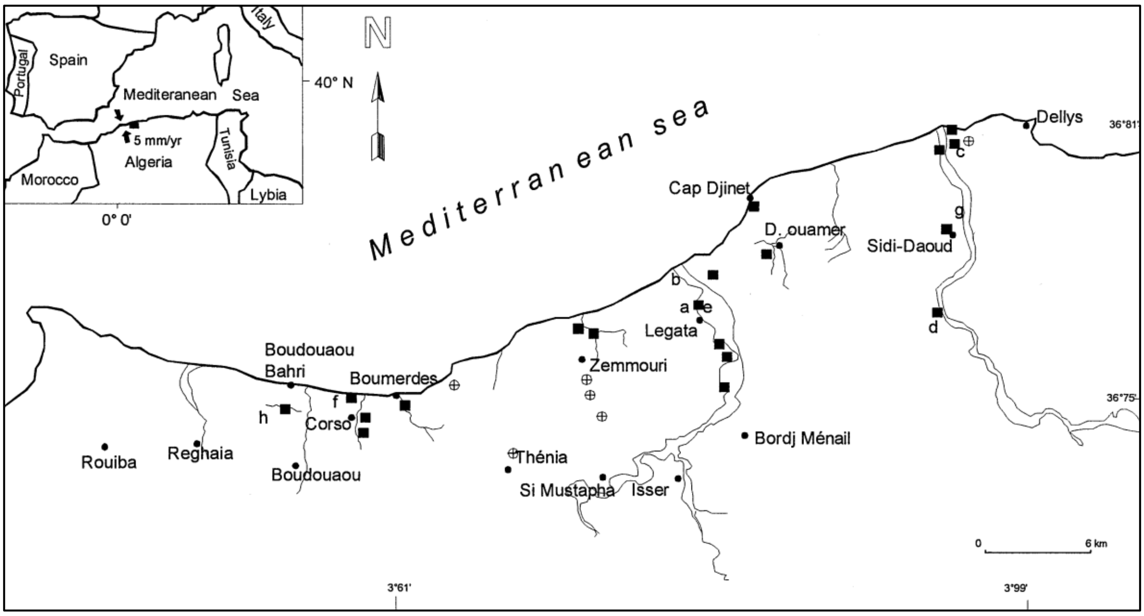

Figure 3.2 – Distribution of liquefaction during the Bourmedès earthquake (Bouhadad *et al*., 2004)

The earthquake triggered the sand liquefaction and excess water came to the ground surface (*sand boils*) causing landslides and cracking near the Isser River. The cracking appeared on both banks of the river causing the scattering of soil into the river. As the Isser River has a large solid flow a lot of sand was transported downstream to the Mediterranean Sea, as it is observed in Figure 3.3, an image from Google-Earth®.

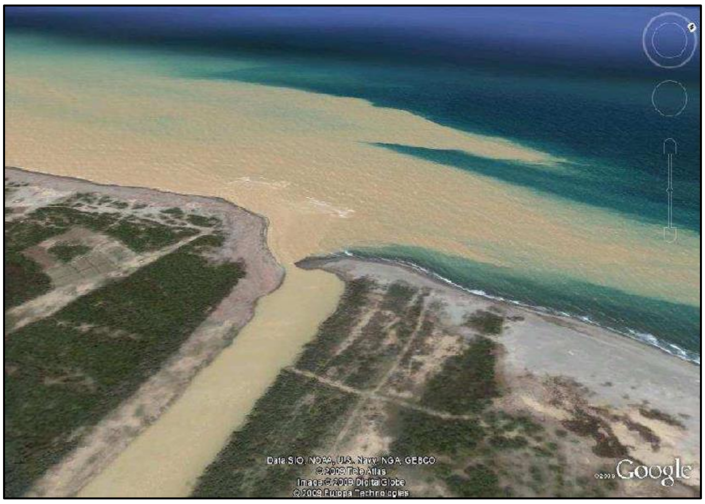

Figure 3.3 – Sand flow on Isser River, 22 May 2003 (Google)

Examples of these features of liquefaction are shown on Figure 3.4. The *sand boils* (Figure 3.4 b)) caused damage to roads and the collapse of houses. Big craters were also observed together with boiled sand and ground fissures due to differential settlements and soil collapse (Figure 3.4 a) and c)). Figure 3.4 d) shows the damage caused by loss of ground support when the soil liquefaction pushed down part of a pavement.

Figure 3.4 – a) Cracking; b) *Sand boils*; c) and d) damage on roads due to liquefaction (EERI, 2003)

3.2. MATERIAL DESCRIPTION

The material that was used in the laboratory studies is sand from *Les Dunes* beach, located in Ain Beninan in Algiers, where liquefaction was observed. The original soil is a siliceous medium sand with uniform particle size with grains fairly regular and slightly angled (Figure 3.5).

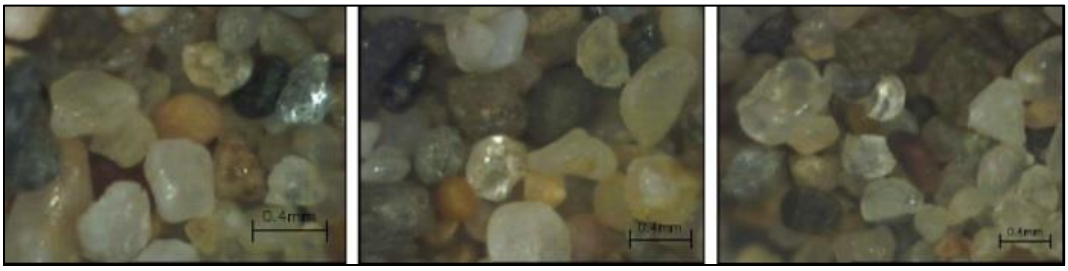

Figure 3.5 – Particles of *Les Dunes* sand

Figure 3.6 shows two soil gradation curves for this sand. The light blue curve was developed by Ghili Tahar at *Laboratoire GIENA*, in Faculty of Civil Engineering of Argel, and the dark blue was obtained at LabGEO in Faculty of Engineering of the University of Porto (FEUP), being this confirmed several times during the experimental program developed herein.

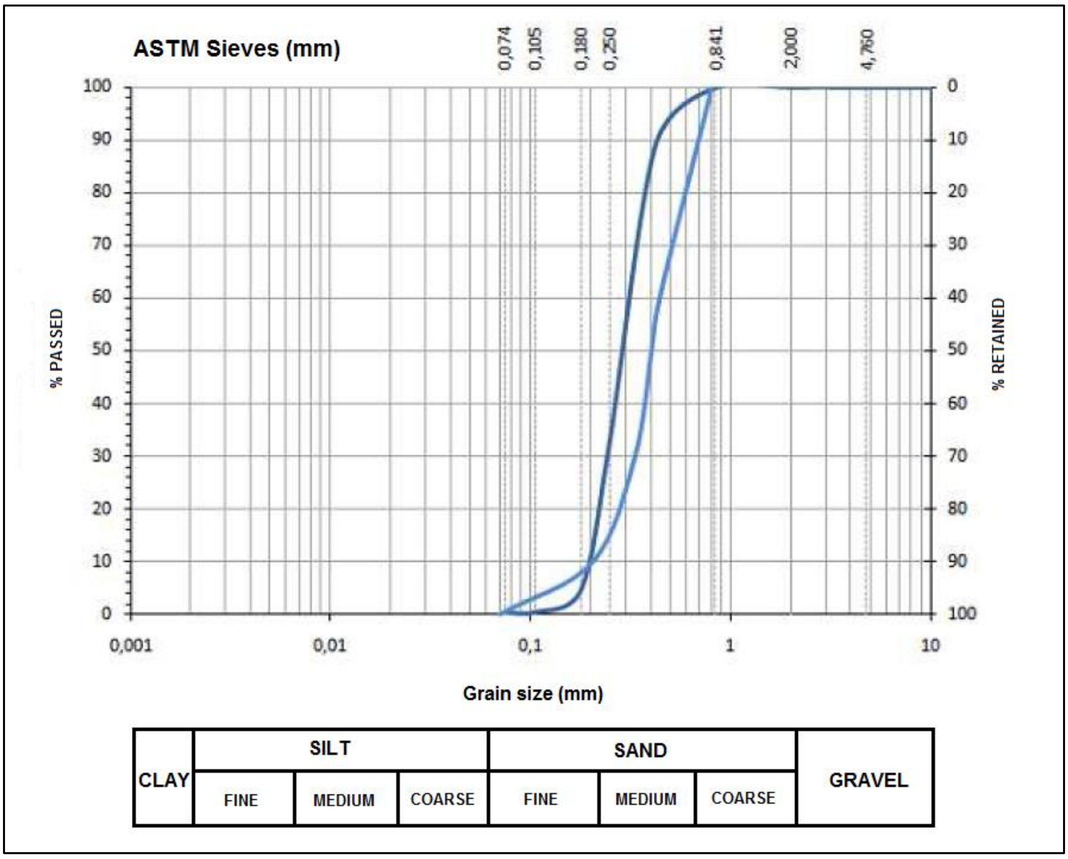

Figure 3.6 – Soil gradation of Les Dunes Sand

According to the curve determined by Ghili Tahar, the effective diameter, D_{10}, is 0.204 mm and represents the grain diameter of the sieve through which 10% of the weight of particles passes. The values of D_{30}, D_{60} and D_{100} are 0.331 mm, 0.439 mm and 0.800 mm, respectively, and have the equivalent meaning as D_{10}.

The coefficient of uniformity, C_U, gives an idea of the diversity of the particles sizes and it is given by the equation (3.1). A high value of C_U corresponds to a well graded soil and a low value of C_U corresponds to a poor graded soil. According to the Unified Soil Classification System, a well graded soil has C_U values higher than 4 (for gravels) or 6 (for sands). When C_U is close to the unit, the soil is said to be uniform.

$$C_U = \frac{D_{60}}{D_{10}} \tag{3.1}$$

The coefficient of curvature, C_C, can be correlated to the particles' shape and is given by the equation (3.2). A soil is considered well graded when the value of C_C is between 1 and 3.

$$C_C = \frac{(D_{30})^2}{D_{10} \times D_{60}} \tag{3.2}$$

According to the light blue curve in Figure 3.6, the coefficient of uniformity is C_U=2.15 and the coefficient of curvature is C_C= 1.22 revealing a poorly graded soil. The values of these coefficients determined in LabGEO (dark blue curve) are C_U=1.55 and C_C=1.01. Comparing the sand gradation exposed in Figure 3.6 with the boundaries in the boundary curves for liquefiable soil and potentially liquefiable soil (Figure 2.7), it is possible to note that the gradation curves for *Les Dunes* sand are located between the boundaries for the most liquefiable soil. As the sand is poorly graded, one can expect that it is susceptible to liquefy under loading.

The minimum and maximum density and void ratio are represented on Table 3.1. They were determined by Ghili (2003) according to the recommended procedure of the Japanese Society of Soil Mechanics for fine sands (D_{100} < 2 mm) with less than 5 % of fines (≈ #200, ASTM). Following studies performed at FEUP showed that it is possible to obtain a higher value of $e_{máx}$, but that is not relevant for this particular study.

Table 3.1 – Densities and void ratios

$\gamma_{d,min}$ (kN/m^3)	13.96	$e_{máx}$	0.890
$\gamma_{d,máx}$ (kN/m^3)	17.24	e_{min}	0.531

Fonseca (2009) and Pinheiro (2009) determined the value of the friction angle at critical state with data from the drained and undrained tests that did not liquefied until an axial strain of 20%. In Figure 3.7 the results of those tests are plotted, in t-s’ space. By defining a linear regression with those points, the slope of that line is equal to the tangent of the line angle (α). The friction angle is obtained with the expression of equation (3.3).

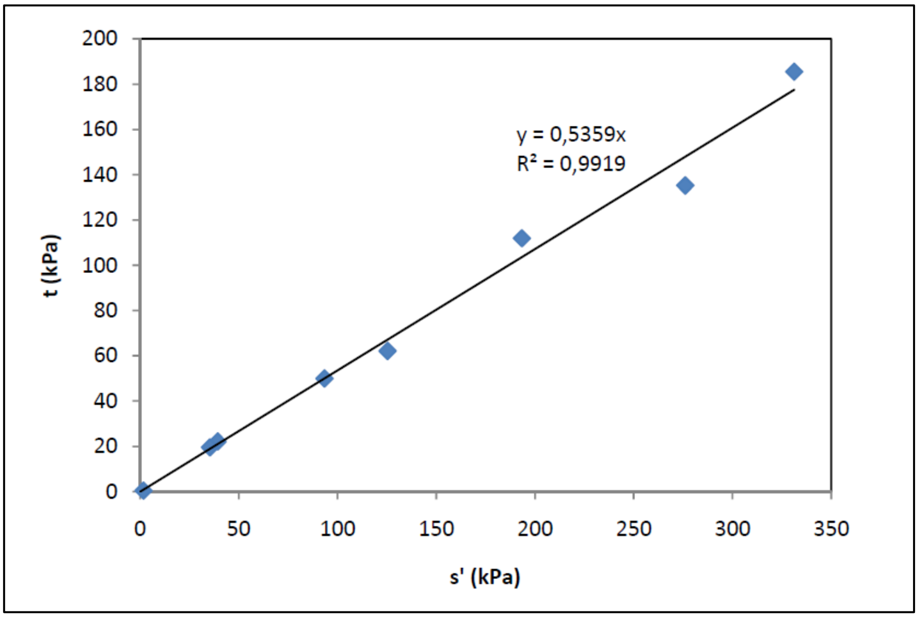

Figure 3.7 – Definition of the K_f line (Fonseca, 2009)

$$\phi' = \arcsin(\tan\alpha) = \arcsin(0.5359) = 32.4° \qquad (3.3)$$

3.3. PREVIOUS STUDIES

3.3.1. THE TRIAXIAL TEST

The triaxial test is a shear strength test suitable for all types of soil. It is conducted on a triaxial cell. An example of this equipment is represented in Figure 3.8.

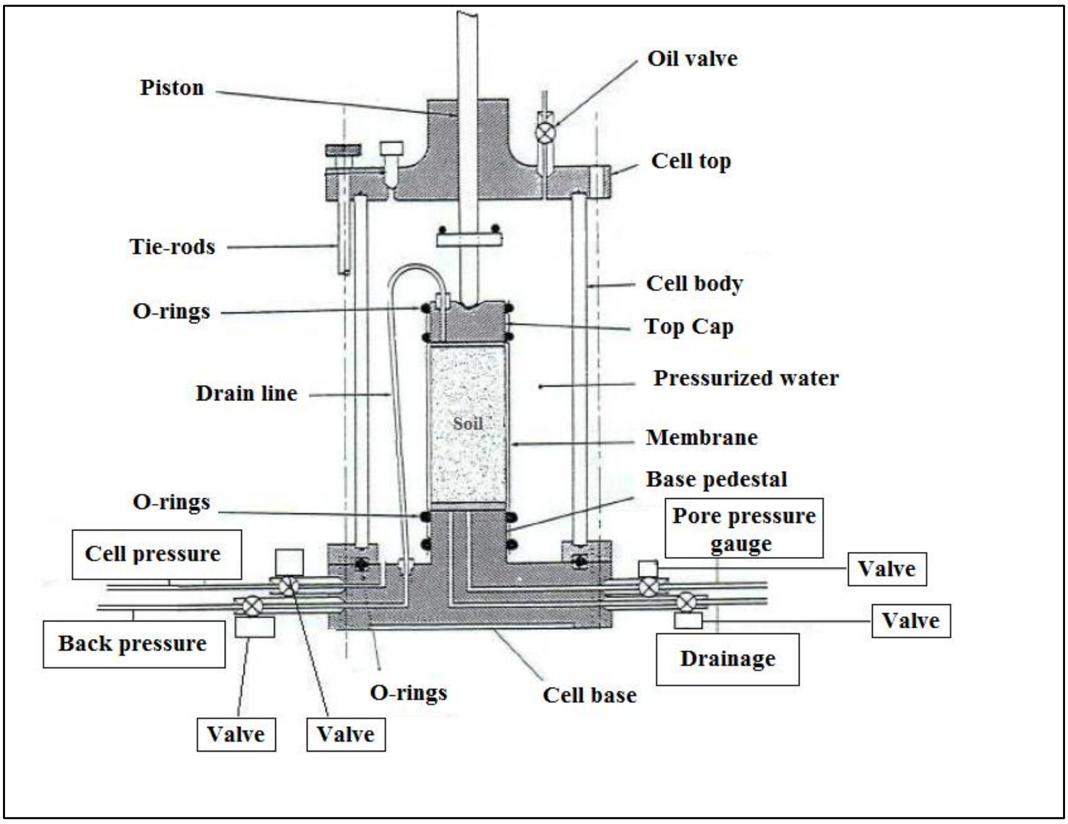

Figure 3.8 – The triaxial apparatus (adapted from Head and Epps, 2011)

The static triaxial test is divided in five different stages: preparation of the specimen and installation on the triaxial cell, percolation, saturation, consolidation and loading.

The specimen is prepared according to the *moist tamping* technique, which is commonly used for the preparation of sandy or silty soils to get high void ratios, that is, very loose states. This method although proving to be very efficient for obtaining high values of void ratio (Rocha, 2010) may be criticized for inducing a distinct fabric to the soil when compared with natural deposition (more details in Viana da Fonseca and Soares, 2011). The specimen is placed on the base pedestal, from which the drainage and pore pressure measurement systems access. A value of the moisture content (w) of 5 % was reached as the ideal for the implementation of this technique in this soil (Fonseca, 2010).

The next stage is percolation. During this phase, the voids are filled with water so that all the air is expelled from the specimen. The percolation must be performed from bottom to top of the specimen, in order to facilitate the expelling of the air, with a minimum effective stress around 10 kPa to 15 kPa.

It should be maintained until the percolated volume equals twice the voids' volume. In the casa this is not achieved a prior percolation with CO2 is advised to facilitate the process.

The saturation is performed by application of neutral pressure, gradually increasing, maintaining the effective stress constant. This allows the elimination of the air in the specimen (Fonseca, 2009). All tests were conducted by applying on increasing back pressure until 500 kPa (BD) while the cell pressure (CP) reached 515 kPa. It starts with CP = 25 kPa and BP = 10 kPa and the rate of increase is 30 kPa/hour, using an automatic control system developed in FEUP. The saturation level is controlled by the Skempton parameter B, which is defined on equation (3.4), where Δu is the excess pore pressure and $\Delta\sigma_3$ is the increment of total radial stress. If its value is close to 1, the specimen is saturated.

$$B = \frac{\Delta u}{\Delta \sigma_3} \tag{3.4}$$

The objective of the consolidation is to reproduce the *in situ* conditions of the material, regarding the stress state. It consists on the increase of the effective stresses through the increase of the cell pressure, maintaining the back pressure constant. All tests were performed after an isotropic consolidation.

The stage of consolidation is done under drained conditions, that is it will be concluded when there is no excess pore pressures and the volume variation is null. Although the consideration of isotropic consolidation for this type of material is not completely realistic, for the static triaxial tests the isotropic consolidation was adopted by easiness and taking into account that the K_0 values would not give different results (Rocha, 2011).

The loading consists on the application of a vertical upward strain of the base. The velocity used was 0.02mm/min so there was complete dissipation of excess pore pressure in the drained tests and the excess pore pressure was homogeneous along all the volume of the specimen for the undrained tests. If the test is drained, the drainage valve is open and if the test is undrained the valve is closed. In undrained tests, as the valve is closed and the sample is saturated, there is no volumetric deformation so it can be admitted that the void ratio is constant. For the control and monitoring of the test it was used a software developed at FEUP named MULTIGEO.

3.3.2. DESCRIPTION OF THE LABORATORY TEST RESULTS

For this work some results of triaxial tests performed by Pinheiro (2009), Rocha (2010) and Soares (2012) were used. Table 3.2 shows a summary of those tests and some of their main characteristics. All the specimens were isotropically consolidated. The CID tests were performed under drained conditions while the CIU tests were performed under undrained conditions. The relative density (D_r) is obtained by equation (3.5), using the values of e_{max} and e_{min} from Table 3.1. Low values of D_r mean that the sand is very loose.

$$D_r = \frac{e_{max} - e_0}{e_{max} - e_{min}} \tag{3.5}$$

Table 3.2 – Summary of triaxial tests performed

Author	Designation triaxial test	Type of Test	K_0	σ'_v (kPa)	e_0	D_r (%)
Pinheiro (2009)	LD12	CIU	1	200	0.885	1.4
Rocha (2010)	LD42	CIU	1	23	0.897	-
	LD44	CIU	1	30	0.901	-
	LD45	CIU	1	100	0.873	4.6
	LD46	CIU	1	400	0.848	11.8
	LD48	CIU	1	1000	0.844	12.8
	LD63	CID	1	500	0.850	11.1
	LD64	CID/CIU	1	1000	0.859	8.6
	LD65	CID	1	15	0.902	-
Soares (2012)	2º_2nd stage	CIU	1	520	0.796	26.2
	3º_2nd stage	CID	1	1000	0.782	30.1
	4º_2nd stage	CIU	1	1500	0.808	22.7

In Figure 3.9, the stress-paths of undrained tests with confining pressures of more than 400 kPa are shown. As it is observed, the mean effective stress decreases until it reaches the Critical State Line (CSL). As for the deviatoric stress, it increases until a peak, which is going to be studied later in this thesis, and then starts decreasing until it reaches the CSL, when it inflects, increasing again along the CSL. As it is verified, for these tests, the liquefaction phenomenon does not occur because the effective mean stress does not drop to zero. When the stress path reaches the “phase transformation” point, it starts increasing again and follows the critical state line. For better understanding and representation of the stress-path curves, the undrained tests were divided in two groups, one for the tests with confining pressures of more than 400kPa and other for the tests with confining pressures of less than 200kPa.

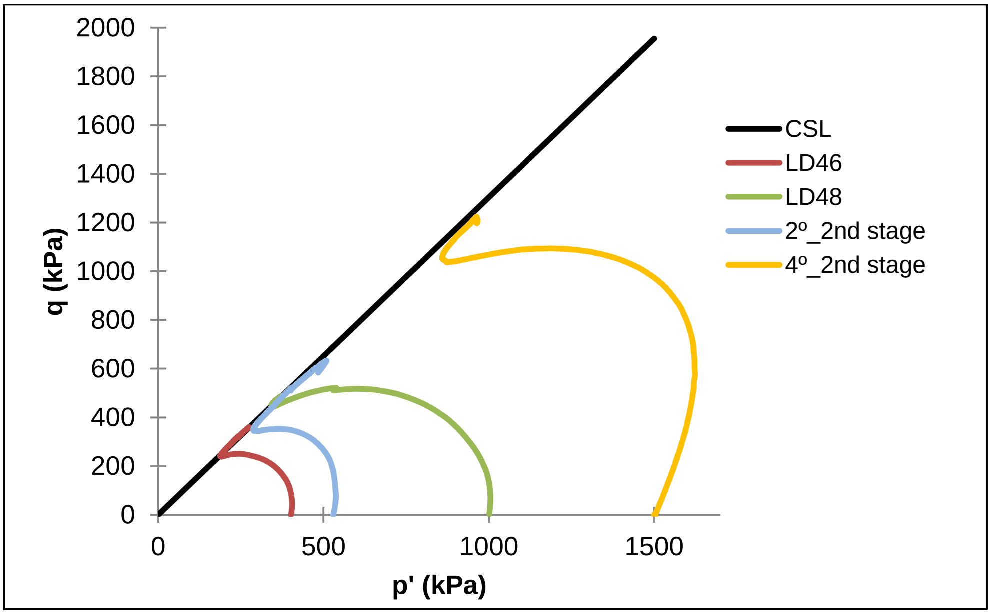

Figure 3.9 – Stress-path for undrained tests with more than 400kPa of confining pressure

Figure 3.10 shows the results of the undrained tests with confining pressures of less than 200 kPa. At first the shearing resistance goes up to a peak value of the deviatoric stress that is going to be explained later in this thesis as being the point where the specimen becomes unstable. After this point, the deviatoric and the mean effective stresses both tend to decrease until zero so it is notable that the samples suffer flow liquefaction.

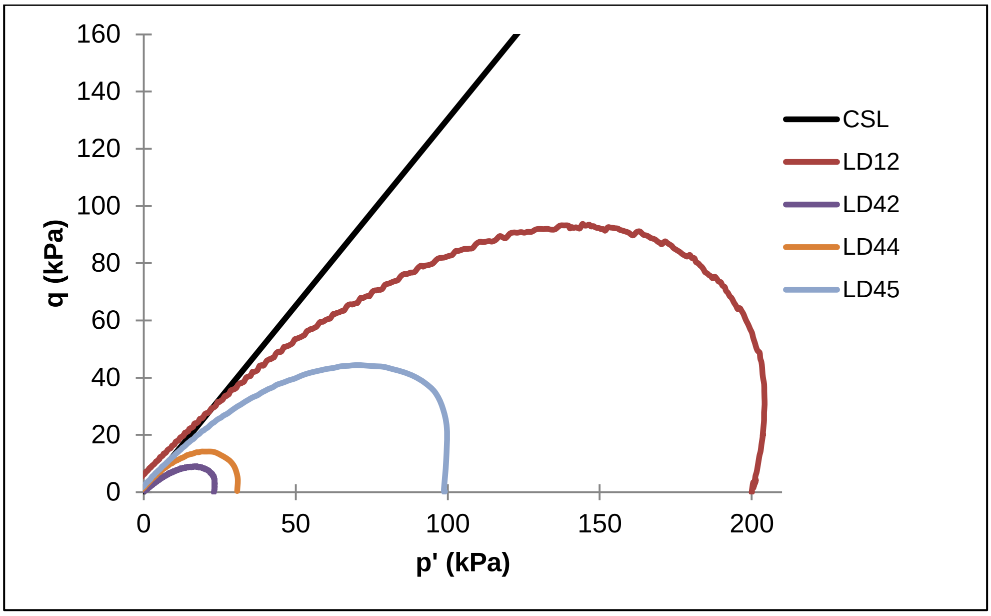

Figure 3.10 – Stress-path for undrained tests with less than 200kPa of confining pressure

The stress-paths of the drained tests are presented in Figure 3.11 where it is observed that both deviatoric and mean effective stresses increase with a slope of 3. LD64 is a particular case that is only represented as an example. This test starts to be drained but then, due to the limitation of the capacity of the internal load cell selected for the test, the CP valves had to be closed and the test becomes undrained. The stress-path exhibits that. At first it follows a typically drained path, with both deviatoric and mean effective stresses increasing but then, when it changes from drained to undrained conditions, the stresses decrease like it happens after the peak of deviatoric stress on the stress-paths represented in Figure 3.10 for undrained tests.

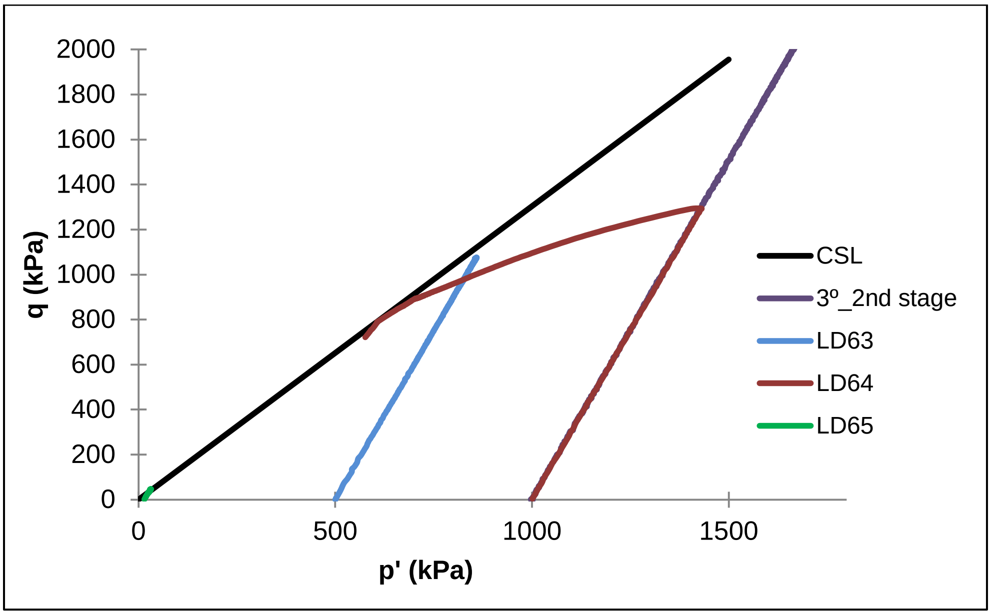

Figure 3.11 – Stress-path for drained tests

In Figure 3.12 to Figure 3.14 the deviatoric stress *versus* axial strain of the triaxial tests performed are represented.

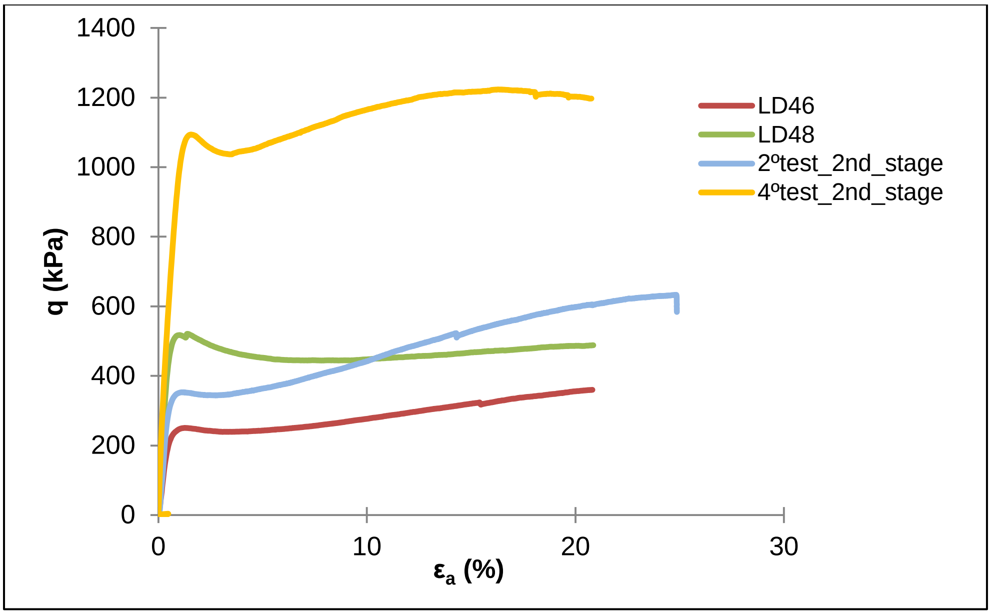

Figure 3.12 – Deviatoric stress *versus* axial strain for undrained tests with more than 400kPa of confining pressure

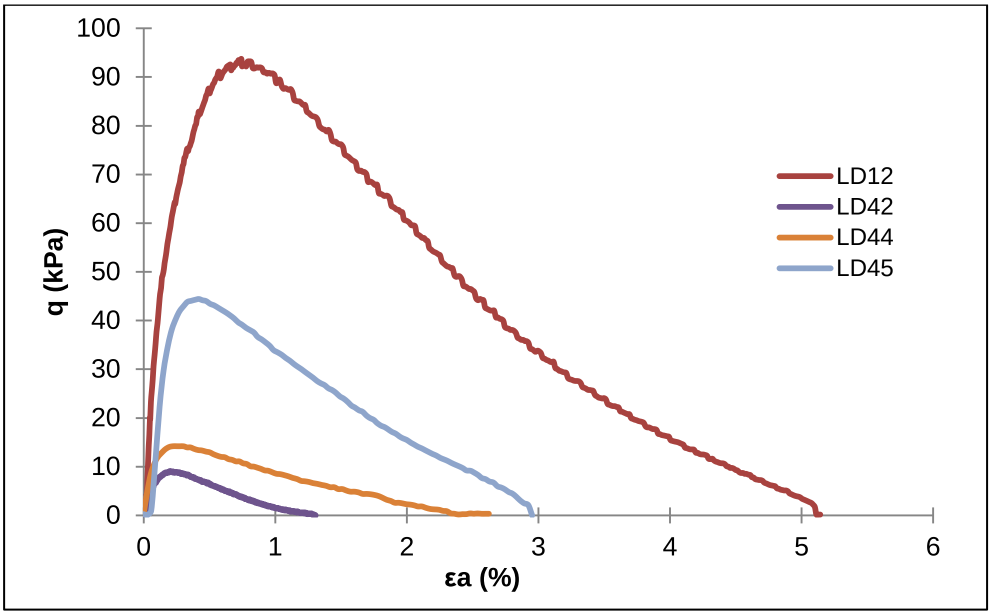

Figure 3.13 – Deviatoric stress *versus* axial strain for undrained tests with less than 200kPa of confining pressure

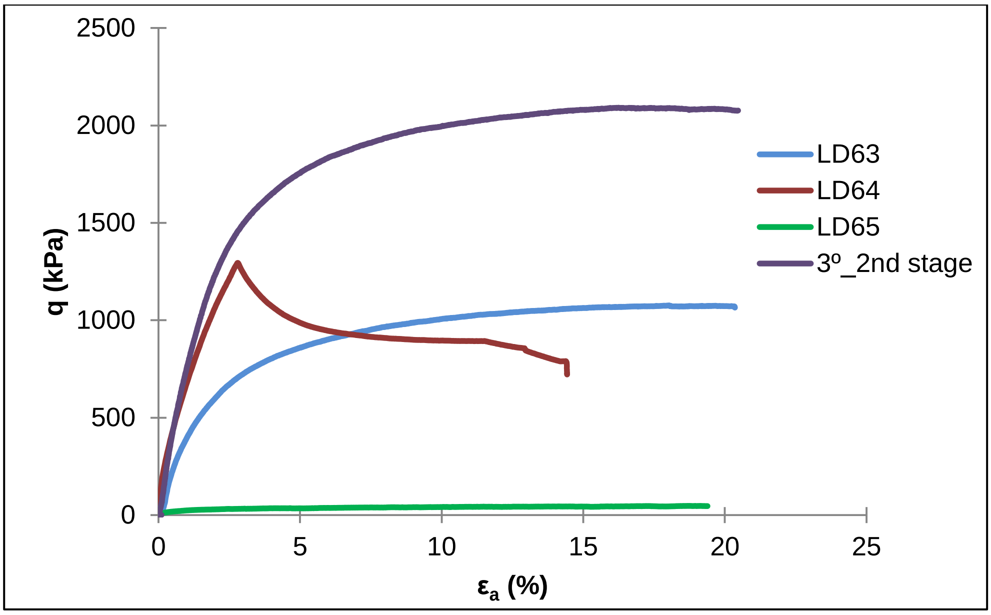

Figure 3.14 – Deviatoric stress *versus* axial strain for drained tests

In Figure 3.15 and Figure 3.16 the excess pore pressure *versus* axial strain for the undrained tests is shown and in Figure 3.17 the volumetric strain is plotted against the axial strain for the drained tests.

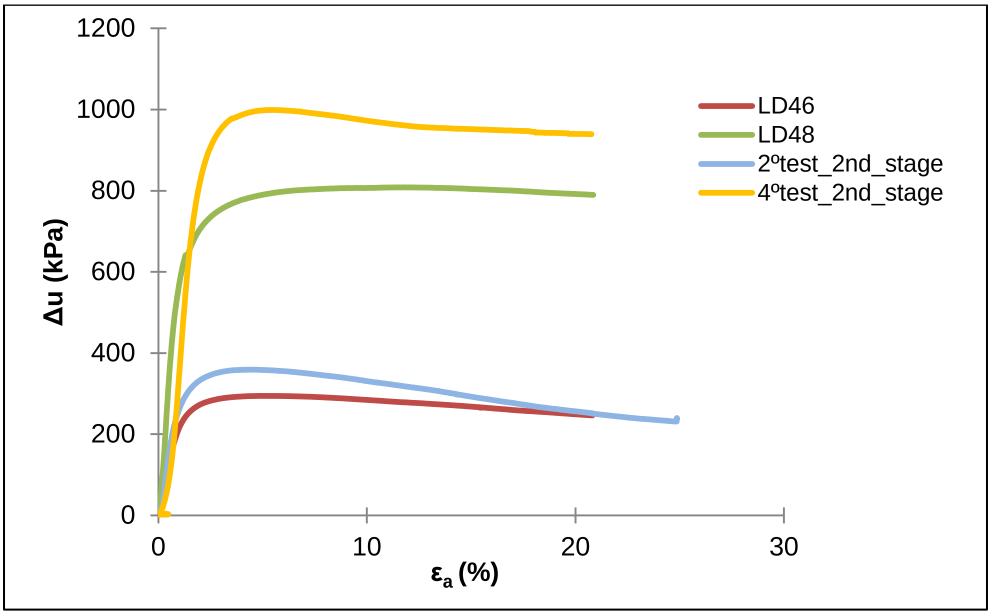

Figure 3.15 – Excess pore pressure *versus* axial strain for undrained tests with more than 400kPa of confining pressure

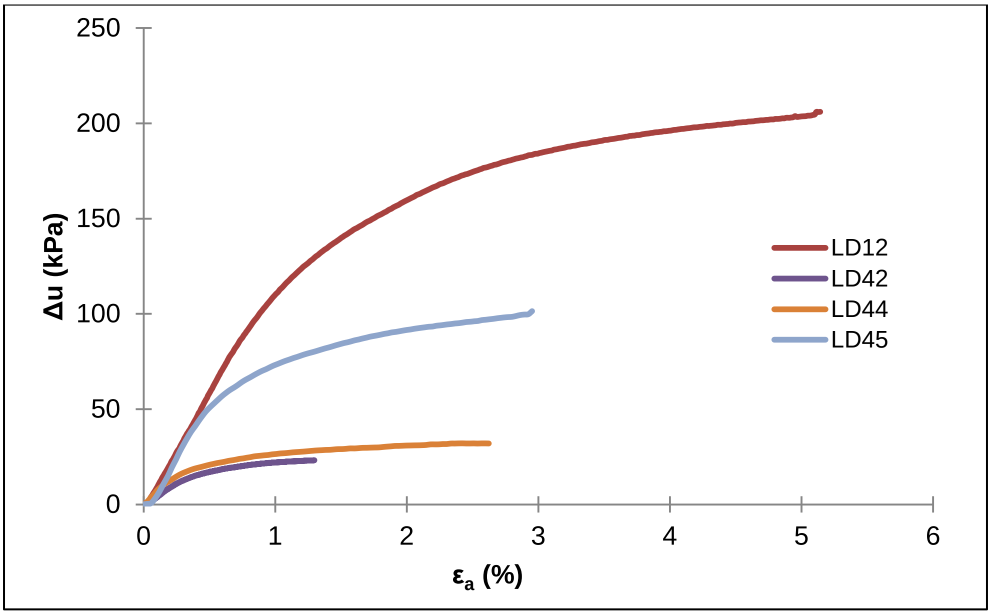

Figure 3.16 – Excess pore pressure *versus* axial strain for undrained tests with less than 200kPa of confining pressure

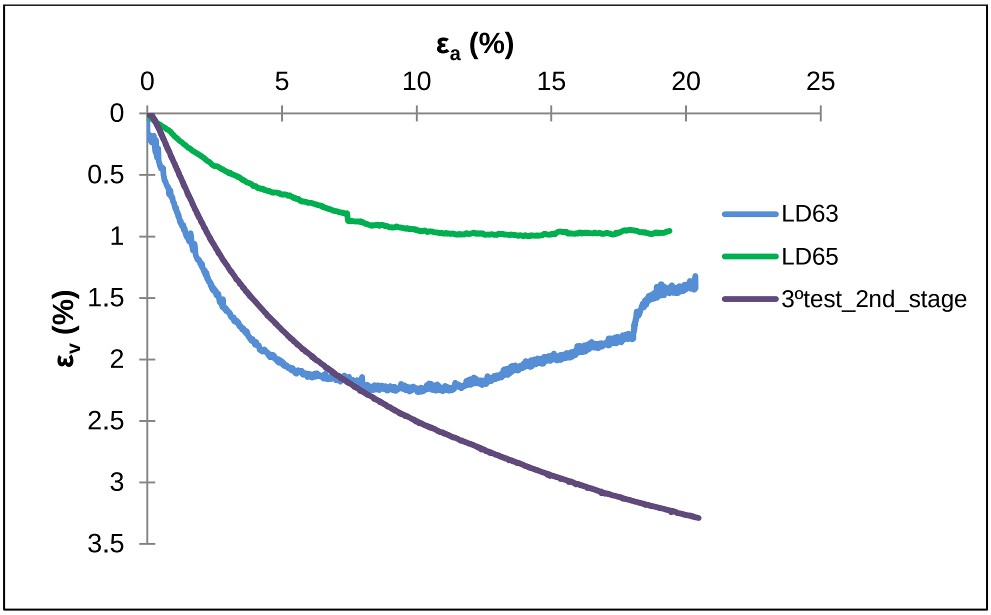

Figure 3.17 – Volumetric strain *versus* axial strain for drained tests

For lower values of confining pressure, in the undrained tests (Figure 3.13) it is evident a reduction of the deviatoric stress until zero while the excess pore pressure increases (Figure 3.16) until reaching the value of the confining pressure, lowering the shear strength of the soil and causing the occurrence of liquefaction. Observing the undrained test results for higher values of confining pressure, it is noticeable a fast increase of the excess pore pressure but then it starts decreasing. As the pore pressure diminishes the effective mean stress is never going to decrease until zero so liquefaction will not occur.

In the drained tests, the deviatoric stress quickly increases with the axial strain at first but then it becomes relatively constant. Figure 3.17 shows that the specimens contract. At the end of the test LD63, the specimen dilates a little but this is probably due to the fact that in this part of the laboratory test the variable control was not so accurate. In Figure 3.14, LD64 starts increasing the deviatoric stress with axial strain but when the test changes from drained to undrained it suffers softening and the deviatoric stress decreases.

The 2º_2nd stage and the 3º_2nd stage tests were not used in the work developed in this thesis because the first suffered a lot of hardening and did not reach the Critical State Line and the second suffered grain crushing.

4

REPRODUCTION OF THE TRIAXIAL TESTS WITH THE MODEL

4.1. INTRODUCTION

In this chapter, the results of both drained and undrained triaxial tests performed in the laboratory were compared with the numerical solution.

The numerical solution is obtained using a finite element program, *Code_Bright* which uses *GiD* system for pre-processing and post-processing. The parameters that define the sand are obtained from laboratory data or through calibration. The input of the tests in *Code_Bright* is also briefly explained. CASM is implemented in the program so the comparison between the experimental results and the numerical solution allows the verification and validation of the model.

4.1.1. CODE_BRIGHT

Code_Bright is the code used to obtain the numerical solutions of the tests in this thesis. It was developed by the Department of Geotechnical Engineering and Geosciences of the *Universitat Politècnica de Catalunya* and it consists on a finite element program that analyses thermo-hydro-mechanical problems. It is written in FORTRAN and it does not use external libraries therefore the user has to introduce most of the *input*s. The version used in this thesis was version 4, which is available for free at http://www.etcg.upc.edu/recerca/webs/code_bright/downloads.

The problem is solved considering as variables (unknowns): solid displacements (u, on three special directions), liquid pressure (P_l), gas pressure (P_g) and temperature (T). Stresses and strains are related by the mechanical constitutive model together with the equation of stress equilibrium. The strains are described in terms of displacements. The deformations are controlled by small strains and small strain rates.

There are four main groups of equations that govern this problem: balance equations, constitutive equations, equilibrium relationships and constraints definition. The constitutive equations relate the independent variables (or unknowns) and the dependent variables. The governing equations are written in terms of the unknowns when the constitutive equations are replaced in the balance equations (*Code_Bright* User’s Guide, 2012).

4.1.2. GID

GiD is a program developed by the International Center for Numerical Methods in Engineering (CIMNE) at the *Universitat Politècnica de Catalunya*. It is a universal pre and postprocessor for numerical simulations in engineering which is developed to work with different codes, such as *RamSeries*, *Tdyn*, *Vulcan* or *Code_Bright*. The author of this thesis obtained a license to work with the program, in the version 11.0.4.

For the definition of the geometry, the program works in a similar way to *CAD* (*Computer Aided Design*) system. The main difference is that the geometry is created in a hierarchical mode, which means that the higher level entities are constructed over entities of lower level. In Figure 4.1 the principal steps necessary to solve a problem with *GiD* are exposed.

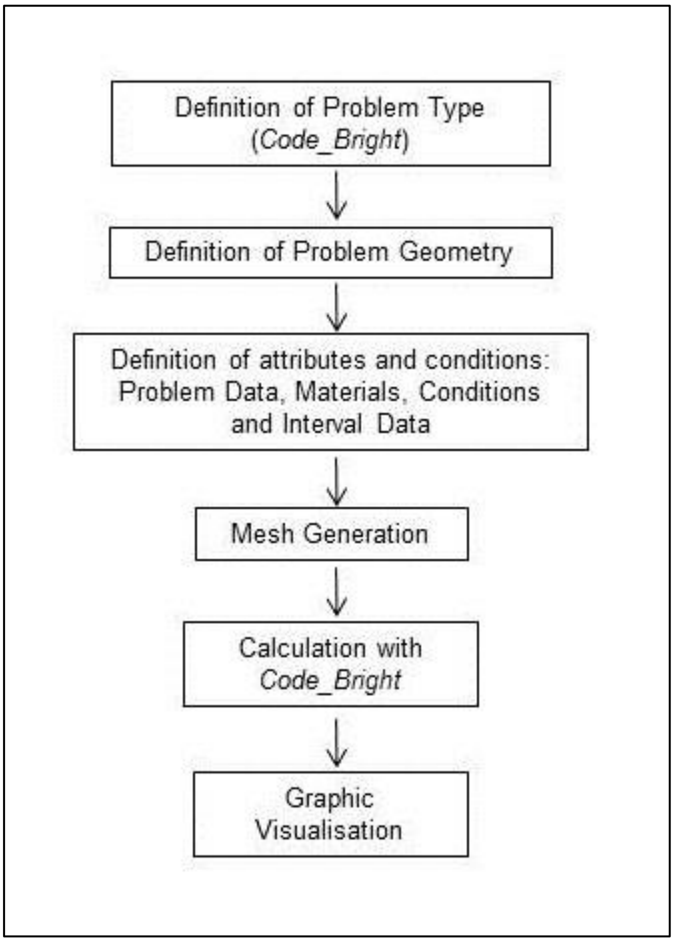

Figure 4.1– Main steps to solve a problem with *GiD*

The graphic visualization is flexible so that the user can analyse and interpret the results without difficulty. There are many options to display the results such as contour maps at each step of the calculation process, time evolution of variables graphs or graphs with the evolution of one variable as a function of other and vector distribution.

4.2. MODEL PARAMETERS

CASM requires the definition of six parameters (material constants) in order to correctly reproduce the results for a specific material. These parameters describe the elastic behaviour, the yield surface shape and the critical state. Table 4.1 summarizes the constitutive model parameters required and Table 4.2 lists the initial state values and history variables of the soil.

Table 4.1 – Description of constitutive model parameters

Group	Symbol	Description
Elastic components	ν	Poisson's ratio
	κ	Slope of the isotropic swelling line (in υ-lnp' space)
Yield surface Shape	r	Spacing ratio
	n	Shape parameter
Critical State Constants	M	Slope of the Critical State line (in q-p' space)
	λ	Slope of Critical State Line (in υ-lnp' space)

Table 4.2 – Description of initial state values and history variables

Group	Symbol	Description
Initial state values	e_0	Initial void ratio
	OCR	Overconsolidation ratio
	K_0	Coefficient of earth pressure at rest
History variables	p'_0	Preconsolidation pressure
	F	Current value of the yield function

The results of the laboratory tests performed allow the definition of most CASM parameters (ν, κ, M, λ, e_0, OCR, K_0 and p'_0). The experimental data is simulated using mathematical models. Other parameters are obtained through calibration (such as n, r and F) of the tests and the model. In this section, these parameters are defined.

4.2.1. ELASTIC PARAMETERS

- Poisson's ratio, ν

According to Yu (1998), the Poisson's ratio is typically in the range of 0.15-0.35 for clays and sand. For this particular sand, the Poisson's ratio was determined by Fonseca (2009) using the expression in equation (4.1) where V_P and V_S are the P and S wave velocities respectively. Its value is 0.362.

$$\nu = \frac{\left(\frac{V_P}{V_S}\right)^2 - 2}{2\left(\frac{V_P}{V_S}\right)^2 - 2} \tag{4.1}$$

- Slope of the isotropic swelling line (in υ-lnp' space), κ

The value of κ is highly variable and depends on the effect of loading and unloading in soil grains (Atkinson, 1993). The swelling line is defined by the path of the unloading-reloading during isotropic compression and swelling. This parameter was obtained from an oedometer test performed in *Les Dunes* sand in a sample with 50 mm of diameter As shown in Figure 4.2, the slope of the isotropic swelling line plotted in υ-lnp' space, κ is 0.005. According to Yu (1998) this is a typical value for sands.

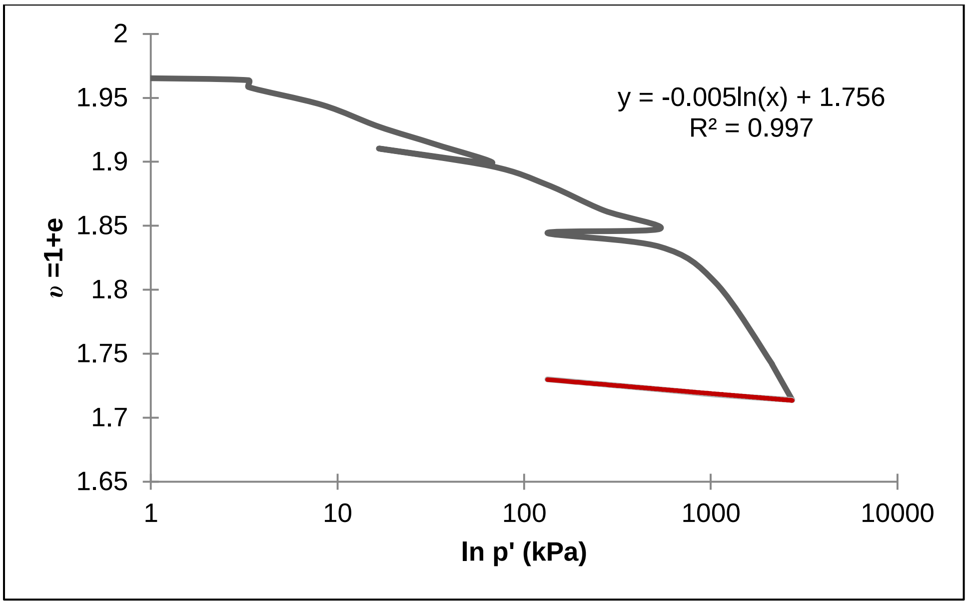

Figure 4.2 – Oedometer test results (50 mm diameter) for determination of κ

4.2.2. CRITICAL STATE CONSTANTS

- Slope of the Critical State line in q-p' space, M

The slope of the critical state line, also known as critical stress ratio, was calculated using equation (4.2) and the friction angle at the critical state obtained in previous studies (Section 3.2), the parameter M is determined to be 1.3047. Typical values for sands lie between 1.1 and 1.4 (Yu, 1998).

$$M_c = \frac{6\sin 32.4°}{3 - \sin 32.4°} = 1.3047 \qquad (4.2)$$

- Slope of the Critical State Line (in υ-lnp' space), λ

The critical state line for sands is difficult to determine clearly. However, using the results of some drained and undrained triaxial tests performed in *Les Dunes* sand, by Fonseca (2009), Rocha (2010) and along the experimental program of Soares (reported in Viana da Fonseca and Soares, 2012) it was possible to draw it. The parameter λ is the slope of the critical state line in υ-lnp' space and, as it is seen in Figure 4.3, has the value of 0.021.

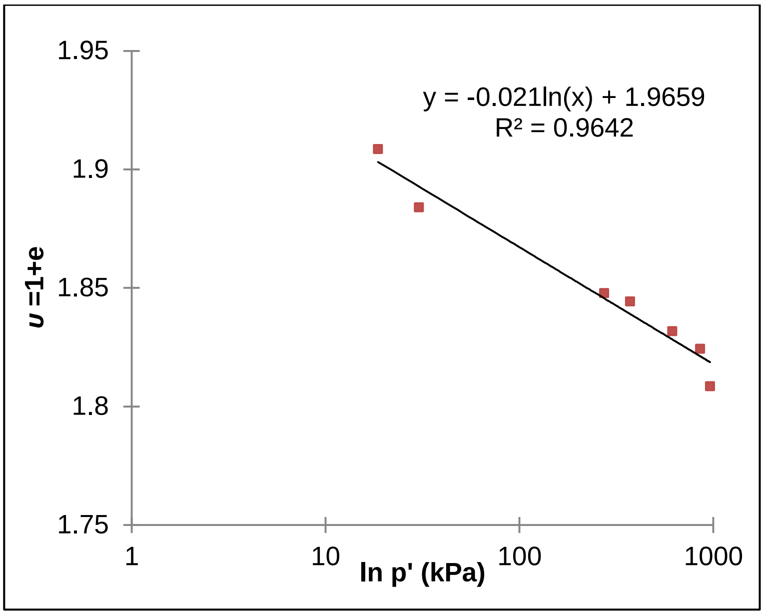

Figure 4.3 – Critical State Line in υ-ln p' space (Viana da Fonseca and Soares, 2012)

In order to validate this value, the results of two oedometer tests were used. One test was performed in a sample with 50 mm of diameter and other in a sample with a diameter of 75 mm. The slopes of the Normal Compression Lines were determined to be 0.022 and 0.023, respectively, as shown in Figure 4.4. The line was identified before the grain crushing. The zone after the NCL corresponds to the evolutive behaviour after particle breakage. Knowing that the Critical State Line is admitted to be parallel to the Normal Compression Line, it can be said that the slope of the CSL was well determined and the value of λ=0.021 is acceptable.

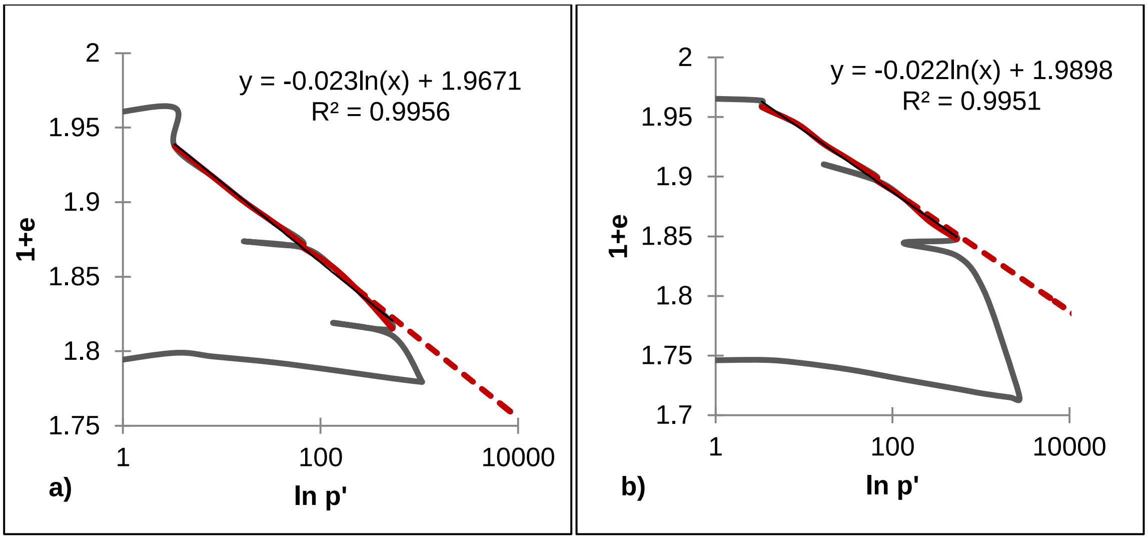

Figure 4.4 – Oedometer test results for determination of λ; a) 50mm; b) 75mm

4.2.3. YIELD SURFACE SHAPE PARAMETERS

The *r* and *n* parameters are specific for the model. Therefore, they cannot be determined directly from laboratory data and have to be calibrated using test results. In Figure 4.5, the effects of changing the value of *n* are shown. When *n*=1.5, the yield surface is symmetrical, when its value increases the maximum deviatoric stress tends to move right and when its value decreases that peak moves left. Figure 4.6 illustrates how the yield function changes according to the value of *r*. As the value of *r* increases, the peak of the yield surface decreases.

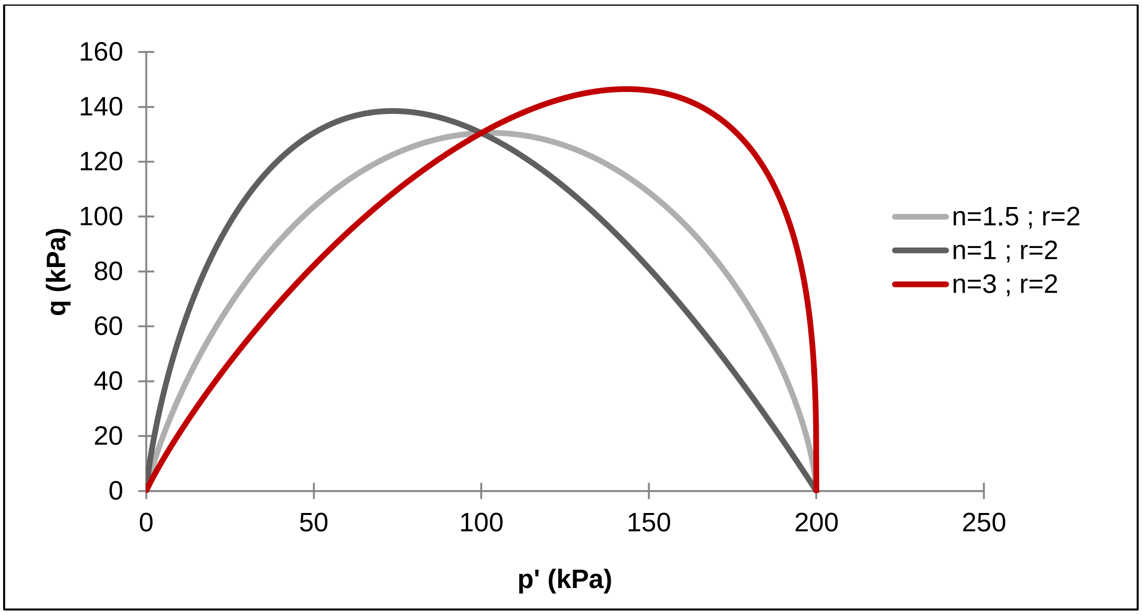

Figure 4.5 – Evolution of the shape parameter *n*

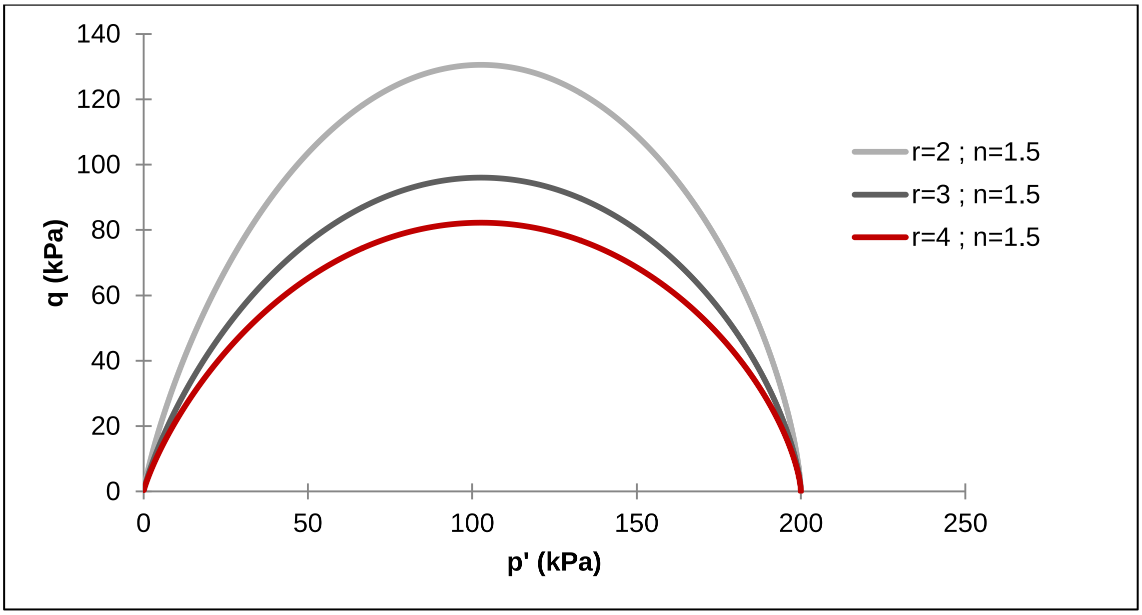

Figure 4.6 – Evolution of the spacing ratio *r*

The calibration is based on the plot of the yield surface and the results of undrained triaxial tests. For each test, the values of e_0 and p'_0 are different but the yield surface parameters should be the same. The values of p'_0 for each undrained triaxial test are listed in Table 4.3 and they are obtained from the experimental results. The equation (4.3) was used to define the yield surface of the CASM model and it was obtained by equating the yield function to zero.

$$F = 0 \Rightarrow q = Mp'\left(ln\left(\frac{p'_0}{p'}\right)\frac{1}{ln\, r}\right)^{\frac{1}{n}} \tag{4.3}$$

Table 4.3 - Values of p'_0 for undrained triaxial tests

Designation Triaxial Test	p'_0 (kPa)
LD12	200
LD42	23
LD44	30
LD45	100
LD46	400
LD48	1000
4º_2nd stage	1500

After trying several possibilities, the best values of n and r found were 3 and 15 respectively. The results are shown in Figure 4.7, where it is seen the similarity between the yield surfaces computed using the yield function from CASM (red) and the laboratory test results (grey). The 4º_2nd stage test was not used on the following analysis because as it can be seen in **Error! Reference source not ound.** g), its stress-path was peculiar and the values of p' increase at the beginning of the test. Since this test was performed with a high confining pressure (1500kPa), the material is already behaving with a higher compressibility (the CSL steepens its slope) due to the increase in fines resulting from grain crushing. Therefore, as its behaviour is not the same as the other tests, it was decided not to use it in the present work.

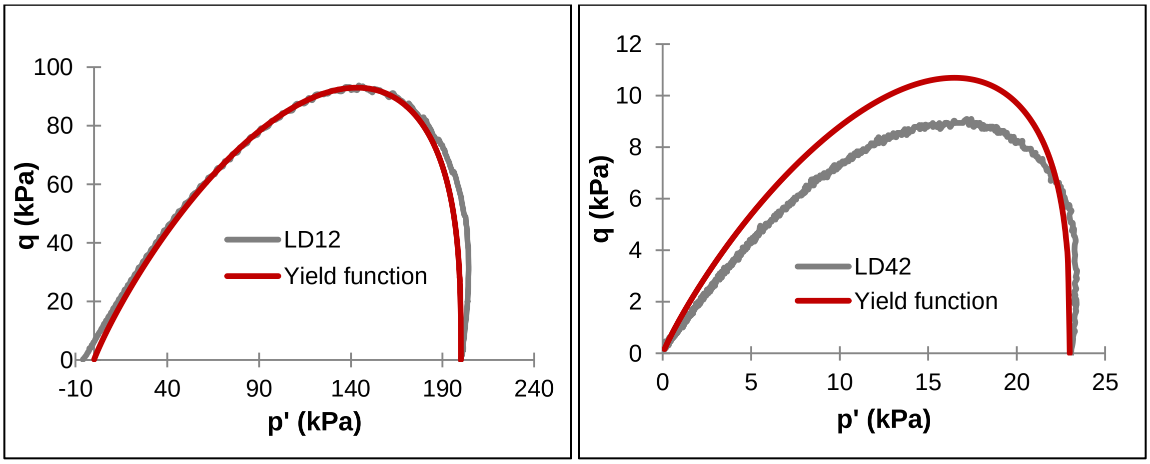

a)

b)

Figure 4.7 – Yield surfaces for undrained triaxial tests: a) LD12; b) LD42 (to be continued)

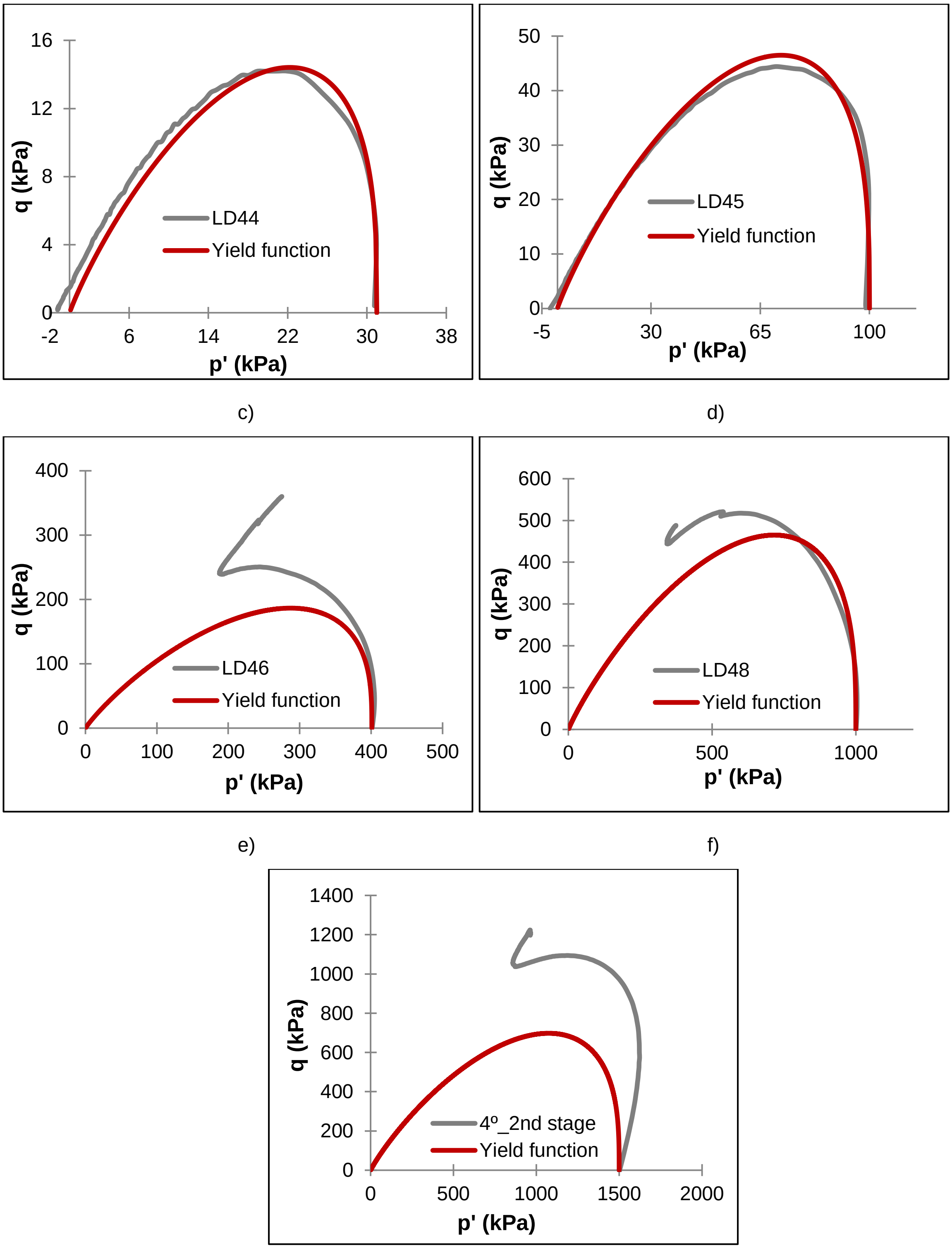

c)

d)

e)

f)

g)

Figure 4.7 – Yield surfaces for undrained triaxial tests (cont.): c) LD44; d) LD45; e) LD46; f) LD48; g) 4º_2nd stage

4.3. NUMERICAL MODEL

As described before, the code used to model the tests was *Code_Bright*. The Clay and Sand Model (CASM) is implemented in the code, which allows the simulation of the triaxial test performed in the laboratory and the validation of the constitutive model parameters.

The triaxial specimens used in the laboratory are cylinders with 70 mm of diameter and 140 mm of height. As they are symmetrical around a vertical axe passing in the centre of the base of the cylinder, the simulation was performed on half of a specimen (a rectangle with 35 mm of base and 140 mm of height) and the option “Axysimetry around y-axis” was selected so, in the end, an element fixed in one of the borders allowed the free movement to the other two directions (radial and axial). The geometry domain is composed by points, lines, surfaces and volumes and all domains are considered in 3-dimensional space (assuming that there is variation in the third coordinate). The specimen geometry is represented in Figure 4.8, where the lines are drawn in blue and numbered and the surface is represented in purple.

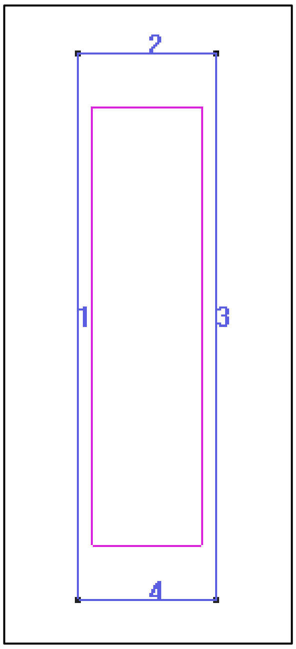

Figure 4.8 – Specimen geometry

In mechanical problems, the boundary conditions are forces and displacement rate in some spacial direction. In hydraulic problems, the mass flow rate of water has to be prescribed, as well as the liquid pressure. The boundary conditions assigned for this particular problem were “X direction is prescribed” on line 1, “Y direction is prescribed” on line 4, isotropic vertical and horizontal stresses on lines 2 and 3 respectively and incremental vertical displacement on line 2 (Figure 4.9). In the undrained tests, the water is not allowed to flow out of the specimen so it was imposed a flux boundary condition on each line with all the variables equal to zero.

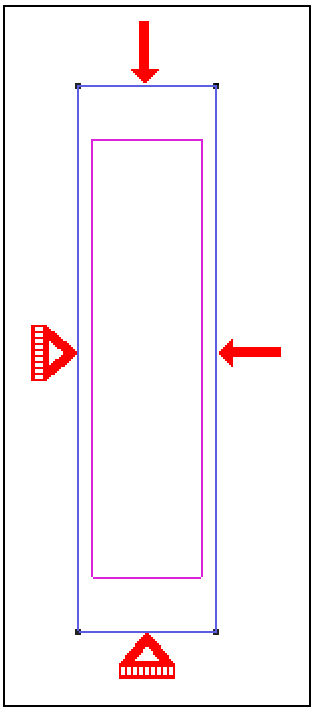

Figure 4.9 – Representation of the boundary conditions imposed

A specific value for porosity was also imposed, related to the void ratio by using equation (4.4), and the initial stress composed by the value of the isotropic stresses on the three main directions (X, Y and Z) and the preconsolidation pressure, p'_0, as Hist.1 (*Code_Bright* User's Guide, 2012). The value of the void ratio is computed internally as a function of porosity. Table 4.4 presents the values of these parameters for each triaxial test simulated.

$$n = \frac{e}{1+e} \tag{4.4}$$

Table 4.4 – Values of *n* and initial stress for each triaxial test

Designation Triaxial Test	e	*n*	X stress (kPa)	Y stress (kPa)	Z stress (kPa)
LD12	0.885	0.469	200	200	200
LD42	0.897	0.473	23	23	23
LD44	0.901	0.474	30	30	30
LD45	0.873	0.466	100	100	100
LD46	0.848	0.459	400	400	400
LD48	0.844	0.458	1000	1000	1000
LD63	0.850	0.459	500	500	500
LD64	0.859	0.462	1000	1000	1000
LD65	0.902	0.474	15	15	15
4º_2nd stage	0.808	0.447	1500	1500	1500

The material parameters are common to every specimen and test performed. As the specimens are saturated, the mechanical data was introduced in the CASM (general) option and it is exposed on Table 4.5. In the undrained tests, it is also necessary to compute the Hydraulic data. As the specimens are saturated, it is not required to input any retention curve or relative permeability parameters. However it is necessary to insert the intrinsic permeability parameters (Table 4.6). This value is not that relevant so it was adopted a value common for sands, 10^{-3} m/s (10^{-10} m^2).

Table 4.5 – Mechanical Data (parameters for CASM general)

ITYCL=1	Symbol	Units	Description	Value
P1	v	-	Poisson ratio	0.362
P2	κ	-	Slope of the isotropic swelling line (in υ-lnp' space)	5.00x10^{-3}
P3	λ	-	Slope of Critical State Line (in e-lnp' space)	0.021
P4	r	-	Spacing ratio	15
P5	n	-	Shape parameter	3
P6	M	-	Slope of the Critical State line (in q-p' space)	1.3047
P7	ϕ_{cs}	º	Friction angle at CS (computed as a function of M)	-
P8		-		-
P9		-		-
P10	S_u	MPa	Undrained shear strength (optional). By default = 0	0

Table 4.6 – Hydraulic Data (parameters for intrinsic permeability)

ITYCL=1	Symbol	Units	Description	Value
P1	$(k_{11})_0$	m^2	Intrinsic permeability, 1st principal direction	10^{-10}
P2	$(k_{22})_0$	m^2	Intrinsic permeability, 2nd principal direction	10^{-10}
P3	$(k_{33})_0$	m^2	Intrinsic permeability, 3rd principal direction	10^{-10}
P4	ϕ_0	-	Reference porosity for read intrinsic permeability. If ϕ_0=0, permeability will be constant	0
P5	ϕ_{min}	-	Minimum porosity	0

It is also important to define the “Interval Data”. This option allows changing some conditions or material properties at each interval of time. In this option it is possible to discretize the units of time used, the initial (start) and final (end) times of the process and the time steps.

In order to simulate the triaxial tests performed in the laboratory, it was defined only one interval since the boundary conditions and material parameters do not change during the test. This time is different for each test. In the drained tests, a time was inputted so that in the end the stress-strain curve became horizontal and the stress becomes constant. In the undrained tests, the calculation process stoped before the end of the time established in the interval data because the stress-path reach instability, as it is going to be shown in the next sections, and the program cannot compute the results after this point.

When the problem is fully defined, the meshing is implemented. It consists in discretizing the geometry into nodes and elements. The mesh is constituted by 196 quadrilateral elements and 232 nodes. The quadrilateral elements are the best option, especially in the undrained test simulations because as there is no volumetric changes, the nodes can readjust better (in order to maintain the volume of the specimen, while changing the position of the nodes) than if they were triangles. In Figure 4.10, the mesh is represented.

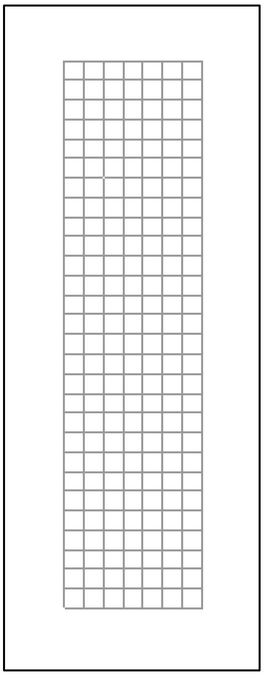

Figure 4.10 – Representation of the mesh

4.4. APPLICABILITY OF THE MODEL

With the results of both drained and undrained triaxial tests it was possible to evaluate the parameters previously defined and the performance of CASM implemented in *Code_Bright*. Each test was simulated, according to what was described before and compared with the results of the experimental data.

The two drained tests performed were LD63 and LD65. The parameters used in the model are the same as the ones presented in Table 4.5 and Table 4.7.

Table 4.7 – Value of e_0 and p'_0 for drained triaxial tests

Designation Triaxial Test	e_0	p'_0 (kPa)
LD63	0.850	500
LD65	0.902	15

As it is presented in Figure 4.11, the stress-strain-volumetric paths of LD63 test are well adjusted to the model. The critical state is reached with an axial strain of about 15-20% and as it is expected there is contraction of the specimen. In Figure 4.12, the LD65 test results are represented. The model does not adjust as well to the experimental data, especially the strain-volumetric curve. This means that the model cannot reproduce all the real features of the material response during a triaxial test either, because the underlying mechanisms are more complex or because heterogeneities in the test sample and/or experimental difficulties.

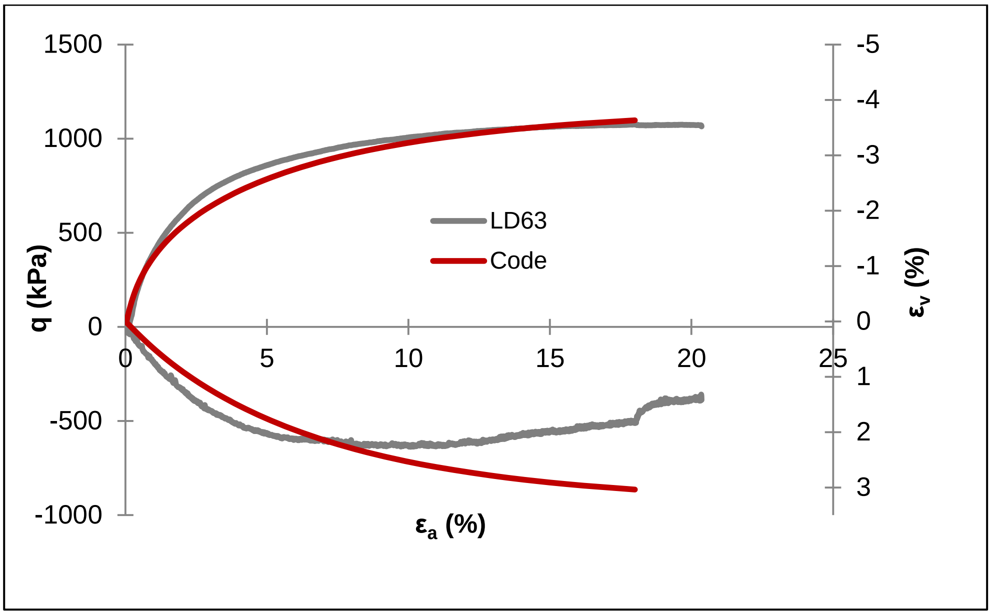

Figure 4.11 – Stress-strain-volumetric curves for drained triaxial test LD63

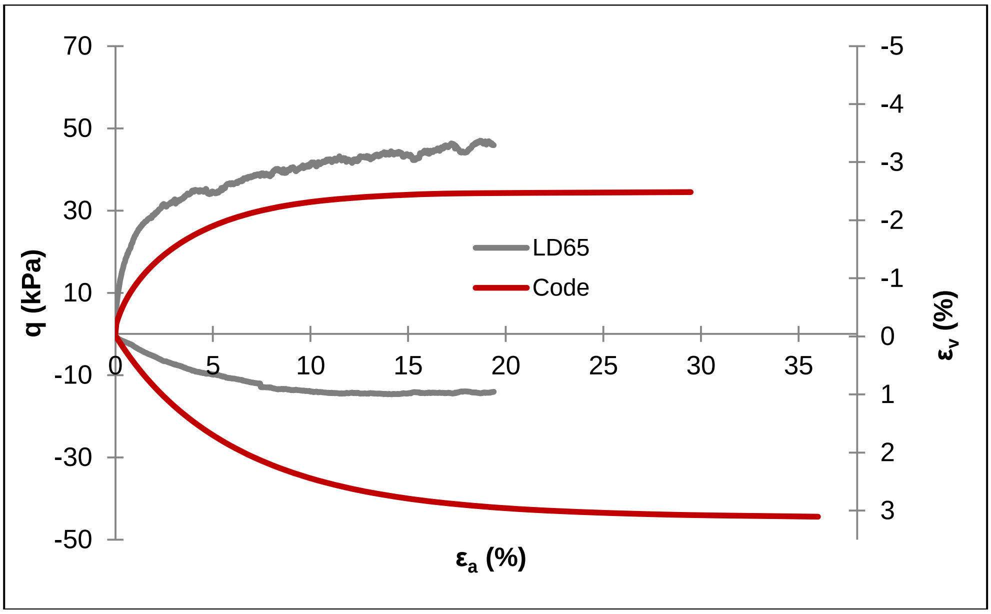

Figure 4.12 – Stress-strain-volumetric curves for drained triaxial test LD65

Regarding the six undrained tests performed, the parameters used in the model are the same as the ones presented in Table 4.5 and Table 4.6 and the values of p'_0 and e_0 for each test are shown in Table 4.3 and Table 4.4 respectively. Figure 4.13 to 4.18 show the stress-path and the stress-strain curves for each test.

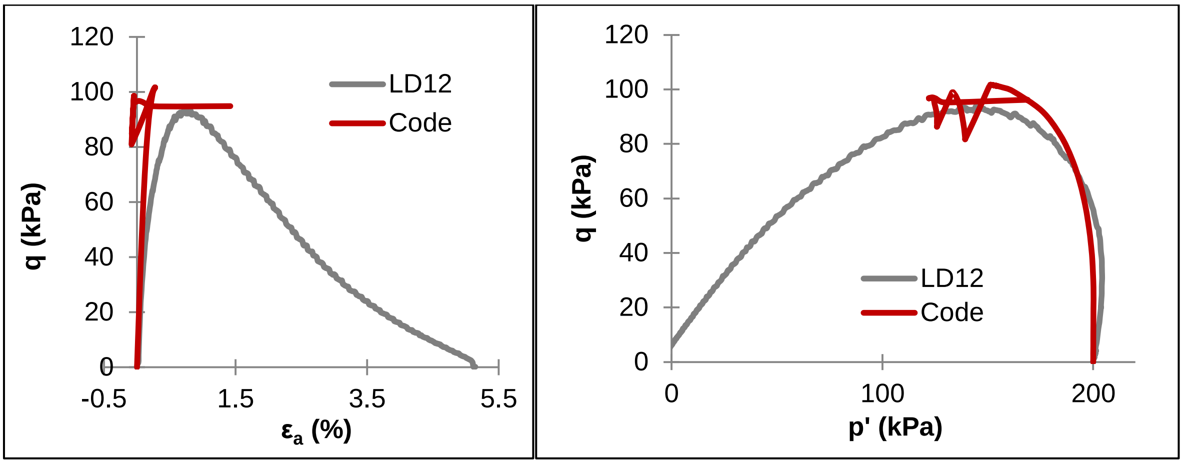

Figure 4.13 – LD12: Stress-strain curve and Stress-path

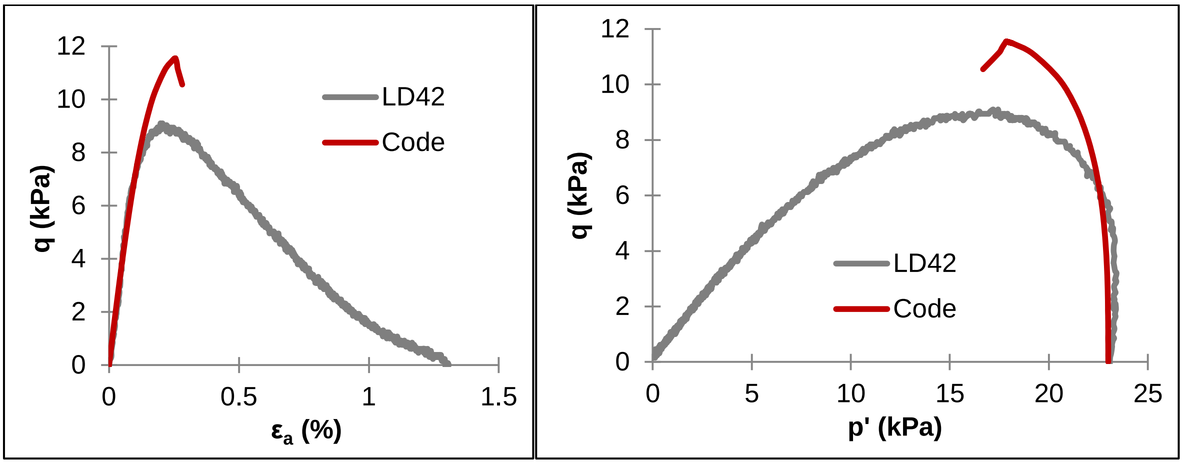

Figure 4.14 – LD42: Stress-strain curve and Stress-path

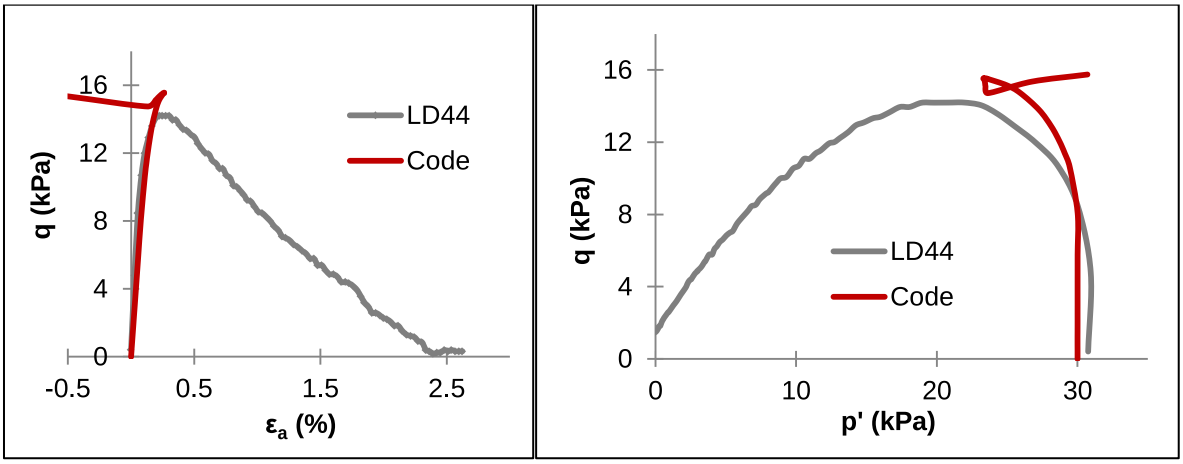

Figure 4.15 – LD44: Stress-strain curve and Stress-path

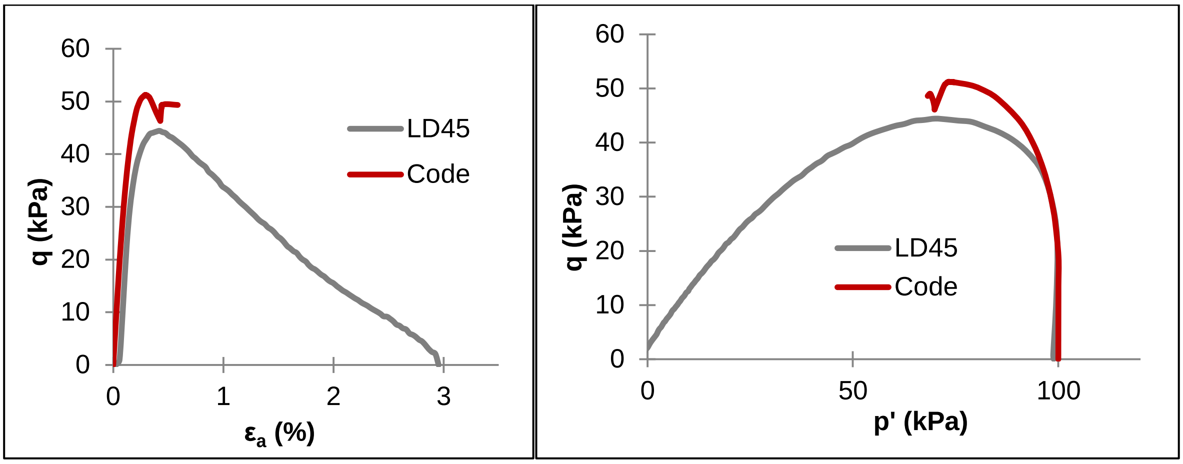

Figure 4.16 – LD45: Stress-strain curve and Stress-path

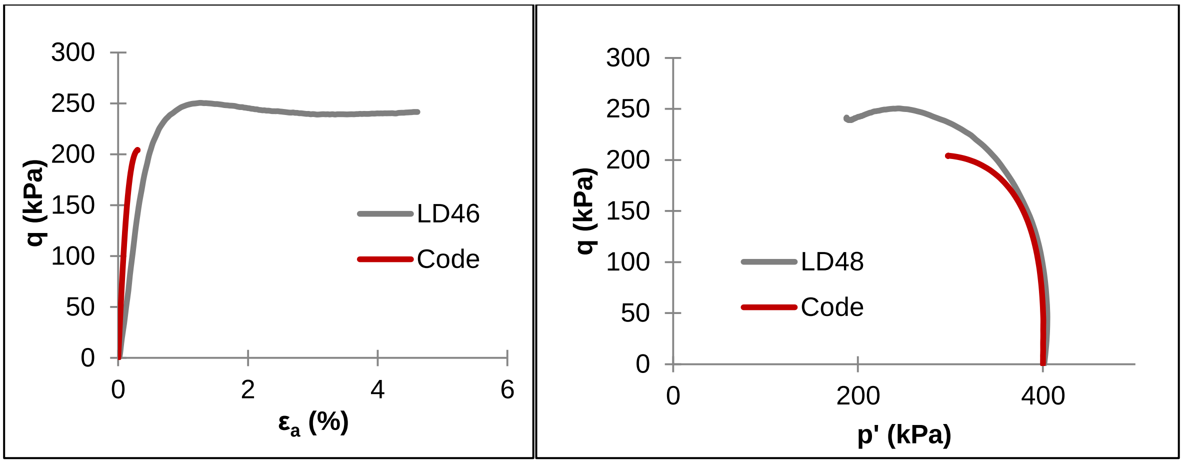

Figure 4.17 – LD46: Stress-strain curve and Stress-path

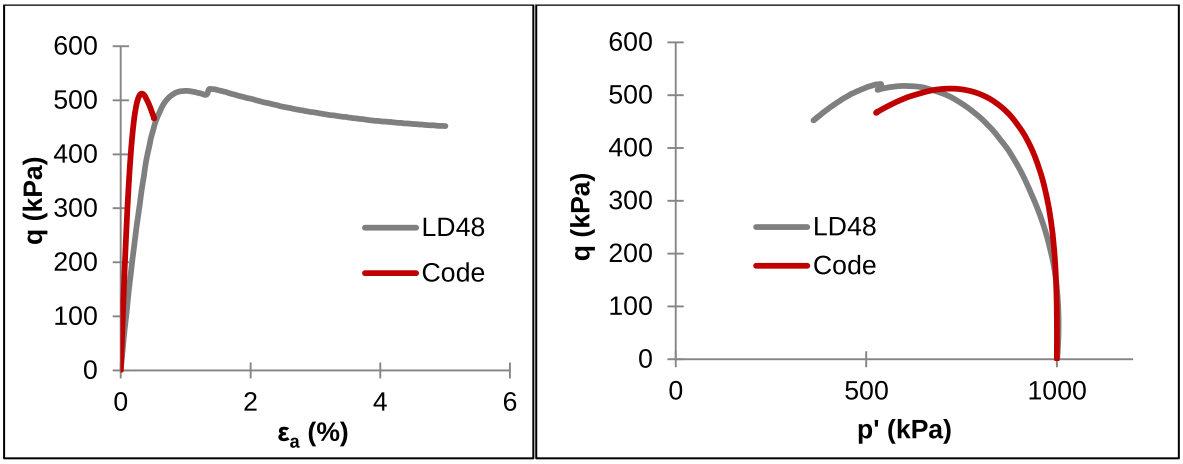

Figure 4.18 – LD48: Stress-strain curve and Stress-path

Analysing the stress-paths and the stress-strain curves presented in the Figures above, it is clearly expressed that the results obtained with the model adjust rather well the laboratory test results so it can be said that the CASM model is adequate to simulate the behaviour of *Les Dunes* sand until the instability point.

With the first initial time step imposed on the Interval Data menu (1e-5), *Code_Bright* was not able to reproduce results after the instability point, i.e., the peak of the deviatoric stress, q. This is shown in the Figures above, where it is notable that the model follows the stress path of the laboratory tests but, when the peak is reached, the path follows erratic directions. This is due to numerical instability during the reproduction of the physical instability. Since this does not really happen, some regularization technics need to be implemented in *Code_Bright*.

However, when the initial time step was increased to 0.1, *Code_Bright* was able to compute results after passing the instability point, as shown in Figure 4.19 to Figure 4.24. This is justified by the fact that with a higher initial time step, the number of points calculated is smaller and probably the stress-path avoids matching the instability point (this point may be between two time steps) and so it continues to give results after that point.

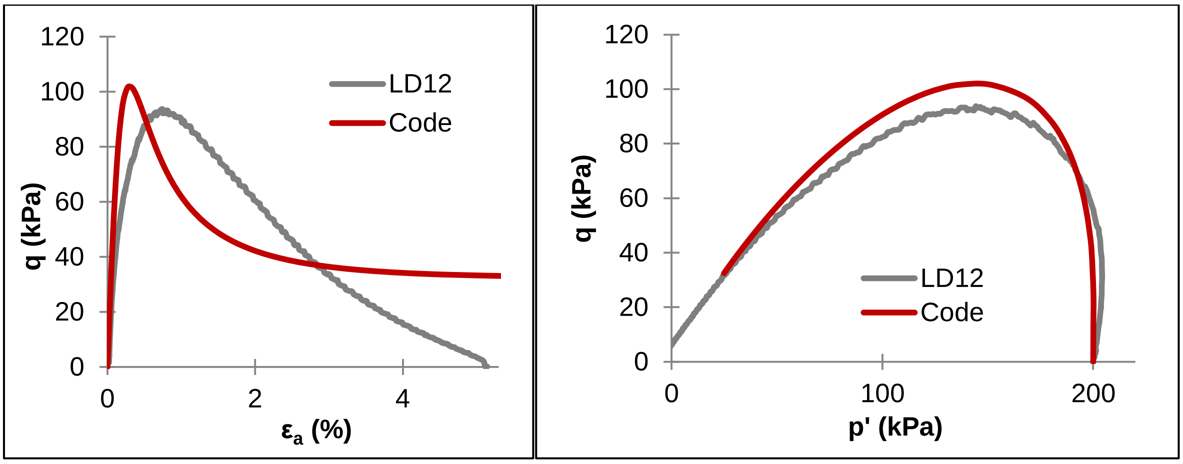

Figure 4.19 – LD12: Stress-strain curve and Stress-path

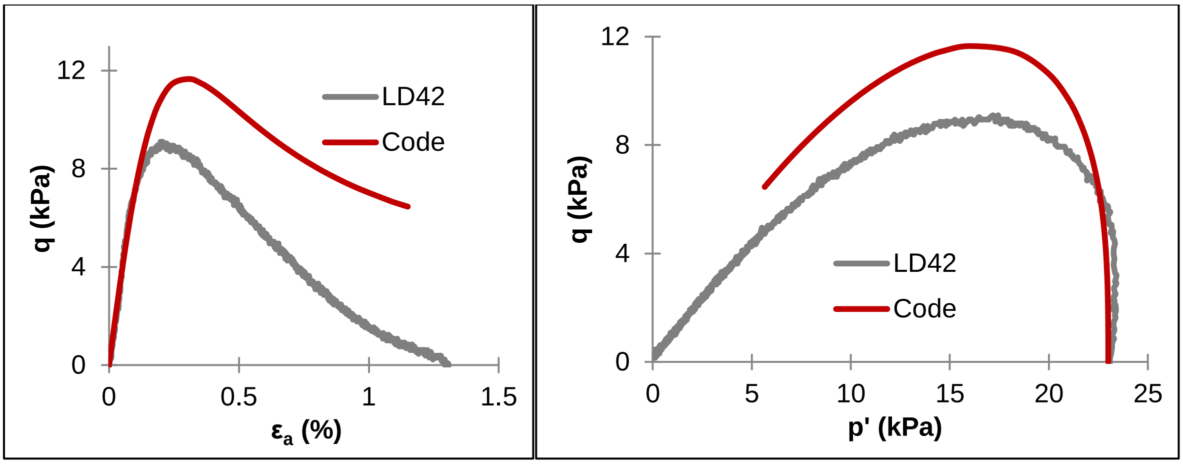

Figure 4.20 – LD42: Stress-strain curve and Stress-path

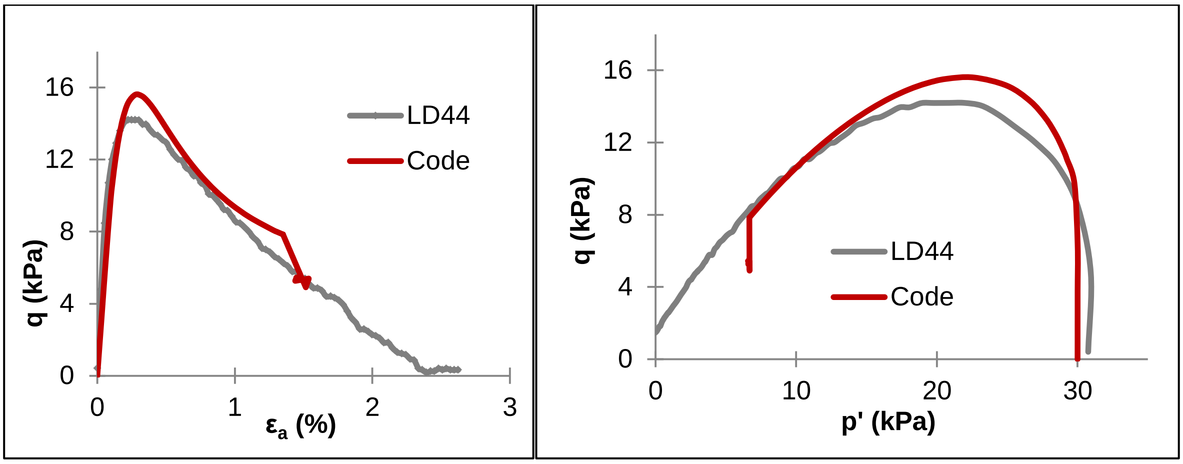

Figure 4.21 – LD44: Stress-strain curve and Stress-path

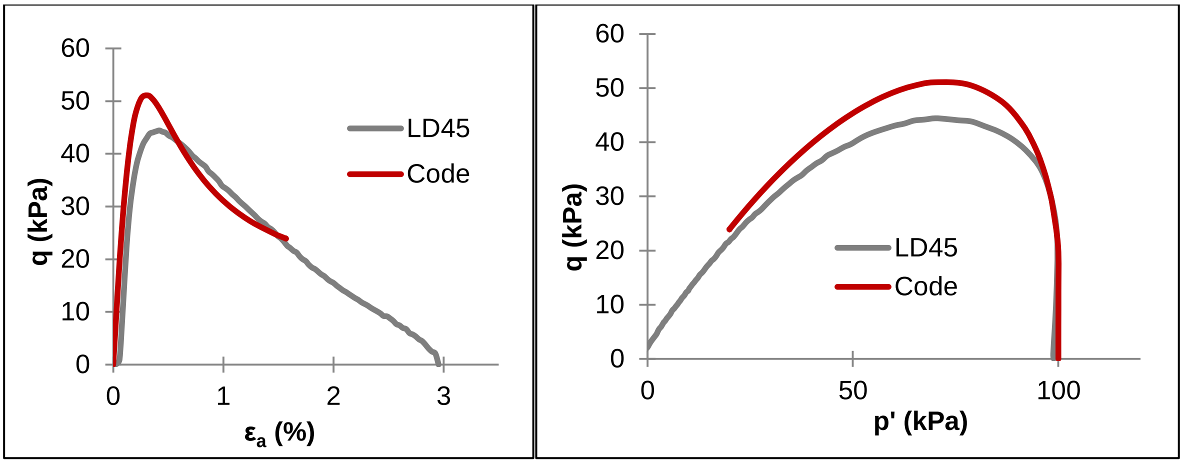

Figure 4.22 – LD45: Stress-strain curve and Stress-path

Figure 4.23 and Figure 4.24 present two undrained tests where the results from the Code show that the stress-path decreases after the peak of deviatoric stress, but the samples experiment dilatancy afterwards, that is, an increase in deviatoric stress. This experimental change in behaviour is called phase transformation and occurs when the stress point is above a given threshold in the p'-q plane. This important issue has not been tackled in the present work and would require a modification in the flow rule of CASM model.

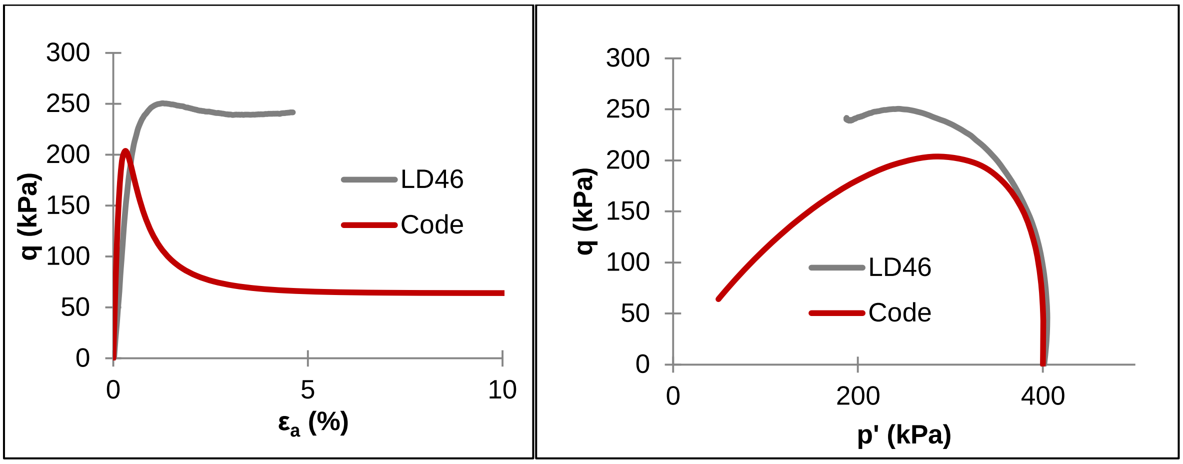

Figure 4.23 – LD46: Stress-strain curve and Stress-path

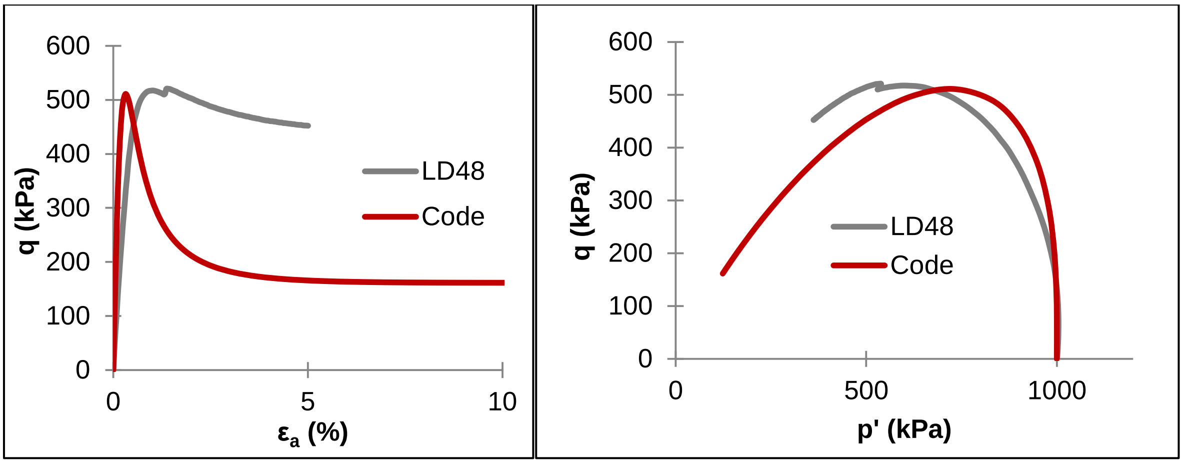

Figure 4.24 – LD48: Stress-strain curve and Stress-path

Observing the tests that suffered liquefaction (LD12, LD42, LD44 and LD45), it should be noted that the peak of the deviatoric stress is a little higher in the results obtained from *Code_Bright* than in the experimental results. Therefore, the instability line concept that will be studied in a different approach in the next Chapter, although it does not preclude the use of the results given by *Code_Bright*.

Figure 4.25 shows the pore pressure *versus* the axial strain curves for all the six previous tests. It is noticeable that the pore pressure increases fast in the beginning but then it stabilizes. The Code results are very similar to the laboratory results, evidencing once more of how well the CASM implemented in *Code_Bright* can simulate the behaviour of *Les Dunes* sand until the instability point.

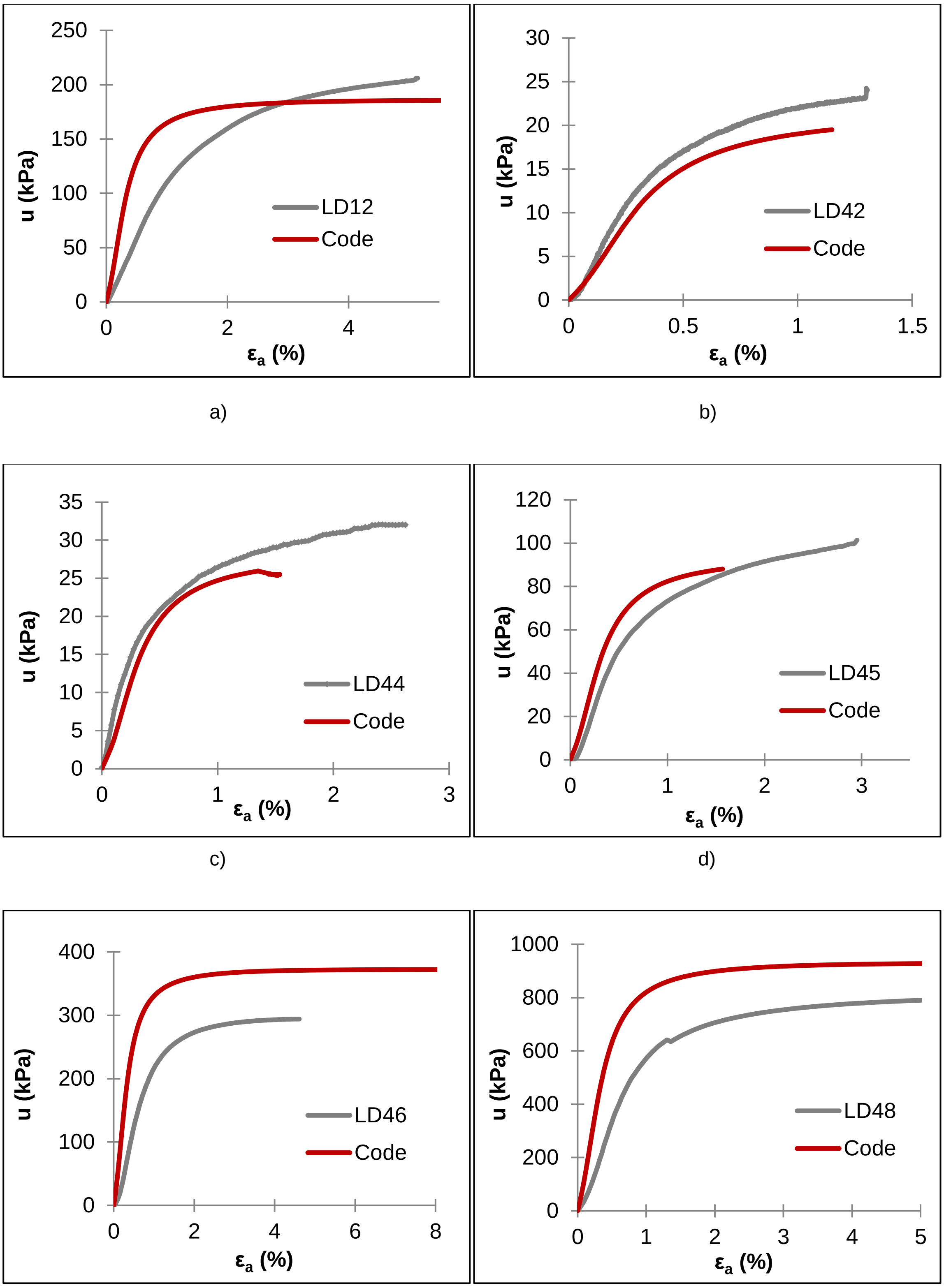

a) b)

c) d)

e) f)

Figure 4.25 – Pore pressure *versus* axial strain: a) LD12; b) LD42; c) LD44; d) LD45; e) LD46; f) LD48

Figures 4.26, 4.27 and 4.28 represent,respectively, the deviatoric stress versus the axial straincurves, the pore pressure versus the axial strain curves and the stress-paths for all the undrained tests performed in the laboratory and their simulation with *Code_Bright*.

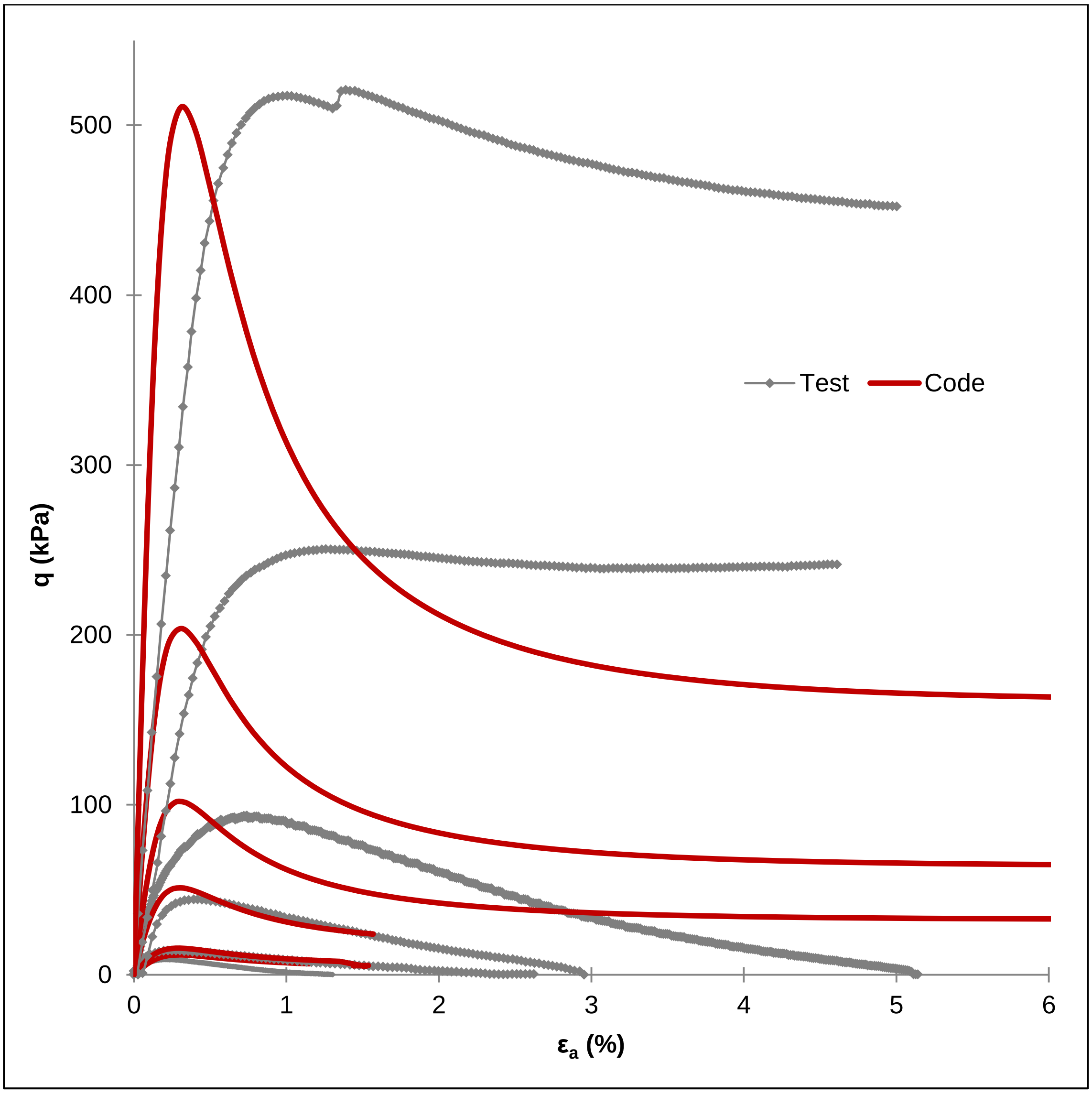

Figure 4.26 – Deviatoric stress *versus* axial strain for undrained tests

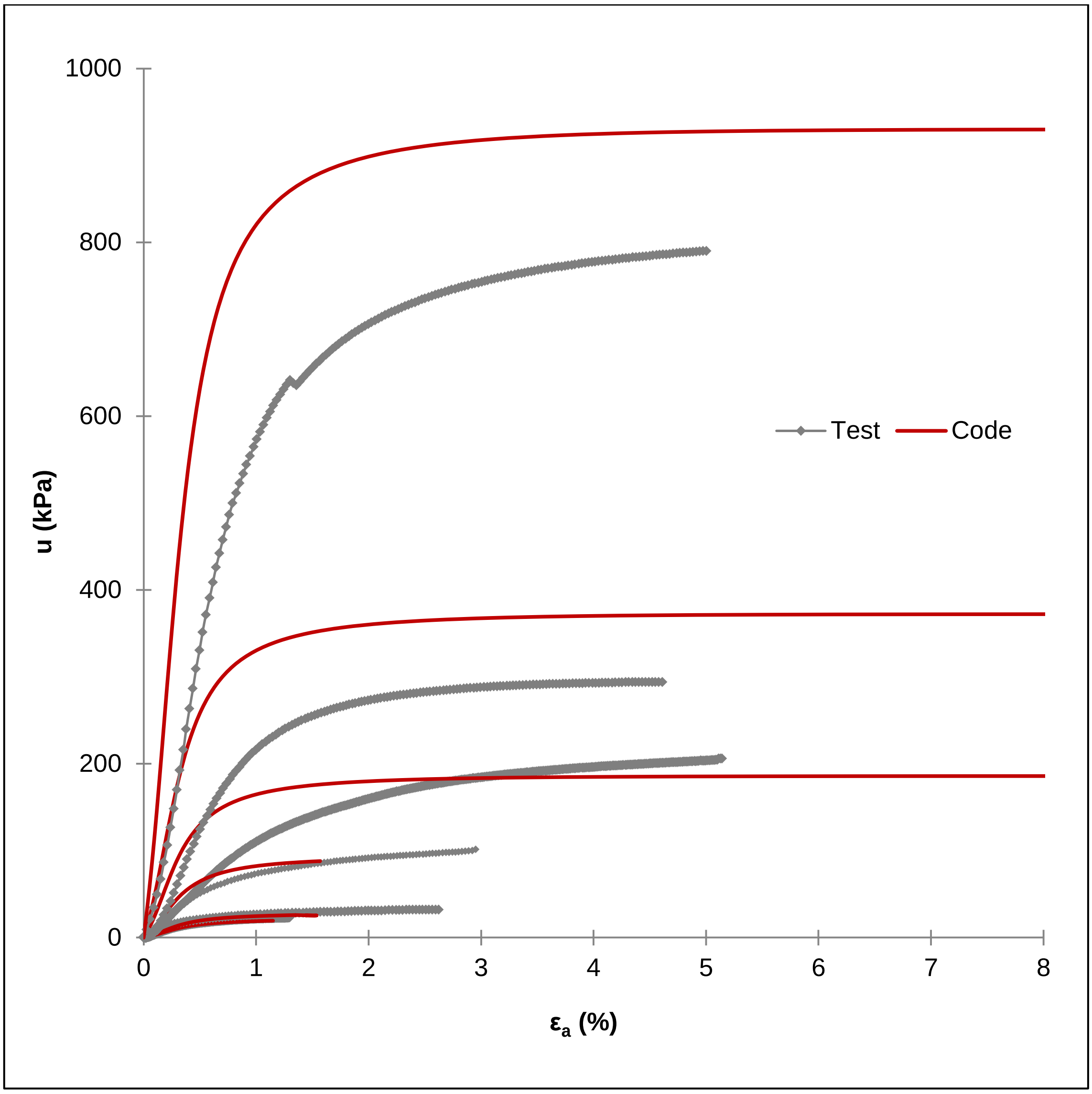

Figure 4.27 – Pore pressure *versus* axial strain for undrained tests

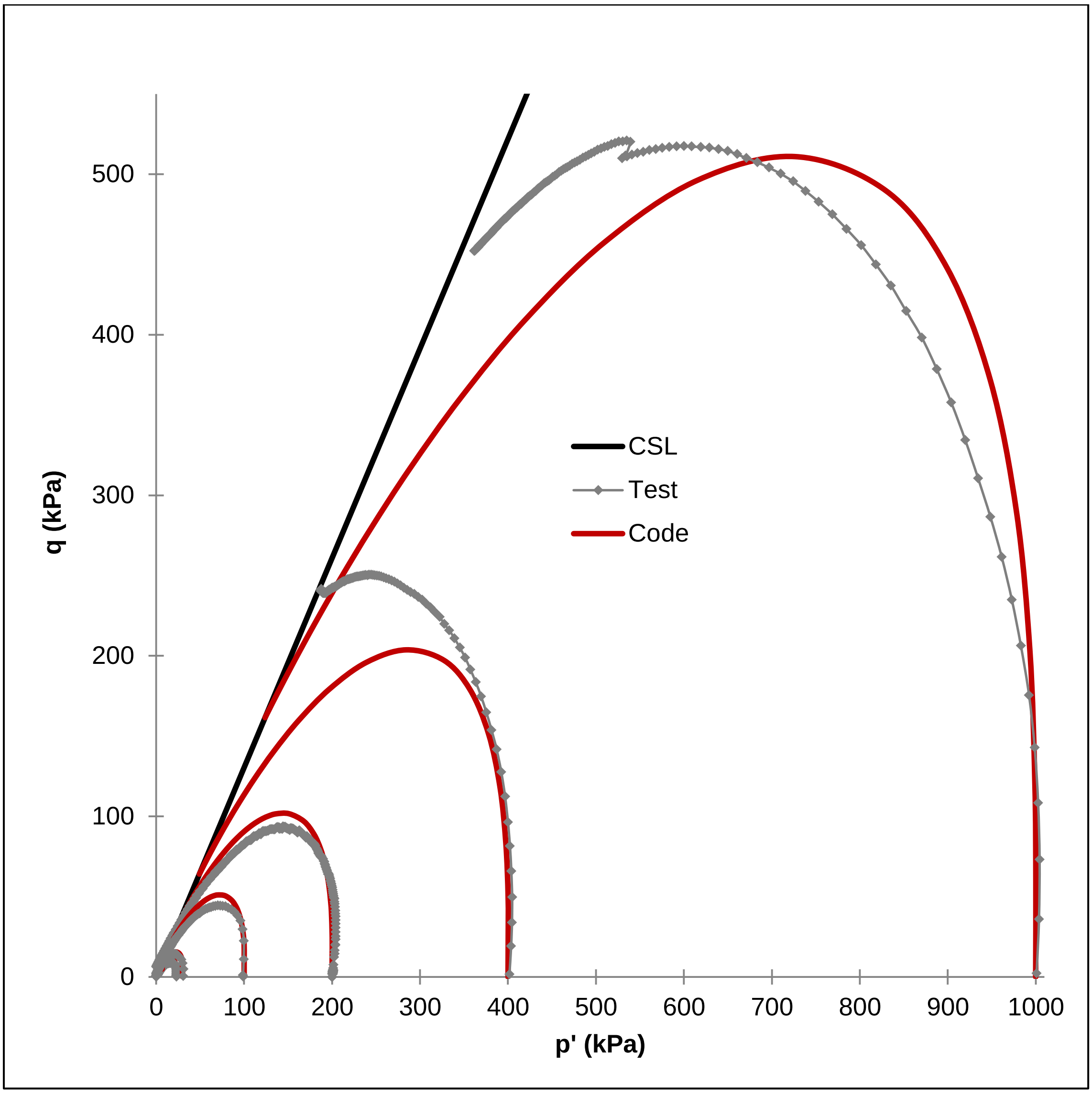

Figure 4.28 – Stress-path for undrained tests

5

STUDY OF INSTABILITY IN LES DUNES SAND

5.1. BACKGROUND ON INSTABILITY OF SANDS

5.1.1. PLASTIC WORK

There are two types of work, based on the stresses and the plastic strain increment. The plastic work (first order work increment) is defined by equation (5.1). It defines the condition of irreversibility that requires that this plastic work is positive whenever a change in plastic strain occurs (Kim and Lade, 1988).

$$dW_P = \sigma_{ij} \cdot d\varepsilon_{ij}^{p} = p' \cdot d\varepsilon_v + q \cdot d\varepsilon_s \tag{5.1}$$

The second-order work increment is the one used to study the instability in the present work and will be explained further.

5.1.2. STABILITY POSTULATES

Drucker (1959) and Hill (1958) proposed some stability postulates that provide conditions that are sufficient to ensure stability and guarantee uniqueness in both dynamic and static problems. The stability postulate proposed by Drucker for solid metals demands an associated plastic flow, where the plastic potential surface coincides with the yield surface. This postulate requires that the second increment of plastic work is greater than or equal to zero, which is represented in equation (5.2), where $d\sigma_{ij}$ is the increment of stress and $d\varepsilon_{ij}^{p}$ is the resulting increment in plastic strain.

$$d\sigma_{ij} \cdot d\varepsilon_{ij}^{p} \geq 0 \tag{5.2}$$

For metals, when the second increment of plastic work is positive, the stress-strain relation is ascending which is associated with stability. However, when it is negative, it means that the stress-strain curve is descending, it has passed the peak (where the second increment of plastic work is zero) and it is unstable (Figure 5.1).

The Hill's postulate is expressed in terms of both elastic and plastic (total) strain increments and is formulated in equation (5.3), where $d\varepsilon_{ij}^{t}$ is the total strain increment and $d\varepsilon_{ij}^{e}$ is the elastic strain increment.

$$d\sigma_{ij} \cdot d\varepsilon_{ij}^{t} = d\sigma_{ij} \cdot \left(d\varepsilon_{ij}^{e} \cdot d\varepsilon_{ij}^{p}\right) = d\sigma_{ij} \cdot d\varepsilon_{ij}^{e} + d\sigma_{ij} \cdot d\varepsilon_{ij}^{p} \geq 0 \tag{5.3}$$

The Hill's stability postulate goes a bit further in the definition of stability when compared to the Drucker's condition. However, these two conditions are sufficient to assure stability, but they are not necessary (Lade, 1992).

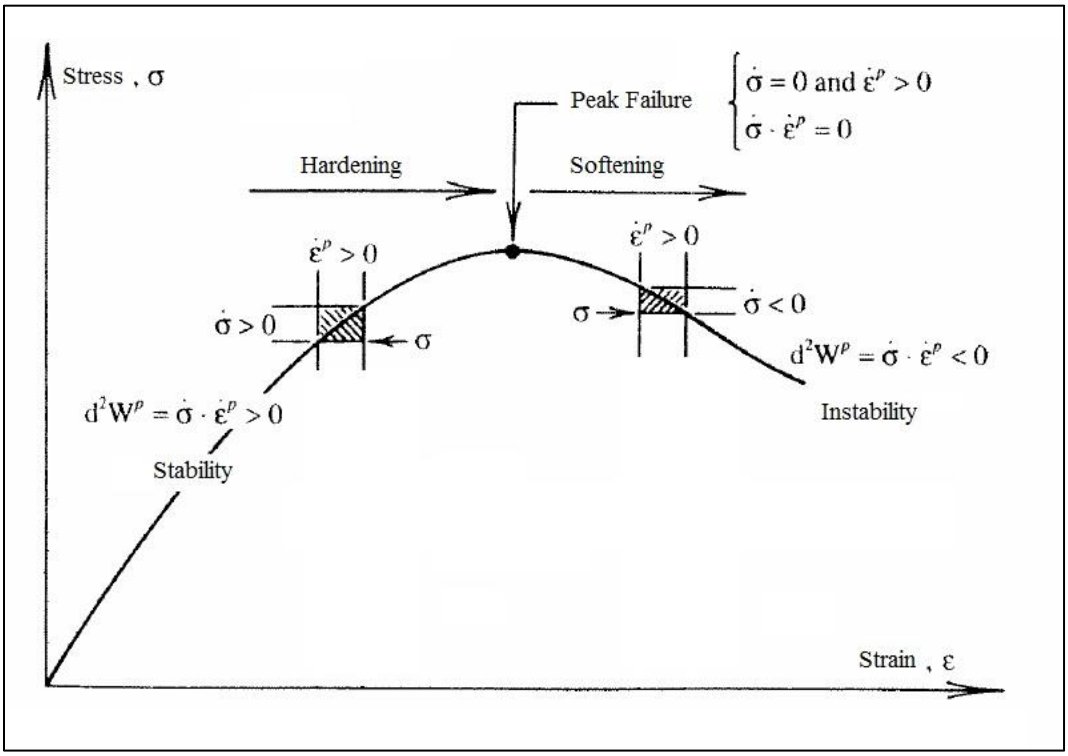

Figure 5.1 – Drucker's stability postulate for solid metals (Lade, 1994)

5.1.3. SECOND-ORDER WORK

One of the criteria for detecting the onset of instability in geomechanical systems is based on the second-order work. Hill (1958) was the first to propose this instability criterion and Bazant and Cedolin (1991) presented a demonstration based on the laws of thermodynamics to prove it. When the second-order work increment is zero instability can occur in the soil and the stress-path falls in the region of potential instability.

In a triaxial formulation, the second-order work is defined by equation (5.4), where dp' is the increment of effective mean stress, dq is the increment of deviatoric stress, $d\varepsilon_v$ is the change in volumetric strain and $d\varepsilon_s$ is the change in shear strain.

$$d^2W = dp' \cdot d\varepsilon_v + dq \cdot d\varepsilon_s \tag{5.4}$$

In an undrained compression triaxial test, the change in volumetric strain is zero. Therefore, the second-order work is zero if the increment in deviatoric stress is zero too. This proves that the peak of the deviatoric stress is a point where instability can begin because $d^2W = 0$.

$$\begin{gathered} d\varepsilon_v = 0 \rightarrow d^2W = dq \cdot d\varepsilon_s \\ d^2W = 0 \rightarrow dq = 0 \end{gathered} \tag{5.5}$$

5.1.4. INSTABILITY OF SOILS

Table 5.1 was compiled by Lade (1992) and it shows the conditions for stability and instability inside failure surface, based on a series of experimental observations on granular soils.

Table 5.1 – Experimental Observations of Conditions for Stability and Instability inside Failure Surface (Lade, 1992)

Soil volumetric behaviour	Dilation		Compression		
Drainage	Drained	Undrained	Drained	Undrained	
$d^2W > 0$	Stability[a]	Stability[a]	Stability[a]	Stability[a]	
$d^2W < 0$	Stability[b]	N.A.[c]	Stability[d]	Degree of Saturation	-
$d^2W < 0$	Stability[b]	N.A.[c]	Stability[d]	$S_r = 100\%$	Instability[e]
$d^2W < 0$	Stability[b]	N.A.[c]	Stability[d]	$S_r \geq (Sr)_{crit}$	Instability[d]
$d^2W < 0$	Stability[b]	N.A.[c]	Stability[d]	$S_r < (Sr)_{crit}$	Stability[d]

[a] Stability is guaranteed according to Drucker (1951), Bishop and Hill (1951) and Hill (1958)

[b] Shown by Lade et al. (1987)

[c] This combination cannot be achieved inside the failure surface

[d] Shown by Lade and Pradel (1990)

[e] Shown by Lade et al. (1988)

Stability and/or instability are directly related to the type of behaviour that the specimen shows when loaded (dilation or compression), the type of test conditions (drained or undrained) and, in case of undrained compression test, the degree of saturation. In the red rectangles represented in Table 5.1, the laboratory test conditions for the experimental data used in this work are highlighted. All tests present compressive plastic volumetric strain (drained) or generate positive excess pore pressure in the case of undrained tests, where the specimens were fully saturated. It can be concluded that the drained tests are always stable. For the undrained tests, when the second order work is negative, the soil follows to the region of potential instability, which is explained later.

5.1.5. LOCATION OF INSTABILITY LINE

Failure and instability are two different concepts when it comes to soils with nonassociated flow. According to Lade (1994), there are two criteria for definition of failure: (1) when the stress difference reaches a limiting value $(\sigma_1\text{-}\sigma_3)_{max}$; and, (2) when the effective principal stress ratio reaches a limiting value $(\sigma'_1/\sigma'_3)_{max}$. In drained tests, these conditions are reached at the same time so there is no problem in defining the failure line. However in undrained tests this does not happen. It is clear that the maximum stress difference occurs before the maximum effective stress ratio so it does not correspond to the true failure condition, but rather to the instability line. In the Critical State Theory, the failure line is defined by the Critical State Line (Subchapter 2.3.3.).

As it was stated previously, for undrained tests, the point where potential instability begins is defined by the top of the effective stress-path, corresponding to the peak in the deviatoric stress, $(\sigma_1\text{-}\sigma_3)_{max}$. After this point, the soil cannot sustain the current stress state and it can suffer plastic deformations under decreasing stresses, which leads to unstable behaviour. The line which connects these points for a series of undrained tests on loose sands is known as the instability line and it defines the lower limit of the region of potential instability (Lade, 1992). The Critical State Line (failure line) defines the upper limit of the region. In Figure 5.2, the instability line and the failure surface are represented.

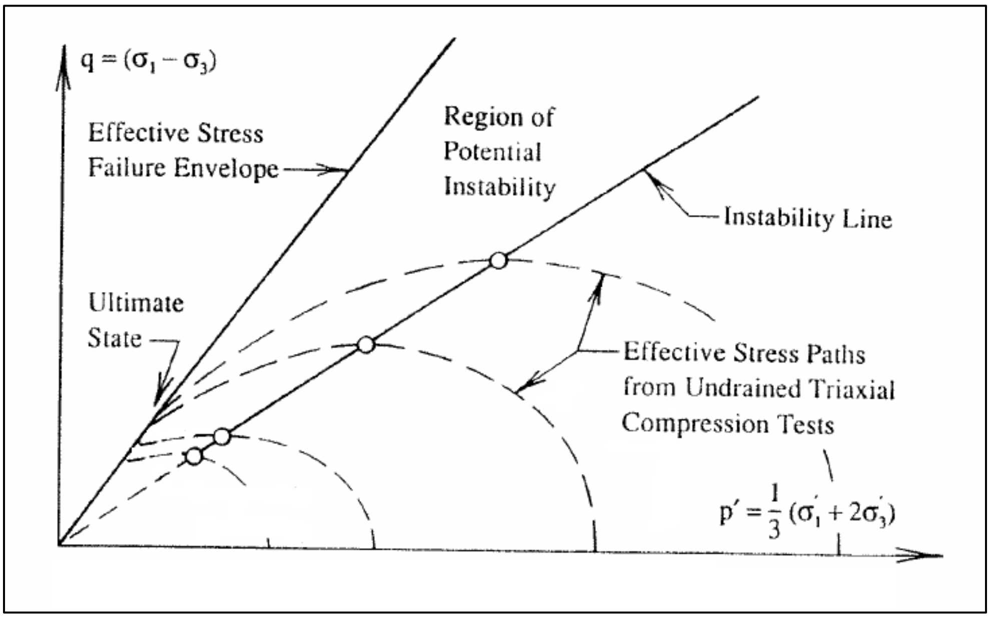

Figure 5.2 – Definition of the Instability Line (Lade, 1992)

5.1.6. INSTABILITY AND LIQUEFACTION

According to Lade (1994), in order to instability starts, it is required that the stress-path in the *q-p'* space is in the region of potential instability or is brought into it.

When dealing with undrained soils, the initiation of instability occurs for low values of strain. If the pore pressure increases faster than it can dissipate, the phenomenon of liquefaction may occur, for large strains. As it was discussed in Chapter 2, the grain size of the particles that constitute the soil influences the susceptibility to instability and consequent liquefaction. According to Mulilis *et al.* (1977), the initial grain fabric affects the susceptibility to instability, because instability starts at small strains. Hence, instability always precedes liquefaction and liquefaction only occurs if the instability line is crossed. As the grain fabric only influences the sand behaviour at low strains, this explains its relation with liquefaction, which takes place at large strains where the effects of initial grain structure would be negligible (Lade, 1994).

Figure 5.3 shows two examples of static stress-paths and stress-strain relations for loose sand. It is observed that instability initiates at small strains and after crossing the instability line while liquefaction happens at large strains.

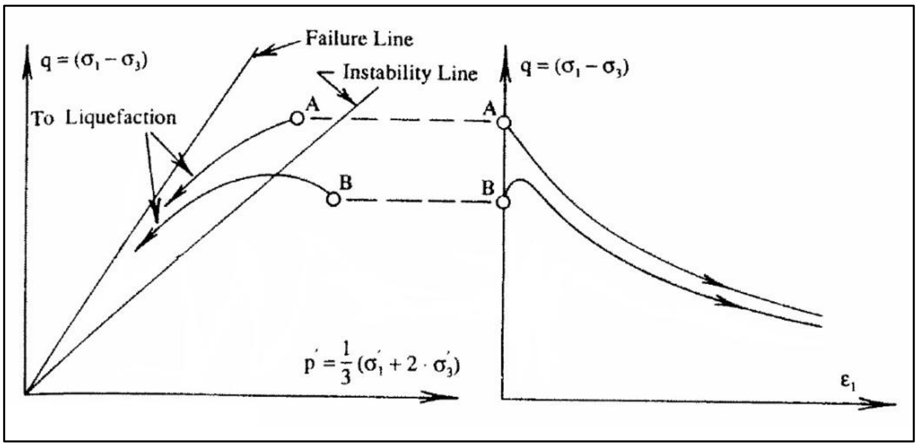

Figure 5.3 – Stress-path and stress-strain relations for loose sand in undrained conditions (Lade, 1994)

5.2. INSTABILITY OF *LES DUNES* SAND

5.2.1. INSTABILITY LINE FOR UNDRAINED TRIAXIAL TESTS

As it was shown in Chapter 4, the Clay and Sand Model (CASM), implemented in *Code_Bright*, is acceptable to model the results of triaxial drained and undrained tests performed on *Les Dunes* sand. Therefore, to define the instability line the results provided by the program were used. The location of instability line is defined by the values corresponding to the peak in the deviatoric stress. Table 5.2 presents, for the undrained tests, those values and Figure 5.4 shows the line plotted in *q-p'* space. When dealing with loose sands, as the ultimate state strength is very low, the instability line passes through the origin of the stress space (Lade, 1992).

Table 5.2 – Definition of the Instability Line

Designation Triaxial Test	q (kPa)	p' (kPa)
LD12	101.59	152.43
LD42	11.55	17.86
LD44	15.54	23.42
LD45	51.17	74.03
LD46	204.18	297.95
LD48	512.12	731.08

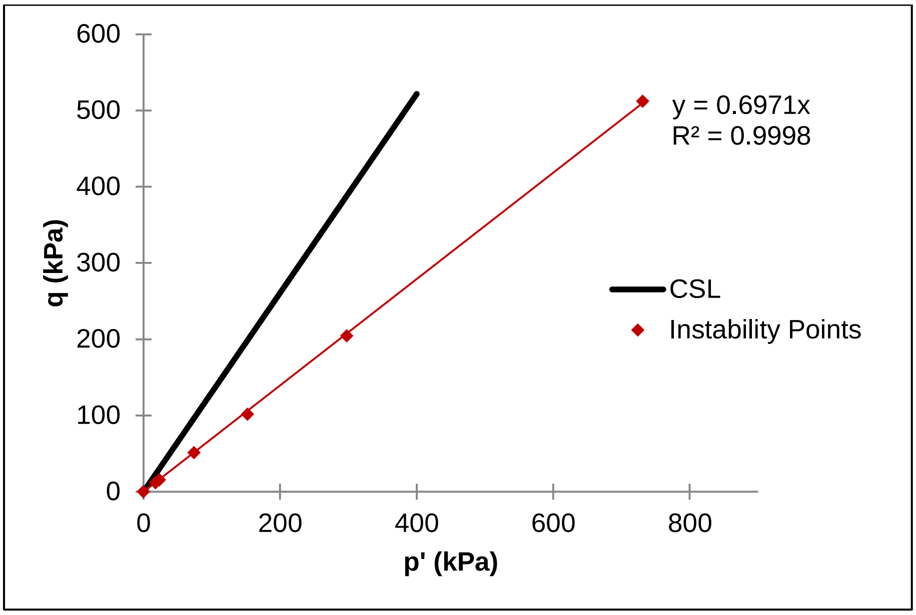

Figure 5.4 – Definition of the Instability Line

5.2.2. DRAINED TEST RESULTS AND INSTABILITY LINE

Figure 5.5 shows the simulation of the two drained tests performed. The stress-paths overpass the instability line and do not change their paths, consequently they stay stable. The number of drained triaxial tests is not enough to be absolutely conclusive, but it can be assumed that in principle for triaxial tests in drained conditions instability does not occur.

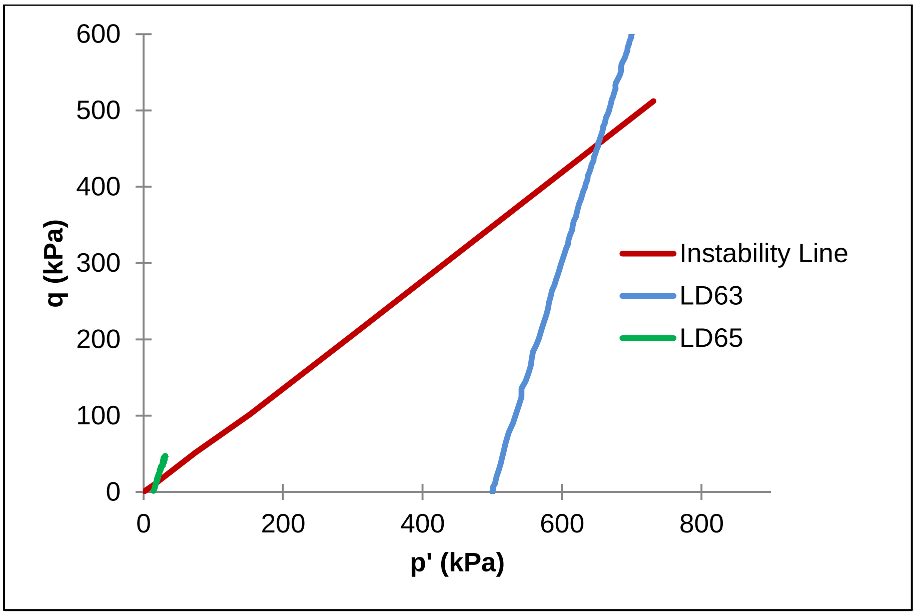

Figure 5.5 – Stress-paths of Drained Tests and Instability Line

5.2.3. SIMULATION OF DRAINED-UNDRAINED TESTS

After realizing that in undrained triaxial tests instability occurs, while for the drained tests it is not possible to identify an instable response, a simulation of that singular test (described in Subsection 3.3.2), when a specimen was first submitted to drained condition and then, at an intermediate loading level, the condition changed to undrained, i.e., the water flux in the specimen stops, was conducted to evaluate the sensibility of this model to detect the triggering of instability.

In this simulation the test starts to be drained and then becomes undrained, hence it is a hydro-mechanical (HM) coupled problem. Therefore, the options “Stress equilibrium (unknown displacement u)” and “Mass balance of water (unknown liquid pressure Pl)” were selected in the “Equations Solved” sheet, in “Problem Data” menu.

This experiment was conducted using the stress-path of the drained test LD63, implemented with a virtual change. In Table 5.3, the parameters computed in *Code_Bright* are defined.

Table 5.3 – Values of e_0, n, p'_0 and initial stress for the test

e_0	n	X stress (kPa)	Y stress (kPa)	Z stress (kPa)	p'_0 (kPa)
0.850	0.459	500	500	500	500

To reproduce the drained condition, in addition to the boundary conditions defined and explained in Chapter 4, it was imposed a Flux B. C. boundary on the top and bottom of the specimen. A high value of about 10^6 was selected for the coefficient Gamma for liquid (a leakage coefficient), to simulate the drainage.

The material parameters are the CASM parameters which are the same as the ones expressed in Table 4.5. As for the intrinsic permeability, inputted on the Hydraulic and Thermal data of the material, a value of that intrinsic permeability was selected to make the liquid pressure equalize zero in the drained test. That value was 10^{-8} m^2.

In this problem, two intervals were defined: the first with the conditions of a drained test, defined from the initial zero time until the final time when the drainage stops; the second interval begins when the first one ends and finishes at 250 hours. When the test becomes undrained (at interval 2), the Flux B.C. boundary conditions on top and bottom of the specimen are deactivated. The drainage stops and there is no water leaving the specimen.

The mesh is the same as the one used on the simulations of the laboratory triaxial tests in Subchapter 4.3.

In Figure 5.6 the stress-paths for several simulations are represented. In each, the drained process was stop at different times. The Critical State Line and the Instability Line are also represented, with the intention of being reference lines.

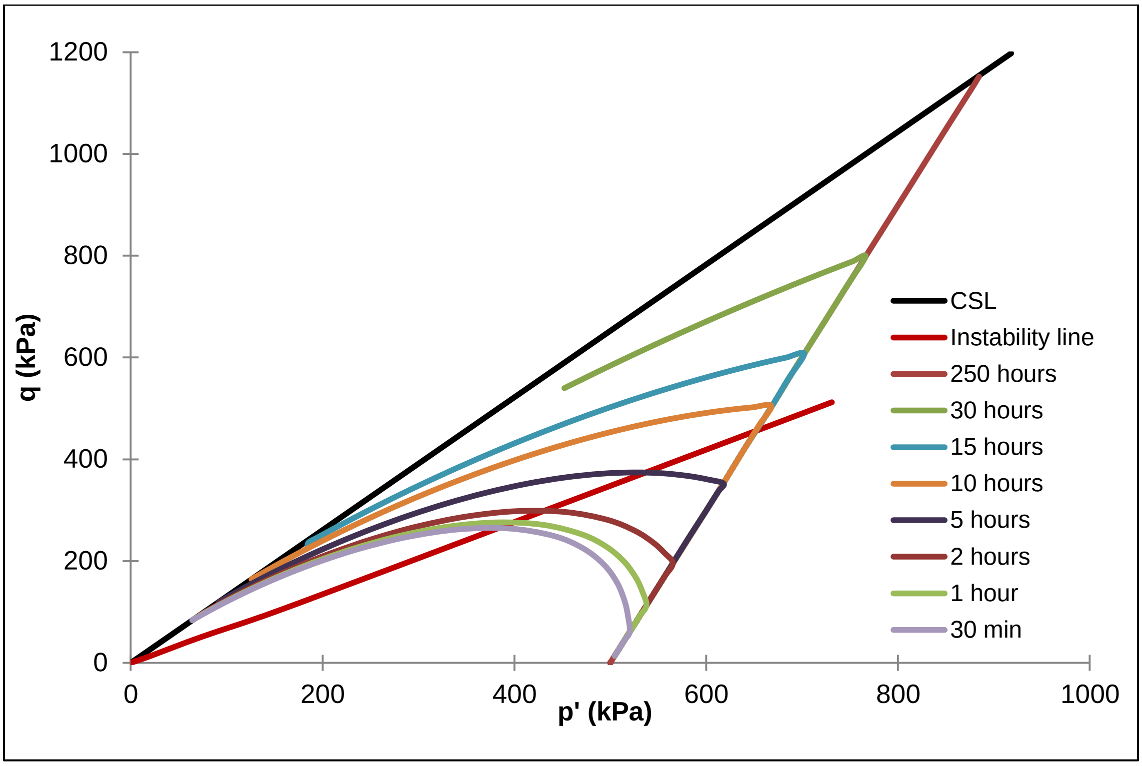

Figure 5.6 – Stress-paths of Drained-Undrained simulations

The stress-path for 250 hours represents the fully drained test. As it is shown in Figure 5.6, all tests performed follow the drained path until the moment they start to be undrained. For tests that start to be undrained after their stress-path passes the instability line, the moment they are under undrained conditions they are already instable. If a test starts to be undrained before reaching the instability line, it follows a typical undrained stress-path, with increase of the deviatoric stress while the effective mean stress decreases. The moment it reaches that instability line, the deviatoric stress begins to reduce. The peak of the deviatoric stress is really close to that point where the stress-path crosses the instability line, so it can be concluded that if a test changes from drained to undrained conditions before its path reaches the instability line, it stays stable. From the time when the two curves intersect the specimen is unstable and the deviatoric stress starts decreasing.

Observing Figure 5.6, it is also notable that the calculation process stops when the stress-paths reach the critical state line, except for the one for 30 hours in Flux B. C. condition. Table 5.4 presents the values of the deviatoric and effective mean stresses of the final point of each stress-path.

Table 5.4 – Final values of *q* and *p'* for each test

Time (hours)	q (kPa)	p' (kPa)
30	539.75	452.11
15	228.59	186.52
10	164.20	125.85
5	119.34	91.47
2	94.55	72.47
1	87.21	66.85
0.5	83.62	64.09

In Figure 5.7, the final point of each stress-path is represented along the Critical State Line. As it is shown, the stress-paths do not finish all in the same point. As the drained to undrained process occurs at different steps, the p'$_0$ value for each simulation is different and so the final point of each stress-path is different. Nevertheless, all the stress-paths finish at or near the Critical State Line, i. e., the failure line.

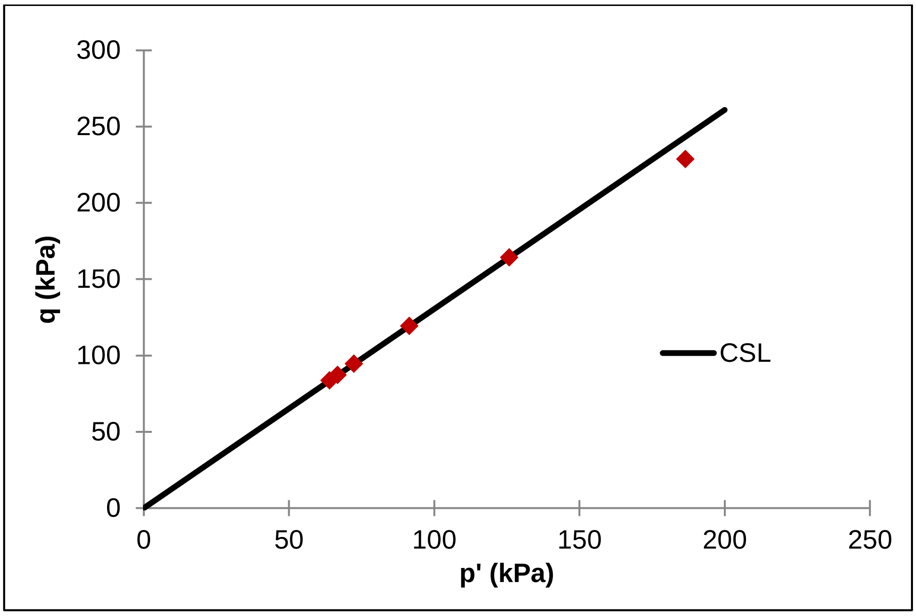

Figure 5.7 – Final points of the stress-paths and Critical State Line

5.2.4. SIMULATION OF LD64 TEST

In Subsection 3.3.2, some tests performed in the laboratory were described. As referred, one of the LD64 started to be performed under drained conditions but at a certain point, the BP valves had to be closed and the test became undrained. In this section, this test will be reproduced with *Code_Bright* to study the response of the code to this type of test and validate the simulations aforementioned.

The parameters of CASM, the geometry and the conditions are the same as the ones mentioned above. The specific parameters for the test are presented in Table 5.5.

Table 5.5 – Values of e_0, n, p'_0 and initial stresses for LD64

e_0	n	X stress (kPa)	Y stress (kPa)	Z stress (kPa)	p'_0 (kPa)
0.859	0.462	1000	1000	1000	1000

In order to find the time when the conditions change from drained to undrained, a complete drained test was simulated. The peak in the deviatoric stress in the test performed in the laboratory was at 1293.80 kPa. The results of the deviatoric stress *versus* time were exported from *Code_Bright*. After exporting the results of the drained test, it was found that the peak of the deviatoric stress occurred after 17.75 hours, so the test was turned to undrained at that time. Therefore, the computation was developed on two intervals. The first until 17.75 hours where the specimen was exposed to drained conditions and the second from 17.75 hours to 250 hours where the specimen was submitted to undrained conditions. Figure 5.8 shows the results from *Code_Bright* compared with the experimental data.

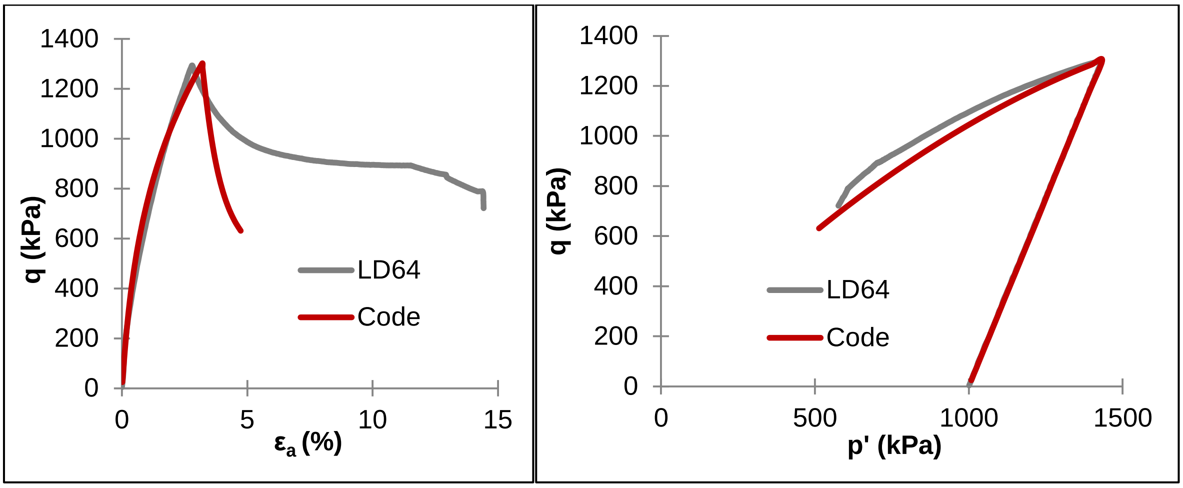

Figure 5.8 – LD64: Stress-strain curve and Stress-path

As it is observed in Figure 5.8, both the stress-strain curves and the stress-paths are similar. This means that *Code_Bright* is able to reproduce well this type of test control with CASM. When the test changes from drained to undrained conditions, the deviatoric stress decreases but the plastic strain does not stop. Softening is observed and the soil deforms plastically with decreasing levels.

In Figure 5.9, the stress-path is represented as well as the critical state line and the instability line defined for this sand. It is observed that when the test becomes undrained, the stress-path is already inside the region of potential instability. After that point, both the deviatoric and effective mean stresses decrease and the stress-path stops at the Critical State Line. As the Code cannot compute instability, the stress-path just follows the yield surface, as it is shown in Figure 5.10, where both the initial and final yield surfaces are drawn. As the test is, at first, drained, the yield surface expands. The yield surfaces were defined by equation (5.6). The value of p'_0 for the first yield surface is 1000 kPa and the value for the second is 3570.28 kPa. The last value of p'_0 was obtained by replacing the values of q and p' at the end of the drained part of the test in equation (5.7) (Table 5.6).

$$F = 0 \Rightarrow q = Mp'\left(ln\left(\frac{p'_0}{p'}\right)\frac{1}{ln\,r}\right)^{\frac{1}{n}} \tag{5.6}$$

$$p'_0 = e^{\left(\frac{q}{Mp'}\right)^n \ln r + \ln p'} \tag{5.7}$$

Table 5.6 – Value of *p'₀*

q (kPa)	p' (kPa)	p'$_0$ (kPa)
1301.50	1433.56	3570.28

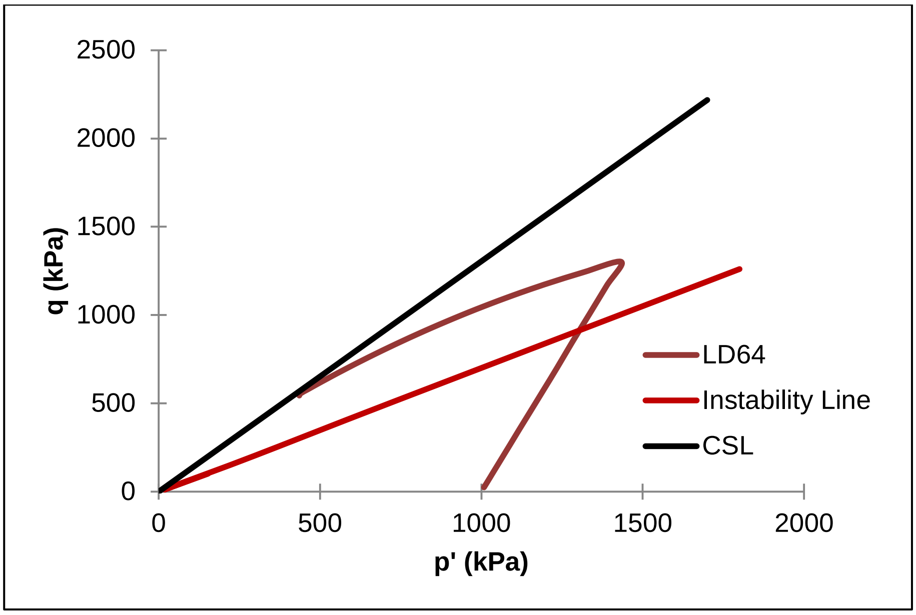

Figure 5.9 – LD64, CSL and instability line

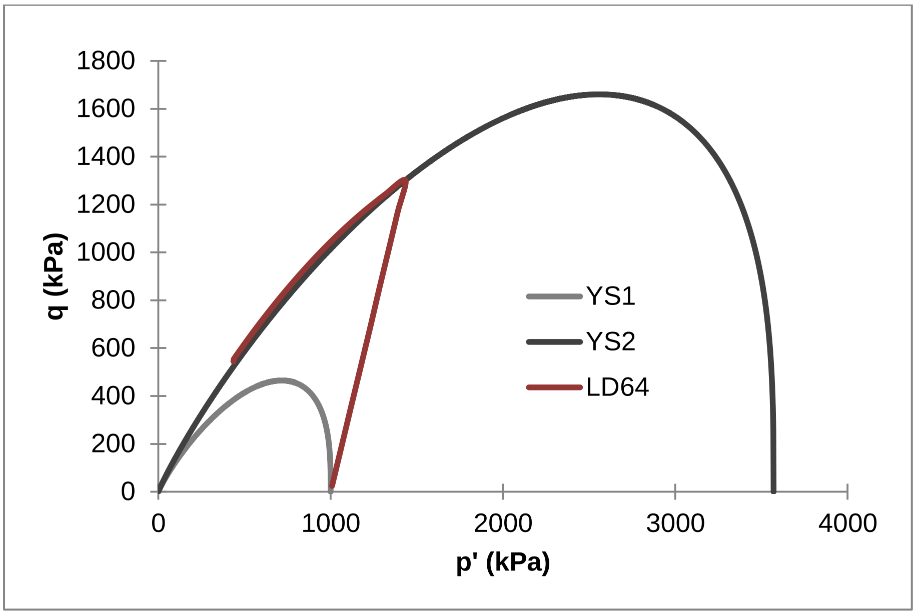

Figure 5.10 – LD64 and yield surfaces

5.3. DILATANCY RATE

According to Rowe (1962), the dilatancy and strength of a group of particles in contact when subjected to a deviatoric stress system depend on three main parameters: the friction angle between the surface of the particles, the geometrical angle of packing and the degree of energy loss during remolding.

The stress-dilatancy relation used in this work is due to Rowe (1962). As it was explained in Chapter 2, it defines the relation between stress ratio (η) and dilatancy rate (d) which is expressed on equation (5.8).

$$d = \frac{\delta \varepsilon_p^{\mathrm{p}}}{\delta \varepsilon_q^{\mathrm{p}}} = \frac{9(M - \eta)}{9 + 3M - 2M\eta} \tag{5.8}$$

For each undrained test, equation (5.8) was applied, using the deviatoric and effective mean stress values corresponding to the instability point.

Table 5.7 – Dilatancy rate for undrained tests at the instability point

Designation Triaxial Test	q (kPa)	p' (kPa)	η = q/p'	d
LD12	101.59	152.43	0.666	0.514
LD42	11.55	17.86	0.647	0.528
LD44	15.54	23.42	0.664	0.516
LD45	51.18	74.03	0.691	0.497
LD46	204.18	297.95	0.685	0.501
LD48	512.12	731.08	0.701	0.490

Analysing the values of the dilatancy rate obtained on each undrained test (Table 5.7), it can be concluded that the value of dilatancy for *Les Dunes* sand at the instability point is about 0.5. That means that when the dilatancy rate reaches the value of 0.5, the soil may experience instability.

Drained tests remain stable after their stress-path crosses the instability line. The dilatancy rate in the intersection point of the instability line and the drained test stress-path was studied. In Figure 5.11 the two lines for test LD63 are represented.

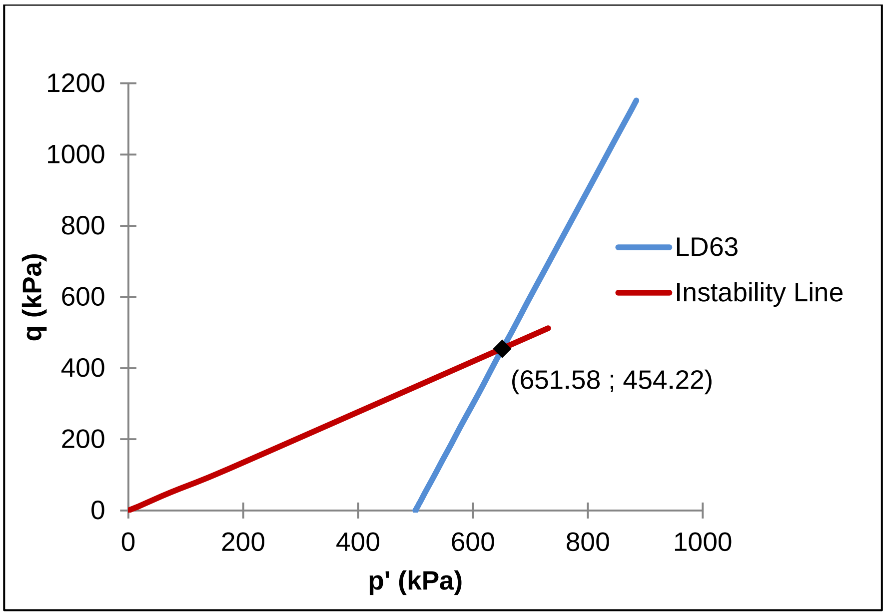

Figure 5.11 – LD63 stress-path and instability line

Equation (5.9) defines the stress-path while equation (5.10) defines the instability line.

$$q = 2.9969p' - 1498.5 \tag{5.9}$$

$$q = 0.6971p' \tag{5.10}$$

Solving the equation system, the values of the deviatoric and effective mean stress for the intersection point were found. Table 5.8 shows the results along with the value of the dilatancy rate calculated.

Table 5.8 – Dilatancy rate for the intersection point of LD63 with the instability line

q (kPa)	p' (kPa)	η	d
454.22	651.58	0.697	0.493

The same process was applied on the results of LD65 test. Figure 5.12 shows the intersection between the stress-path and the instability line, equation (5.11) defines the stress-path. In Table 5.9 the values of the deviatoric and effective mean stress at the intersection point and the dilatancy rate are represented. The equation of the instability line is the same presented on equation (5.10).

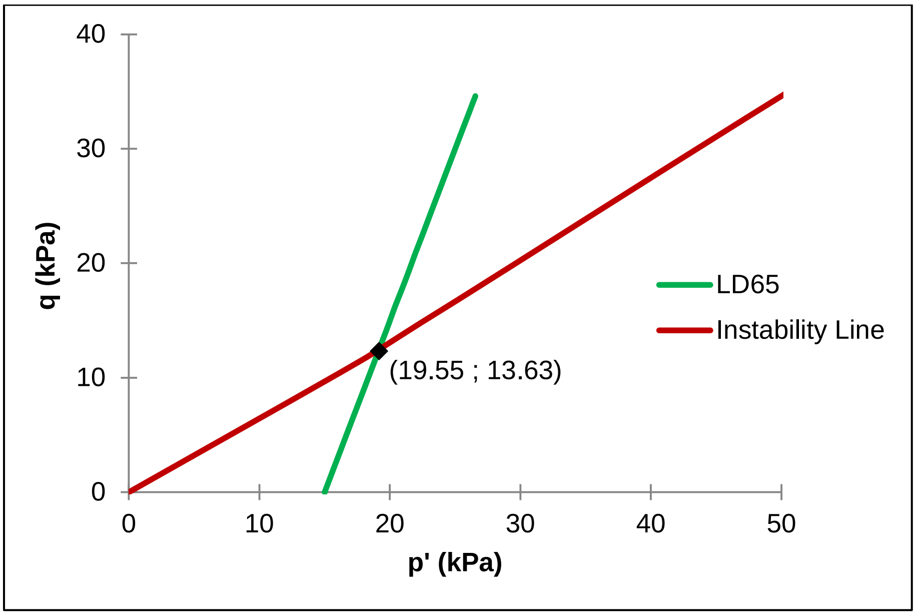

Figure 5.12 – LD65 stress-path and instability line

$$q = 29983p' - 44.98 \tag{5.11}$$

Table 5.9 – Dilatancy rate for the intersection point of LD65 with the instability line

q (kPa)	p' (kPa)	η	d
13.63	19.55	0.697	0.493

As for the test LD64, the change from drained to undrained conditions happened after the stress-path crossed the instability line. That way, the dilatancy rate at the point where the drained path intersects the instability line was studied. The process aforementioned was repeated for LD64 results. In Figure 5.13 the intersection between the stress-path and the instability line is shown, equation (5.12) defines the stress-path and in Table 5.10 the values of the deviatoric and effective mean stress at the intersection point and the dilatancy rate are represented. The equation of the instability line is the same presented on equation (5.10).

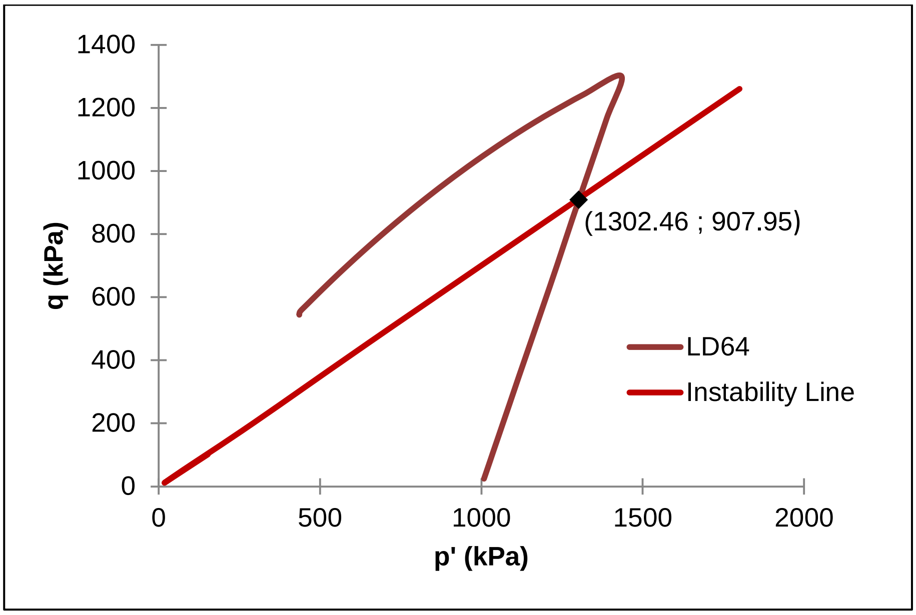

Figure 5.13 – LD64 stress-path and instability line

$$q = 3.0035p' - 3004 \tag{5.12}$$

Table 5.10 – Dilatancy rate for the intersection point of LD64 with the instability line

q (kPa)	p' (kPa)	η	d
907.95	1302.46	0.697	0.493

The instability line appears to be both related to a constant value of dilatancy (0.493) or a constant value of stress ratio (0.697). According to instability concept, it is the direction of plastic strain that initiate the instability and thus it is more rational to link the instability line to the value of dilatancy. However, as in CASM model the dilatancy depends only on the stress ratio (η), both concepts are equivalent. A conclusion of that is that the shape of the instability line in *p'*– *q* diagram (straight line) validates the assumption made for the dilatancy rule in CASM model. The model appears then to allow for modeling liquefaction in materials where instability line is a straight line in the *p'*– *q* space.

5.4. SECOND-ORDER WORK

In order to validate the described trends and to continue the study of instability in *Les Dunes* sand, the second-order work criterion was applied to the tests. Using the expression of equation (5.4) the second-order work increment was calculated for each step of the simulation. The values of the variables used in the expression for the definition of the second-order work increment were exported from *Code_Bright*.

5.4.1. DRAINED AND LD64 TESTS

The second-order work increment values were compared with the evolution of the axial strain for the drained tests. Figure 5.14 shows these relations for LD63 and LD65.

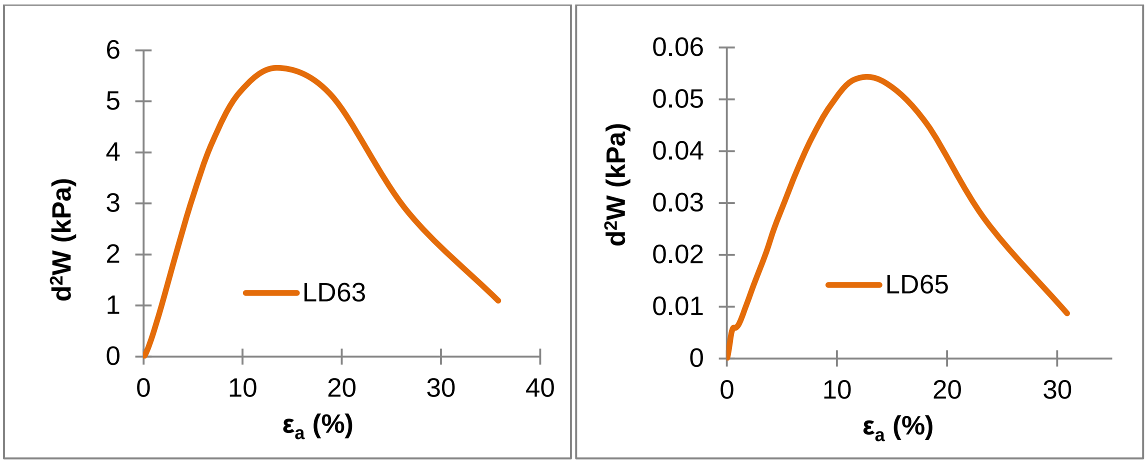

Figure 5.14 – Second-order work increment *versus* axial strain for drained tests

These results confirm what was defended above, for drained tests the second-order work increment is always positive so they are stable.

As LD64 stress-path crosses the instability line while under drained conditions, its analysis was considered in this subchapter. Figure 5.15 represent the evolution of the second-order work increment with axial strain and with time. In this case, it is important to reproduce the second-order work with time because, as it was explained before, this test starts to be drained and at 17.75 hours became undrained. As the stress-path has passed the instability line when the test starts to be undrained, it is inside the region of potential instability. As it is shown in Figure 5.15, when the time is 17.75 hours the second-order work is zero and starts to be negative, showing the instability of the specimen when it evolves in undrained conditions.

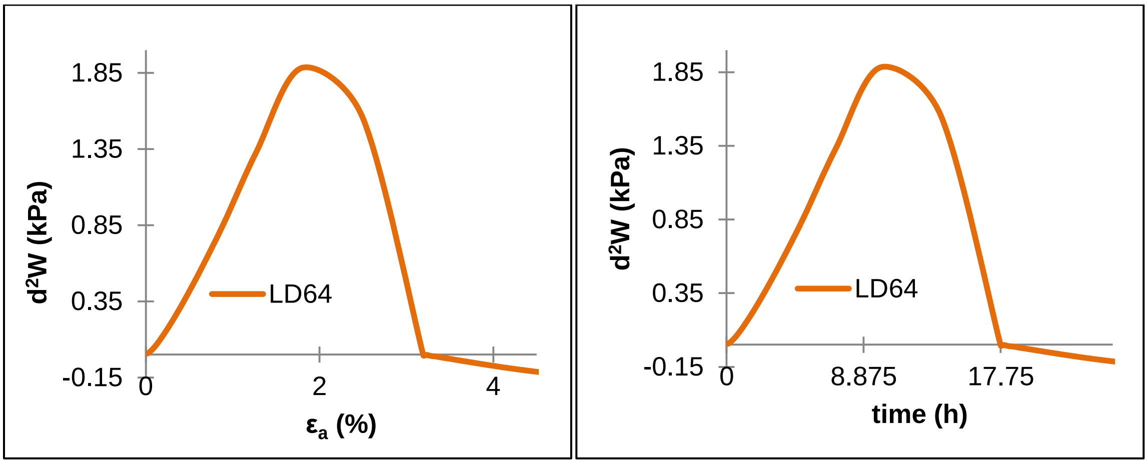

Figure 5.15 – Second-order work increment *versus* axial strain and time for LD64

5.4.2. Undrained Tests

The same procedure was applied to the undrained test results. In this case, the deviatoric stress was also represented, to show that when the second-order work increment is zero (starting to be negative) the deviatoric stress reaches a peak. Figures 5.16 to 5.21 present the results of the second-order work increment (orange curve) and the deviatoric stress (red curve) *versus* the axial strain. It can be concluded that when the second-order work increment is zero and begins to be negative, the deviatoric stress is maximum (and starts decreasing). This confirms the instability criterion explained above. The evolution and path of the second-order work increment was not an object of this study. However it would be interesting to study it in the future.

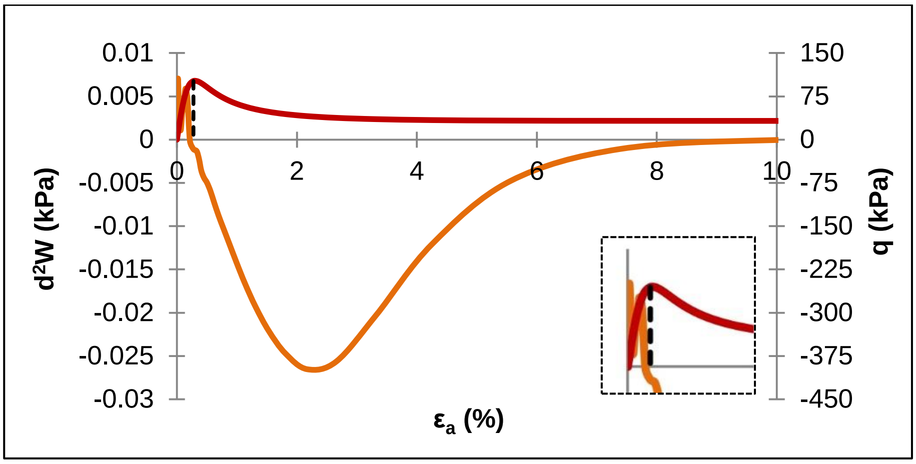

Figure 5.16 – Second-order work increment and deviatoric stress *versus* axial strain for LD12

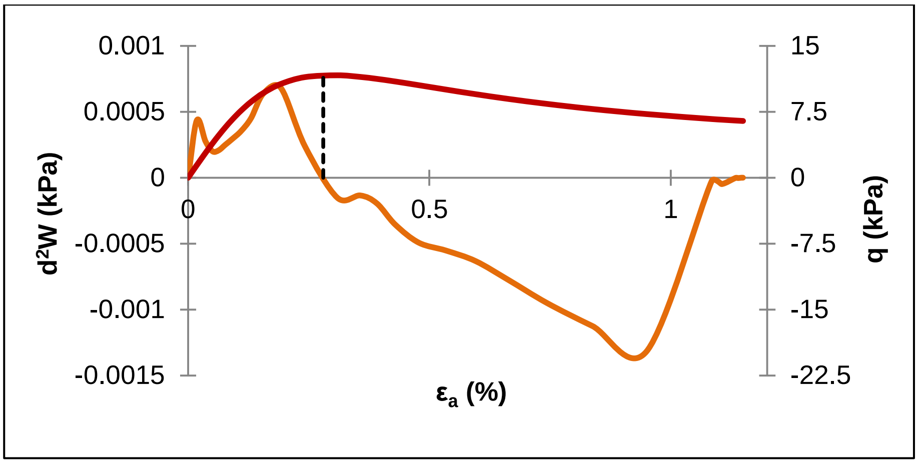

Figure 5.17 – Second-order work increment and deviatoric stress *versus* axial strain for LD42

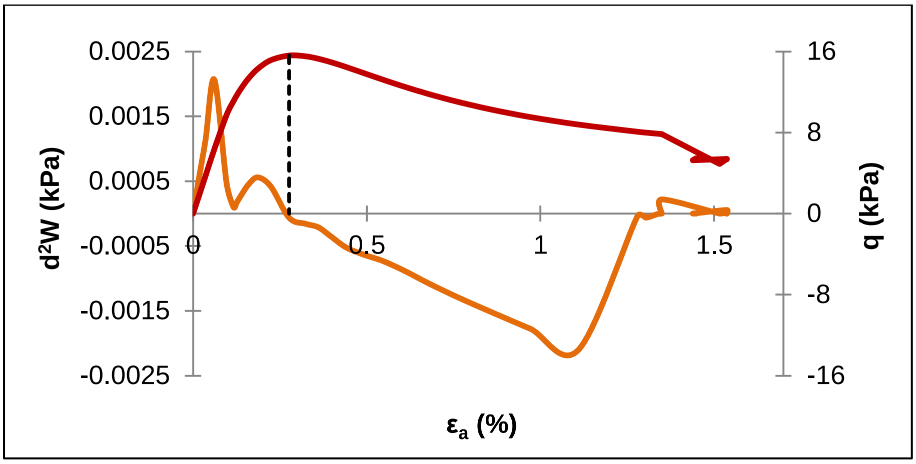

Figure 5.18 – Second-order work increment and deviatoric stress *versus* axial strain for LD44

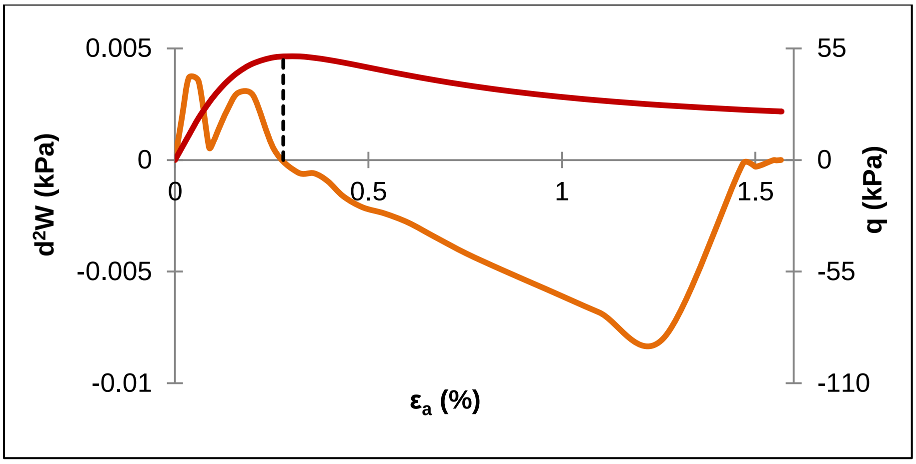

Figure 5.19 – Second-order work increment and deviatoric stress *versus* axial strain for LD45

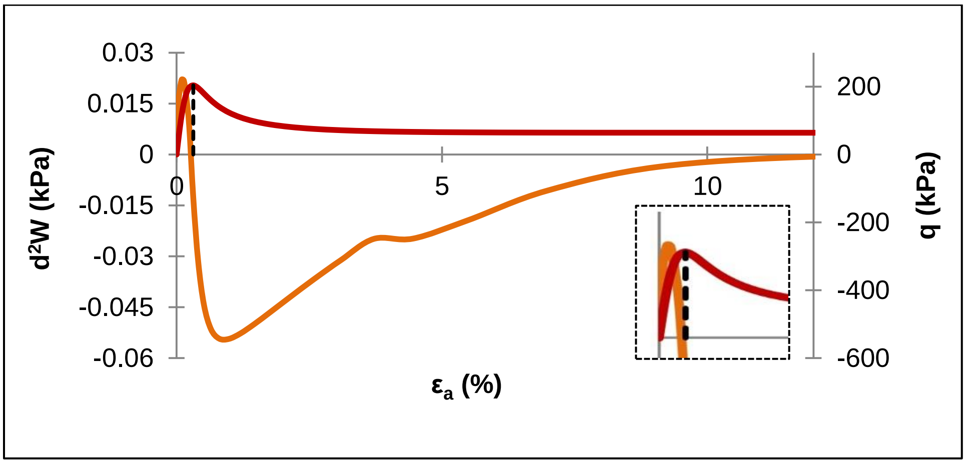

Figure 5.20 – Second-order work increment and deviatoric stress *versus* axial strain for LD46

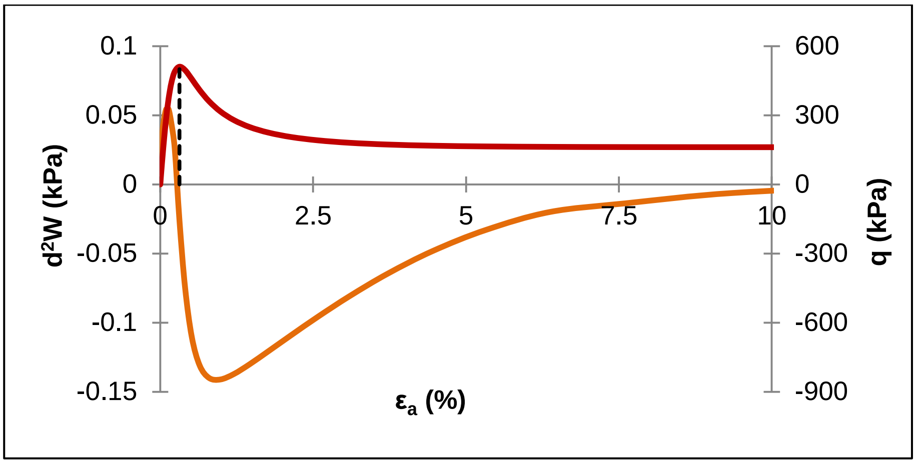

Figure 5.21 – Second-order work increment and deviatoric stress *versus* axial strain for LD48

5.4.3. DRAINED-UNDRAINED TESTS

It is also important to study the second-order work increment in the mixed tests simulated in *Code_Bright*. Figures 5.22 to 5.28 show the evolution of d^2W and the deviatoric stress with the time steps (in hours). In this analysis the horizontal axis was chosen to be the time instead of the axial strain, in order to evaluate what happens in the time step when the conditions change from drained to undrained.

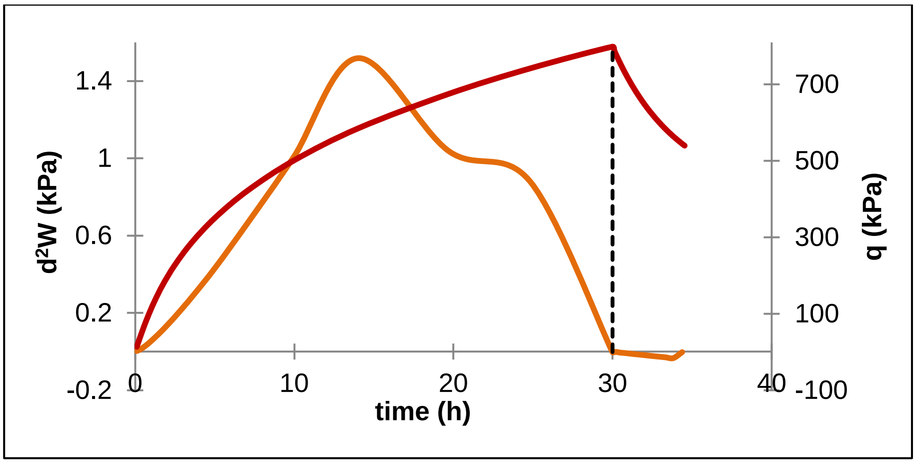

Figure 5.22 – Second-order work increment and deviatoric stress *versus* time for 30 h

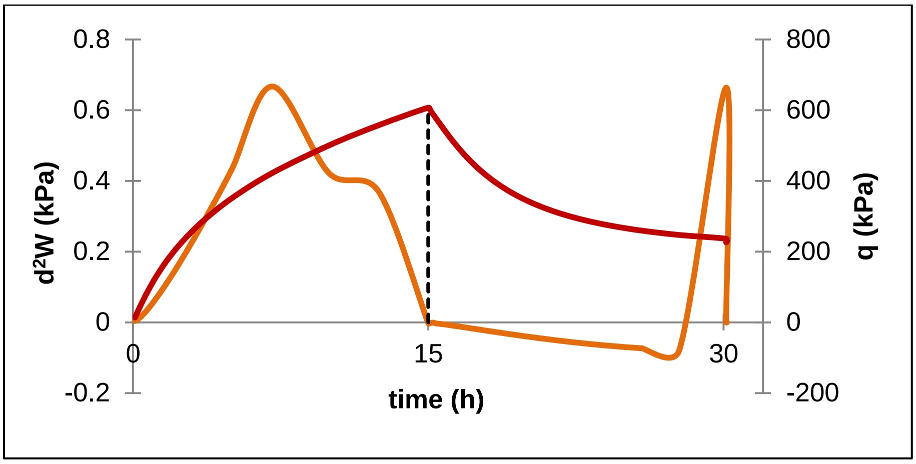

Figure 5.23 – Second-order work increment and deviatoric stress *versus* time for 15 h

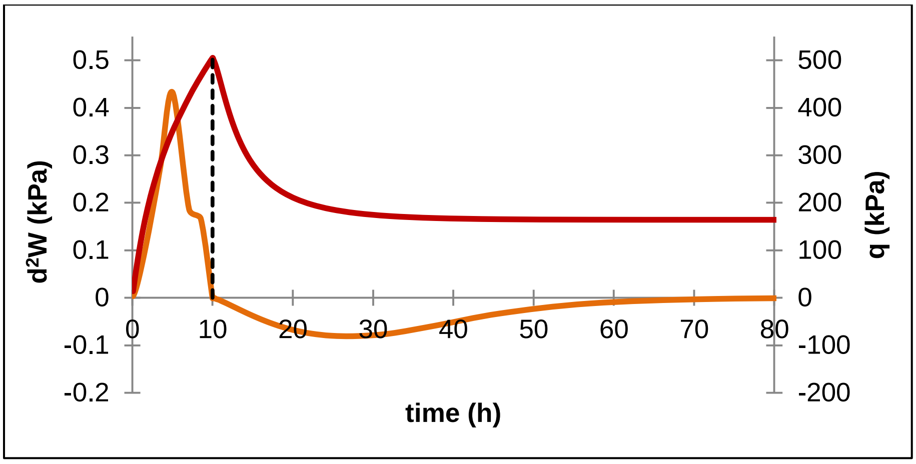

Figure 5.24 – Second-order work increment and deviatoric stress *versus* time for 10 h

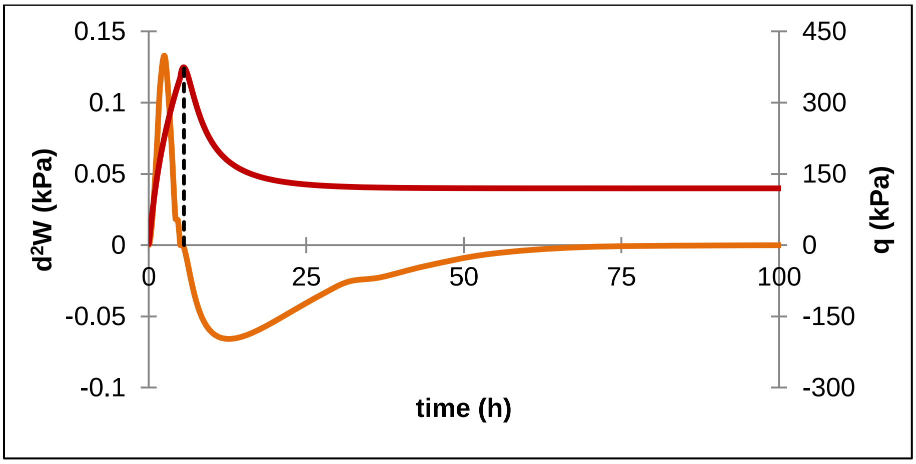

Figure 5.25 – Second-order work increment and deviatoric stress *versus* time for 5 h

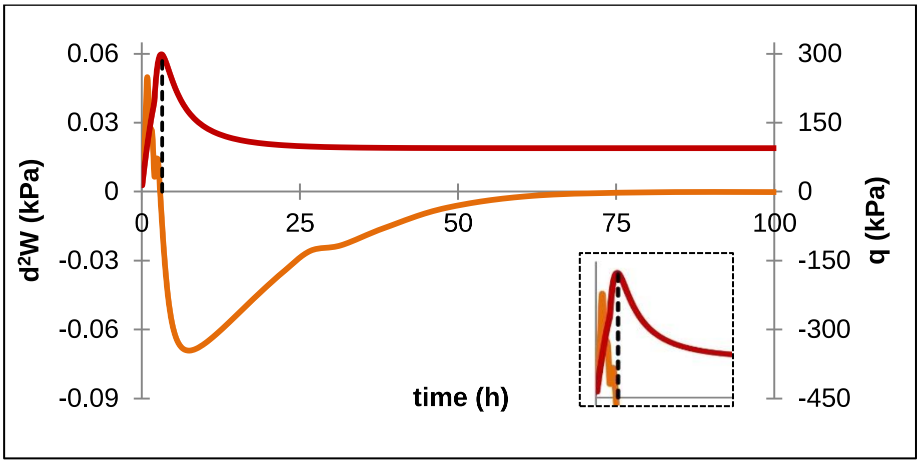

Figure 5.26 – Second-order work increment and deviatoric stress *versus* time for 2 h

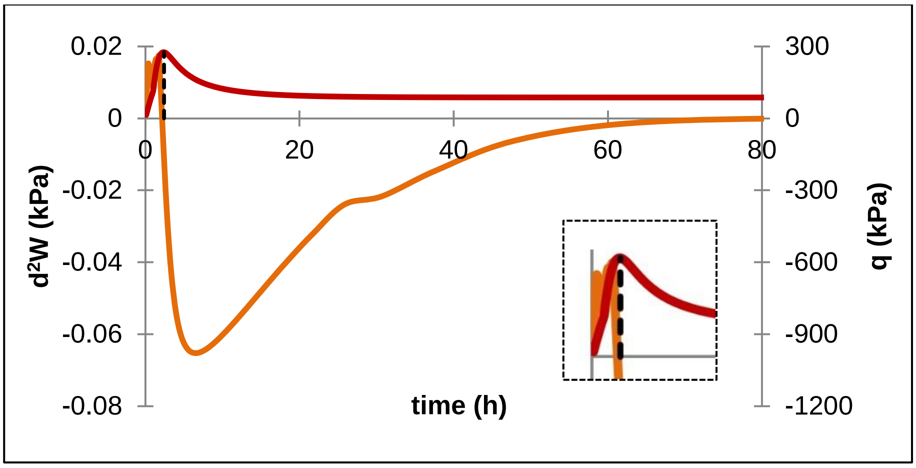

Figure 5.27 – Second-order work increment and deviatoric stress *versus* time for 1 h

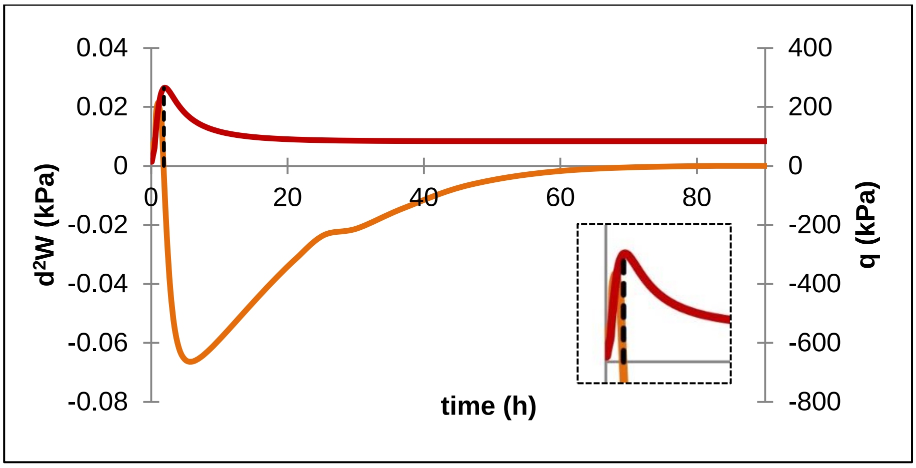

Figure 5.28 – Second-order work increment and deviatoric stress *versus* time for 30 min

Observing the Figures above, some conclusions can be made. First, for the tests that overpass the instability line under drained conditions and only after that turned to undrained conditions (30h, 15h and 10h), the second-order work increment is zero in the exact time when the test starts to be undrained. This is justified by the fact that the stress-path is inside the region for potential instability so, when the conditions change to undrained the peak of the deviatoric stress is by definition this same value of q and it starts to drop. As for the tests that change to undrained conditions while the stress-path lies under the instability line (5h, 2h, 1h and 30min), they stay stable until crossing that line. The peak of the deviatoric stress is reached when the stress-path crosses the instability line, in a time step after the time when undrained conditions start. Table 5.11 shows the values of the time steps when instability begins and in Figure 5.29 those points are represented.

Table 5.11 – Time step and q and p' values for the instability points

Time (hours)	Time step (hours)	q (kPa)	p' (kPa)
30	30.00	798.56	766.16
15	15.00	607.36	702.16
10	10.00	505.00	667.80
5	5.60	374.23	516.32
2	3.24	298.13	402.80
1	2.42	276.00	382.70
0.5	1.87	264.13	394.09

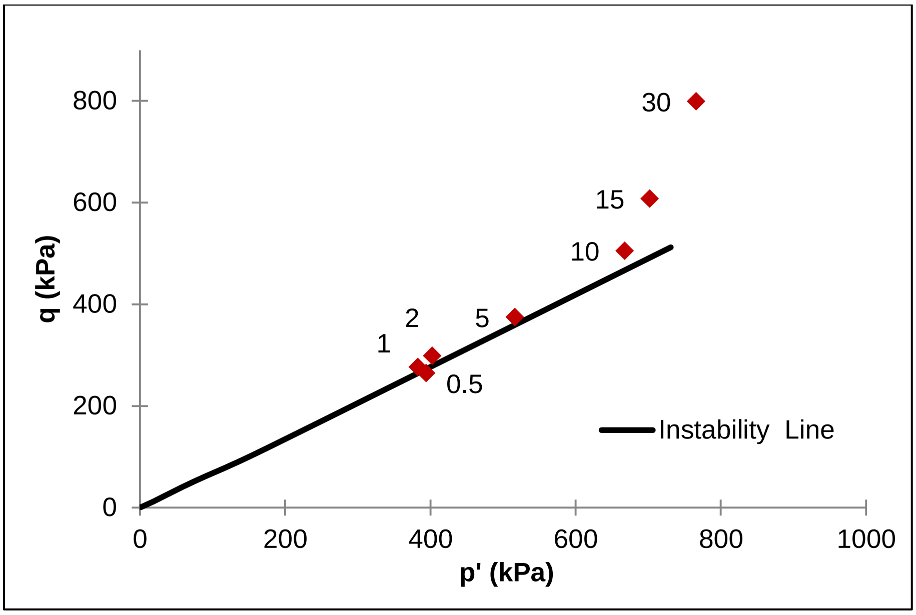

Figure 5.29 – Instability points for each test

5.5. DEFINITION OF CSL, NCL AND INSTABILITY LINE IN *e*-LN *P'* SPACE

In this part of the work, after the determination of the instability line, it would be interesting to define the Normal Compression Line, the Critical State Line and the Instability line in *e*-ln*p'* space and evaluate the differences between them.

In Figure 5.30 two yield surfaces obtained by the expression of CASM (equation (2.32) in Subchapter 2.4.2.) are represented. For each yield surface, the values of *p'* correspondent to the NCL, instability line and CSL are related, by expressions as the ones represented in equations 5.13 to 5.15, which are directly proportional with a common constant.

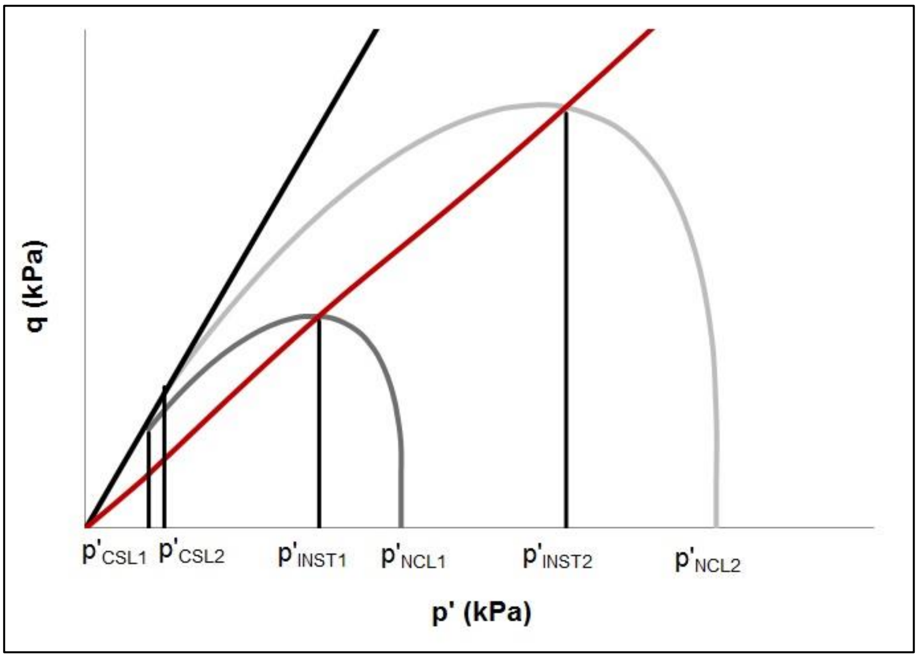

Figure 5.30 – Relation between p' in CSL, NCL and instability line

$$p'_{CSL1} = \alpha\, p'_{NCL1} \tag{5.13}$$

$$p'_{CSL2} = \alpha\, p'_{NCL2} \tag{5.14}$$

$$p'_{CSL} = \alpha\, p'_{NCL} \tag{5.15}$$

The equation of the CSL was defined with the results of some drained and undrained tests performed in *Les Dunes* sand (presented previously in Figure 4.3). In equation (5.16) its expression is represented.

$$e = -0.021 \ln p' + 0.9659 \tag{5.16}$$

The NCL is defined by the values of p'_0 , the first point of the stress-path and it is parallel to the CSL. To define its equation, the value of *p'* in equation (5.16) has to be replaced by a value related with p'_0.

To determine this value, the expression of the yield surface, defined in equation (2.32) of Subchapter 2.4.2. was equated to the expression of the CSL in the Critical State Theory (equation (2.14) in subchapter 2.3.4.), as it is shown in the expression (5.16).

$$Mp' = Mp'\left(ln\left(\frac{p'_0}{p'}\right)\frac{1}{ln\,r}\right)^{\frac{1}{n}} \tag{5.17}$$

The result is an expression that relates p' with p'_0 (equation (5.18)).

$$p' = \frac{p'_0}{r} \tag{5.18}$$

Replacing the value of p' in equation (5.17), the NCL is defined in e-lnp' space as being (5.19).

$$e = -0.021\ln p'_0 + (0.021\ln r + 0.9659) \tag{5.19}$$

To define the instability line, its equation is equated by the yield function (equation (5.20)).

$$0.6971p' = Mp'\left(ln\left(\frac{p'_0}{p'}\right)\frac{1}{ln\,r}\right)^{\frac{1}{n}} \tag{5.20}$$

The result is an expression that relates ln p' with a function containing p'_0 (equation (5.21)).

$$\ln p' = \ln p'_0 - \left(\frac{0.6971}{M}\right)^n \ln r \tag{5.21}$$

Replacing the value of ln p' in equation (5.17), the instability line is defined in e-lnp' space as being (5.22).

$$e = -0.021\ln p'_0 + 0.021\left(\frac{0.6971}{M}\right)^n \ln r + 0.9659 \tag{5.22}$$

In Figure 5.31 the three lines are represented. The parameters of the sand were replaced in the expressions above. It can be concluded that the instability line is also parallel to the CSL and NCL and it is situated between them. The instability line is closer to the CSL than to the NCL.

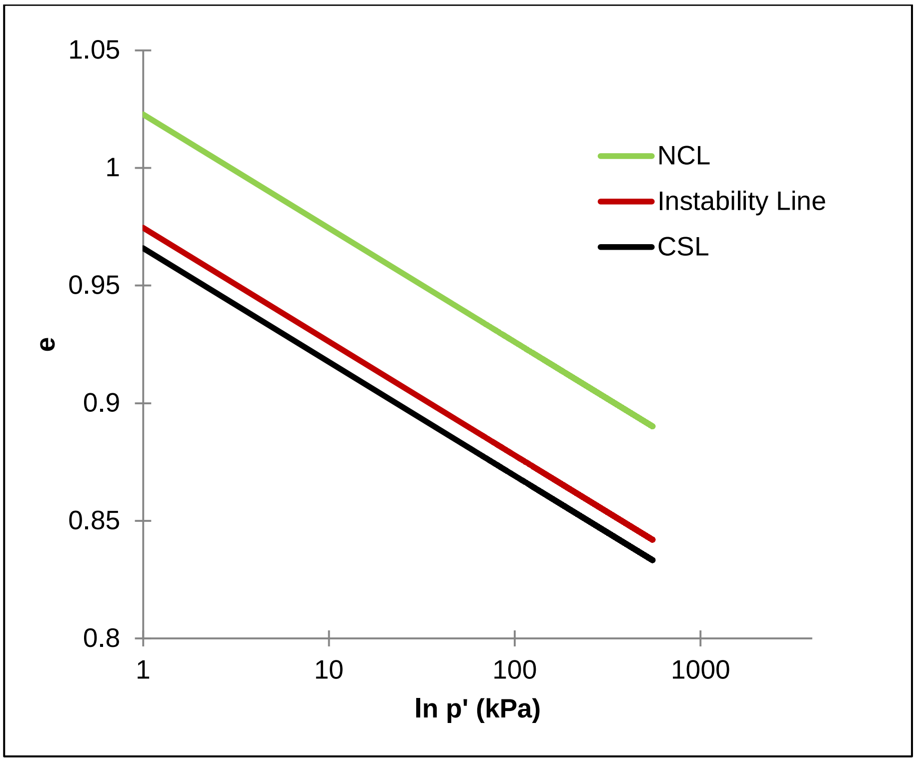

Figure 5.31 – CSL, NCL and Instability line in *e*- lnp' space

6
CONCLUSIONS

6.1. CONCLUSIONS

The aim of this work was to continue the study of *Les Dunes* sand, from a beach in Ain Benian in Algeria, where liquefaction occurred during the 2003 Boumerdès earthquake. This study was done based on a critical state model for clays and sand (CASM), developed by Yu (1998). This was chosen because it is a simple and unified formulation that has been proven suitable for modelling sand behaviour.

First, a comparison between experimental data and the CASM model was done. CASM is implemented in *Code_Bright*, so in order to compare the results of the model with the laboratory data, some tests with the same characteristics were simulated. The results were very satisfactory, therefore, it can be concluded that CASM is a valid and good model to compute and simulate the real *Les Dunes* sand behaviour observed under both drained and undrained conditions. The n and r parameters are essential to define the yield surface shape. They are specific for the model and depend on the type of soil that is being study. Comparing the yield surface from CASM with the stress path obtained from the laboratory tests, the value of these parameters were found to be n = 3 and r = 15. When dealing with *Code_Bright*, some numerical instability was observed during the reproduction of the physical instability. To avoid this problem, the initial time step was increased. The numerical results are once again very similar to the experimental ones.

For the study of instability, the second order work increment criterion was applied. The instability line was proven to be a straight line, passing in the peak of the deviatoric stress in $q – p'$ space, for the undrained tests. According to this criterion, a specimen under drained conditions is never unstable. When under undrained conditions, the specimen may become unstable after its stress-path crosses the instability line and enters the region of potential instability. This was also confirmed with the simulation of drained-undrained tests. These tests start to be drained and at different time the conditions were changed to undrained. It was concluded that if the undrained conditions start when the stress-path has already cross the instability line, the specimen may already be unstable (second order work increment is zero in that point). If a test starts to be undrained before reaching the instability line, it stays stable. It is only when the path crosses the instability line that the second order work increment is zero and instability may occur.

As for the dilatancy rate, proposed by Rowe (1962), it was proven to be around 0.49 in the point where the stress-paths intersect the instability line. In CASM the dilatancy depends on the stress ratio, which controls the dilatancy rate, so in this case, the value of the stress ratio is the slope of the instability line. The shape of the instability line in $p' - q$ diagram (straight line) validates the assumption made for the dilatancy rule in CASM model.

In conclusion, the results found can lead to a better understanding and modelling of instabilities in saturated granular soils and can help the continuation of the study of *Les Dunes* sand and the soil susceptibility for liquefaction.

6.2. FUTURE DEVELOPMENTS

As in any study of model validation, the quantity and quality of the experimental results are very important. To assure that a model is valid and can be used to simulate a specific soil behaviour, the results of the simulations have to be compared with further experimental data on other soils. In this work, there were used two drained tests and six undrained test.

It would be important to perform more undrained and drained triaxial tests, to better define the critical state line and the instability line as well as the sand parameters. When dealing with this type of study, the more extensive experimental data the more reliable will be the reproduction of real soil behaviour.

Other future development is to compute the instability in *Code_Bright*. A lot of numerical and programing work has to be done in order to improve the abilities of this Code. It would be a significant improvement if *Code_Bright* could simulate the results until the annulment of the mean effective stress (liquefaction). Further developments would be the reproduction of the point of dilation (phase transformation point) with the Code. This would be very important to correctly simulate liquefaction and distinguish the perfect liquefaction (with annulment of the stresses) from the temporary instability.

REFERENCES

Alonso, E. E., Gens, A., Josa, A. (1990). *A constitutive model for partially saturated soils*. Géotechnique 40(3): 405-430.

Andrade, J. E. (2009). *A predictive framework for liquefaction instability*. Géotechnique 59 (8), 673-682.

Andrade, J. E., Ramos, A. M. and Lizcano, A. (2013). *Criterion for flow liquefaction instability*. Acta Geotechnica

Atkinson, J. (1993). *Introduction to the Mechanics of Soils and Foundations*. McGraw-Hill International Series in Civil Engineering, London, U.K.

Bazant, Z. and Cedolin, L. (1991). Stability of structures. Elastic, inelastic, fracture and damage theories. Dover Publications, Mineola, New York.

Been, K. and Jefferies, M.G. (1985). *A state parameter for sands*. Géotechnique 35(2), 99–112.

Bouhadad, Y. et al. (2004). *The Boumerdes (Algeria) earthquake of May 21, 2003 (Mw=6.8): Ground deformation and intensity.* Journal of seismology, 09/03/2004, pp. 497-506, Kluwer Academic Publishers.

Cañón, A. M. R. (2010). *Instability in Sands*. PhD Thesis, Faculty of Engineering Universidad de los Andes.

Drucker, D. C. (1959). *A definition of stable inelastic material*, J. appl. Mech., 26, 101-106.

Drucker, D. C., Gibson, R. E. and Henkel, D. J. (1957*). Soil mechanics and work hardening theories of plasticity*. Proc. ASCE, 122, 338-346.

Earthquake Engineering Research Institute (2003). *The Boumerdes, Algeria, Earthquake of May 21, 2003*. Oakland, California

Fonseca, M. (2009). *Derivação em triaxial cíclico de parâmetros de estado e de acção sísmica que induziram liquefacção de areias dunares num sismo em Argel*. Master Thesis, FEUP.

Gens, A. and Nova, R. (1993). *Conceptual bases for a constitutive model for bonded soils and weak rocks*. Engineering for Hard Soils-Soft Rocks, Athens, Greece, Anagnostopoulos et sl. (eds.) Rotterdam: Balkema, 577-583

González, N. A. (2011). *Development of a family of constitutive models for Geotechnical applications*. PhD Thesis, UPC, Barcelona

Head, K. H. and Epps, R. J. (2011). *Manual of Soil Laboratory Testing Volume II – Permeability, Shear Strength and Compressibility Tests 3rd Edition*. Whittles Publishing, Scotland, U.K.

Hill, R. (1958). *A general theory of uniqueness and stability in elastic-plastic solids*. J. MEch, Phvs, Solids, 6, 236-249.

Imposimato, S. and Nova, R. (1998). *An investigation on the uniqueness of the incremental response of elastoplastic models for virgin sand*. Mechanics of Cohesive-Frictional Materials. 3, No. 1, 65-87, Milan, Italy.

Ishihara, K. (1985). *Stability of natural deposits during earthquakes*. Proc. 11st Int. Conf. on Soil Mechanics and Foundation Engineering. San Francisco.

Kim, M. K. and Lade, P. V. (1988). *Single Hardening Constitutive Model For Frictional Materials, I. Plastic Potencial Function*. Computers and Geotechnics, 5, 307-324, England.

Kramer, S. (1996). *Geotechnical Earthquake Engineering*. Prentice Hall International Series, New Jersey.

Lade, P. V. (1992). *Static Instability and Liquefaction of Loose Fine Sandy Slopes*. Journal of Geotechnical Engineering, Vol. 118, No1

Lade, P. V. (1994). *Instability and Liquefaction of Granular Materials*. Computers and Geotechnics, 16, 123-151, California, U. S. A..

Matos Fernandes, M. (2006). *Mecânica dos Solos – Conceitos e Princípios Fundamentais*. FEUP Edições, Porto.

Muir Wood, D. (1990). *Soil Behaviour and Critical State Soil Mechanics*. Cambridge University Press, Cambridge.

Mulilis, J. P., Seed, H. B., Chan, C. K., Mitchell, J. K. and Arulanandan, K. (1977) *Effects of sample preparation on sand liquefaction*. J. Geotech. Engr. Div. ASCE, 103: 91-108.

National Reaserch Council (1985). *Liquefaction of soils during earthquakes*. Washington, DC: National Academy Press.

Ortigao, J. A. R. (1995). *Soil Mechanics in the Light of Critical State Theories – An Introduction*. A. A. Balkema, Rotterdam, Netherlands.

Pinheiro, A. (2009). *Avaliação em laboratório das condições de estado que conduziram a fenémenos de liquefacção de areias dunares no sismo de 2003 em Boumerdès"*. Master Thesis, FEUP.

Potts, D. M. and Zdravković, L. (1999). *Finite element analysis in geotechnical engineering Theory*. Thomas Telford Publishing, London.

Rocha, J. (2010). *Definição em condições de liquefacção em triaxial à luz da teoria dos estados críticos e avaliação do risco por razão de velocidades de ondas sísmicas numa areia dunar*. Master Thesis, FEUP.

Rocha, J. & Viana da Fonseca, A. *Susceptibilidade à liquefacção de uma areia dunar avaliada em ensaios de laboratório com medição de velocidade de ondas sísmicas*. Submetido em Julho 2010, Publicado na Revista nº 121, pp. 3-16 em Março de 2011

Roscoe, K. H. and Burland, J. B. (1968). *On the generalized stress-strain behaviour of wet clay*. In: Engineering Plasticity, pp. 535-609. Cambridge University Press, Cambridge.

Roscoe, K. H., Schofield, A. N. and Wroth, C. P. (1958). *On the Yielding of Soils*. Géotechnique, 8(1), 22-53.

Rowe, P. W. (1962). *The stress-dilatancy relation for static equilibrium of an assembly of particles in contact*. Proc. Roy. Soc., 267, 500-527.

Schanz, T., Vermeer, P. A. and Bonnier, P. G. (1999). *Formulations and verification of the Hardening-Soil Model*. Beyond 2000 in Computacional Geotechnics, 281-290, Balkema, Rotterdam.

Schofield, A. and Wroth, P. (1968). Critical State Soil Mechanics. McGraw-Hill, London, U.K.

Sheng, D., Sloan, S. W. and Yu, H. S. (2000). *Aspects of finite element implementation of critical state models*. Computational Mechanics 26, 185-196.

Silva, S. (2011). *A General Framework for the Geomechanical Characterization of Artificial Cemented Soil.* PhD Thesis, FEUP.

Terzaghi, K.; Peck, R. B.; Mesri, G. (1996). *Soil Mechanics in Engineering Practice, 3rd Ed*. Wiley-Interscience.

Tsuchida H. (1970) *Prediction and Countermeasure Against the Liquefaction in Sand Deposits.* in Japanese in abstract of the Seminar in the Port and Harbor Research Institute pp 3.1-3.33.

Viana da Fonseca, A., Rocha, J., Tahar, G. (2011). *Liquefaction assessment charts on state and waves' velocities from static and cyclic triaxial tests on 'Les Dunes" sands from Algier*. 5th Intern. Conf. on Earthquake Geotech. Engin., Santiago, Chile, Jan. 10-13, Pub. In CD (Apres.oral). (www.5icege.cl/images/stories/congress_sessions/papers/session_8/8.1.COLVI.pdf).

Viana da Fonseca, A. & Soares, M. (2012). *Effect of principal stress rotation on cyclic liquefaction*. Second International Conference on Performance-Based Design in Earthquake Geotechnical Engineering, Taormina, Italy, 28-30 May (http://www.2pbd-taormina.org). Publicado on-line

Yu, H. S. (1998). *CASM: A Unified State Parameter Model for Clay and Sand*. International Journal of Numerical and Analytical Methods in Geomechanics, 22, 621-653.

APPENDIX A

IMPLEMENTATION OF CASM ELASTO-PLASTIC MODEL FOR TRIAXIAL PATH

A.1. ELASTIC LAW

$$\begin{bmatrix} d\sigma'_x \\ d\sigma'_y \\ d\sigma'_z \\ d\sigma'_{xy} \\ d\sigma'_{xz} \\ d\sigma'_{yz} \end{bmatrix} = \frac{E}{(1-2\nu)(1+\nu)} \begin{bmatrix} 1-\nu & \nu & \nu & 0 & 0 & 0 \\ \nu & 1-\nu & \nu & 0 & 0 & 0 \\ \nu & \nu & 1-\nu & 0 & 0 & 0 \\ 0 & 0 & 0 & \frac{1-2\nu}{2} & 0 & 0 \\ 0 & 0 & 0 & 0 & \frac{1-2\nu}{2} & 0 \\ 0 & 0 & 0 & 0 & 0 & \frac{1-2\nu}{2} \end{bmatrix} \begin{bmatrix} d\varepsilon_x^e \\ d\varepsilon_y^e \\ d\varepsilon_z^e \\ 2d\varepsilon_{xy}^e \\ 2d\varepsilon_{xz}^e \\ 2d\varepsilon_{yz}^e \end{bmatrix} \tag{A.1}$$

$$\begin{bmatrix} d\varepsilon_x^e \\ d\varepsilon_y^e \\ d\varepsilon_z^e \\ 2d\varepsilon_{xy}^e \\ 2d\varepsilon_{xz}^e \\ 2d\varepsilon_{yz}^e \end{bmatrix} = \frac{1}{E} \begin{bmatrix} 1 & -\nu & -\nu & 0 & 0 & 0 \\ -\nu & 1 & -\nu & 0 & 0 & 0 \\ -\nu & -\nu & 1 & 0 & 0 & 0 \\ 0 & 0 & 0 & 2(1+\nu) & 0 & 0 \\ 0 & 0 & 0 & 0 & 2(1+\nu) & 0 \\ 0 & 0 & 0 & 0 & 0 & 2(1+\nu) \end{bmatrix} \begin{bmatrix} d\sigma'_x \\ d\sigma'_y \\ d\sigma_{,z} \\ d\sigma'_{xy} \\ d\sigma'_{xz} \\ d\sigma'_{yz} \end{bmatrix} \tag{A.2}$$

With:

$$E = 3K(1-2\nu) \tag{A.3}$$

And

$$K = \frac{(1+e)p}{\kappa} \tag{A.4}$$

In triaxial conditions, noting x and y are the radial directions (principal directions 2 and 3) and z is the axial direction (principal direction 1):

$$d\sigma'_x = d\sigma'_y = d\sigma'_3\ ;\ d\sigma'_z = d\sigma'_1\ ;\ d\sigma'_{xy} = d\sigma'_{xz} = d\sigma'_{yz} = 0$$

$$d\varepsilon^e_x = d\varepsilon^e_y = d\varepsilon^e_3\ ;\ d\varepsilon^e_z = d\varepsilon^e_1\ ;\ d\varepsilon^e_{xy} = d\varepsilon^e_{xz} = d\varepsilon^e_{yz} = 0$$

The elastic law reads,

$$d\sigma'_1 = \frac{3K}{(1+\nu)}\left[(1-\nu)d\varepsilon^e_1 + 2\nu d\varepsilon^e_3\right] \tag{A.5}$$

$$d\sigma'_3 = \frac{3K}{(1+\nu)}\left[\nu\, d\varepsilon^e_1 + d\varepsilon^e_3\right] \tag{A.6}$$

A.2. YIELD FUNCTION AND DERIVATIVES

$$F = \left(\frac{q}{Mp'}\right)^n + \ln\left(\frac{p'}{p'_0}\right)\frac{1}{\ln r} \leq 0 \tag{A.7}$$

In triaxial conditions:

$$F = \left(\frac{3(\sigma'_1 - \sigma'_3)}{M(\sigma'_1 + 2\sigma'_3)}\right)^n + \ln\left(\frac{\sigma'_1 + 2\sigma'_3}{3p'_0}\right)\frac{1}{\ln r} \leq 0 \tag{A.8}$$

With

$$\frac{\partial F}{\partial \sigma'_1} = n\left(\frac{3(\sigma'_1 - \sigma'_3)}{M(\sigma'_1 + 2\sigma'_3)}\right)^{n-1}\frac{9\sigma'_3}{M(\sigma'_1 + 2\sigma'_3)^2} + \frac{1}{\ln r\,(\sigma'_1 + 2\sigma'_3)} \tag{A.9}$$

$$\frac{\partial F}{\partial \sigma'_3} = n\left(\frac{3(\sigma'_1 - \sigma'_3)}{M(\sigma'_1 + 2\sigma'_3)}\right)^{n-1}\frac{-9\sigma'_1}{M(\sigma'_1 + 2\sigma'_3)^2} + \frac{2}{\ln r\,(\sigma'_1 + 2\sigma'_3)} \tag{A.10}$$

A.3. PLASTIC POTENTIAL AND FLOW RULE

$$g(p,q,\beta) = G = 3M\ln\frac{p'}{\beta} + (3+2M)\ln\left(\frac{2q}{p'}+3\right) - (3-M)\ln\left(3-\frac{q}{p'}\right) = 0 \tag{A.11}$$

In triaxial conditions:

$$\begin{aligned} G = 3M\ln\left(\frac{\sigma'_1+2\sigma'_3}{3\beta}\right) + (3+2M)\ln\left(\frac{6(\sigma'_1-\sigma'_3)}{\sigma'_1+2\sigma'_3}+3\right) \\ -(3-M)\ln\left(3-\frac{3(\sigma'_1-\sigma'_3)}{\sigma'_1+2\sigma'_3}\right) \end{aligned} \tag{A.12}$$

The flow rule reads,

$$d\varepsilon_1^p = \frac{\partial G}{\partial\sigma'_1}d\lambda \tag{A.13}$$

$$d\varepsilon_3^p = \frac{\partial G}{\partial\sigma'_3}d\lambda \tag{A.14}$$

With

$$\frac{\partial G}{\partial\sigma'_1} = \frac{3+2M}{\sigma'_1} \tag{A.15}$$

$$\frac{\partial G}{\partial\sigma'_3} = \frac{M-3}{\sigma'_3} \tag{A.16}$$

A.4. HARDENING LAW

$$\frac{dp'_0}{p'_0} = \frac{\nu}{\lambda-\kappa}d\epsilon_p^p = \frac{\nu}{\lambda-\kappa}\frac{\partial G}{\partial p'}d\lambda \tag{A.17}$$

With

$$\frac{\partial G}{\partial p'} = \frac{1}{p'}\left(3M - (3+2M)\frac{2q}{2q+3p'} - (3-M)\frac{q}{3p'-q}\right) \tag{A.18}$$

A.5. TANGENT MATRIX FOR STRAIN CONTROLLED TRIAXIAL STRESS PATH ($d\varepsilon_1$, $d\varepsilon_2=d\varepsilon_3$ WITH $\sigma_2=\sigma_3$)

If elastic: $d\varepsilon_1 = d\varepsilon_1^e$; $d\varepsilon_3 = d\varepsilon_3^e$

$$d\sigma'_1 = D_{11}^e d\varepsilon_1 + D_{13}^e d\varepsilon_3 \tag{A.19}$$

$$d\sigma'_3 = D_{31}^e d\varepsilon_1 + D_{33}^e d\varepsilon_3 \tag{A.20}$$

With

$$D_{11}^e = \frac{3K(1-\nu)}{(1+\nu)} \tag{A.21}$$

$$D_{13}^e = \frac{6K\nu}{(1+\nu)} \tag{A.22}$$

$$D_{31}^e = \frac{3K\nu}{(1+\nu)} \tag{A.23}$$

$$D_{33}^e = \frac{3K}{(1+\nu)} \tag{A.24}$$

If elasto-plastic: $d\varepsilon_1 = d\varepsilon_1^e + d\varepsilon_1^p$; $d\varepsilon_3 = d\varepsilon_3^e + d\varepsilon_3^p$

$$dF = 0 = \frac{\partial F}{\partial \sigma'_1} d\sigma'_1 + \frac{\partial F}{\partial \sigma'_3} d\sigma'_3 + \frac{\partial F}{\partial p'_0} dp'_0$$

$$\frac{\partial F}{\partial \sigma'_1}\left[D_{11}^e\left(d\varepsilon_1 - \frac{\partial G}{\partial \sigma'_1} d\lambda\right) + D_{13}^e\left(d\varepsilon_3 - \frac{\partial G}{\partial \sigma'_3} d\lambda\right)\right] + \frac{\partial F}{\partial \sigma'_3}\left[D_{31}^e\left(d\varepsilon_1 - \frac{\partial G}{\partial \sigma'_1} d\lambda\right) + D_{33}^e\left(d\varepsilon_3 - \frac{\partial G}{\partial \sigma'_3} d\lambda\right)\right] + \frac{\partial F}{\partial p'_0}\frac{\partial p'_0}{\partial \lambda} d\lambda = 0$$

$$\left[-\left(\frac{\partial F}{\partial \sigma'_1} D_{11}^e \frac{\partial G}{\partial \sigma'_1} + \frac{\partial F}{\partial \sigma'_1} D_{13}^e \frac{\partial G}{\partial \sigma'_3} + \frac{\partial F}{\partial \sigma'_3} D_{31}^e \frac{\partial G}{\partial \sigma'_1} + \frac{\partial F}{\partial \sigma'_3} D_{33}^e \frac{\partial G}{\partial \sigma'_3}\right) + \frac{\partial F}{\partial p'_0}\frac{\partial p'_0}{\partial \lambda}\right] d\lambda = -\left(\frac{\partial F}{\partial \sigma'_1} D_{11}^e + \frac{\partial F}{\partial \sigma'_3} D_{31}^e\right) d\varepsilon_1 - \left(\frac{\partial F}{\partial \sigma'_1} D_{13}^e + \frac{\partial F}{\partial \sigma'_3} D_{33}^e\right) d\varepsilon_3$$

$$d\lambda = \frac{\left(\frac{\partial F}{\partial \sigma'_1} D_{11}^e + \frac{\partial F}{\partial \sigma'_3} D_{31}^e\right)}{H - H_{cr}} d\varepsilon_1 + \frac{\left(\frac{\partial F}{\partial \sigma'_1} D_{13}^e + \frac{\partial F}{\partial \sigma'_3} D_{33}^e\right)}{H - H_{cr}} d\varepsilon_3 \tag{A.25}$$

With

$$H = -\frac{\partial F}{\partial p'_c}\frac{\partial p'_c}{\partial \lambda} \tag{A.26}$$

$$\frac{\partial F}{\partial p'_c} = -\frac{1}{p'_c \ln r} \tag{A.27}$$

$$\frac{\partial p'_c}{\partial \lambda} = \frac{(1+e)}{(\lambda-\kappa)} p'_c \frac{\partial G}{\partial p'} \tag{A.28}$$

$$H_{cr} = -\left(\frac{\partial F}{\partial \sigma'_1} D^e_{11} \frac{\partial G}{\partial \sigma'_1} + \frac{\partial F}{\partial \sigma'_1} D^e_{13} \frac{\partial G}{\partial \sigma'_3} + \frac{\partial F}{\partial \sigma'_3} D^e_{31} \frac{\partial G}{\partial \sigma'_1} + \frac{\partial F}{\partial \sigma'_3} D^e_{33} \frac{\partial G}{\partial \sigma'_3}\right) \tag{A.29}$$

By substituting $d\varepsilon^e_1 = d\varepsilon_1 - \frac{\partial G}{\partial \sigma'_1} d\lambda$ and $d\varepsilon^e_3 = d\varepsilon_3 - \frac{\partial G}{\partial \sigma'_3} d\lambda$ in the elastic law:

$$\begin{cases} d\sigma'_1 = D^e_{11}\left(d\varepsilon_1 - \frac{\partial G}{\partial \sigma'_1} d\lambda\right) + D^e_{13}\left(d\varepsilon_3 - \frac{\partial G}{\partial \sigma'_3} d\lambda\right) \\ d\sigma'_3 = D^e_{31}\left(d\varepsilon_1 - \frac{\partial G}{\partial \sigma'_1} d\lambda\right) + D^e_{33}\left(d\varepsilon_3 - \frac{\partial G}{\partial \sigma'_3} d\lambda\right) \end{cases}$$

$$\begin{cases} d\sigma'_1 = D^{ep}_{11} d\varepsilon_1 + D^{ep}_{13} d\varepsilon_3 \\ d\sigma'_3 = D^{ep}_{31} d\varepsilon_1 + D^{ep}_{33} d\varepsilon_3 \end{cases} \tag{A.30}$$

With

$$D^{ep}_{11} = D^e_{11} - \frac{D^e_{11}\frac{\partial F}{\partial \sigma'_1}\frac{\partial G}{\partial \sigma'_1}D^e_{11} + D^e_{11}\frac{\partial F}{\partial \sigma'_1}\frac{\partial G}{\partial \sigma'_3}D^e_{31} + D^e_{13}\frac{\partial F}{\partial \sigma'_3}\frac{\partial G}{\partial \sigma'_1}D^e_{11} + D^e_{13}\frac{\partial F}{\partial \sigma'_3}\frac{\partial G}{\partial \sigma'_3}D^e_{31}}{H - H_{cr}} \tag{A.31}$$

$$D^{ep}_{13} = D^e_{13} - \frac{D^e_{11}\frac{\partial F}{\partial \sigma'_1}\frac{\partial G}{\partial \sigma'_1}D^e_{13} + D^e_{11}\frac{\partial F}{\partial \sigma'_1}\frac{\partial G}{\partial \sigma'_3}D^e_{33} + D^e_{13}\frac{\partial F}{\partial \sigma'_3}\frac{\partial G}{\partial \sigma'_1}D^e_{13} + D^e_{13}\frac{\partial F}{\partial \sigma'_3}\frac{\partial G}{\partial \sigma'_3}D^e_{33}}{H - H_{cr}} \tag{A.32}$$

$$D^{ep}_{31} = D^e_{31} - \frac{D^e_{31}\frac{\partial F}{\partial \sigma'_1}\frac{\partial G}{\partial \sigma'_1}D^e_{11} + D^e_{31}\frac{\partial F}{\partial \sigma'_1}\frac{\partial G}{\partial \sigma'_3}D^e_{31} + D^e_{33}\frac{\partial F}{\partial \sigma'_3}\frac{\partial G}{\partial \sigma'_1}D^e_{11} + D^e_{33}\frac{\partial F}{\partial \sigma'_3}\frac{\partial G}{\partial \sigma'_3}D^e_{31}}{H - H_{cr}} \tag{A.33}$$

$$D^{ep}_{33} = D^e_{33} - \frac{D^e_{31}\frac{\partial F}{\partial \sigma'_1}\frac{\partial G}{\partial \sigma'_1}D^e_{13} + D^e_{31}\frac{\partial F}{\partial \sigma'_1}\frac{\partial G}{\partial \sigma'_3}D^e_{33} + D^e_{33}\frac{\partial F}{\partial \sigma'_3}\frac{\partial G}{\partial \sigma'_1}D^e_{13} + D^e_{33}\frac{\partial F}{\partial \sigma'_3}\frac{\partial G}{\partial \sigma'_3}D^e_{33}}{H - H_{cr}} \tag{A.34}$$

A.6. TANGENT MATRIX FOR STRAIN CONTROLLED DRAINED TRIAXIAL STRESS PATH ($d\varepsilon_1$, $d\varepsilon_2 = d\varepsilon_3$ WITH $\sigma'_2=\sigma'_3=\sigma_2=\sigma_3=$ CONSTANT)

$$\sigma'_3 = Cst \rightarrow d\sigma'_3 = 0 \rightarrow \begin{cases} d\sigma'_1 = D_{11}d\varepsilon_1 + D_{13}d\varepsilon_3 \\ 0 = D_{31}d\varepsilon_1 + D_{33}d\varepsilon_3 \end{cases} \rightarrow \begin{cases} d\sigma'_1 = \left(D_{11} - D_{13}\dfrac{D_{31}}{D_{33}}\right)d\varepsilon_1 \\ d\varepsilon_3 = -\dfrac{D_{31}}{D_{33}}d\varepsilon_1 \end{cases} \tag{A.35}$$

With

$D_{11} = D_{11}^{e}$, $D_{13} = D_{13}^{e}$, $D_{31} = D_{31}^{e}$, $D_{33} = D_{33}^{e}$ if elastic

$D_{11} = D_{11}^{ep}$, $D_{13} = D_{13}^{ep}$, $D_{31} = D_{31}^{ep}$, $D_{33} = D_{33}^{ep}$ if elastic-plastic

A.7. TANGENT MATRIX FOR STRAIN CONTROLLED UNDRAINED TRIAXIAL STRESS PATH ($d\varepsilon_1$, $d\varepsilon_2=d\varepsilon_3$ WITH $d\varepsilon_V=d\varepsilon1+d\varepsilon_2+d\varepsilon_3=0$ AND $\sigma_2=\sigma_3=$CONSTANT)

$$\sigma'_3 = \sigma_3 - u \rightarrow d\sigma'_3 = 0 - du \tag{A.36}$$

$$\sigma'_1 = \sigma_1 - u \rightarrow d\sigma'_1 = d\sigma_1 - du \tag{A.37}$$

$$\varepsilon_v = \varepsilon_1 + 2\varepsilon_3 = 0 \rightarrow d\varepsilon_1 + 2d\varepsilon_3 = 0 \rightarrow d\varepsilon_3 = -\frac{1}{2}d\varepsilon_1 \tag{A.38}$$

$$d\sigma'_1 = D_{11}d\varepsilon_1 + D_{13}d\varepsilon_3 = \left(D_{11} - \frac{1}{2}D_{13}\right)d\varepsilon_1 \tag{A.39}$$

$$d\sigma'_3 = D_{31}d\varepsilon_1 + D_{33}d\varepsilon_3 = \left(D_{31} - \frac{1}{2}D_{33}\right)d\varepsilon_1 \tag{A.40}$$

With

$D_{11} = D_{11}^{e}$, $D_{13} = D_{13}^{e}$, $D_{31} = D_{31}^{e}$, $D_{33} = D_{33}^{e}$ if elastic

$D_{11} = D_{11}^{ep}$, $D_{13} = D_{13}^{ep}$, $D_{31} = D_{31}^{ep}$, $D_{33} = D_{33}^{ep}$ if elastic-plastic